



DEVELOPMENT OF A LINEAR DIATTENUATION SENSITIVE SEMI- AUTONOMOUS AND PORTABLE DIGITAL LENSLESS HOLOGRAPHIC MICROSCOPE.

Maria Josef Lopera Acosta

Prof. Carlos Trujillo

Applied Optics Research Group
Universidad EAFIT
Medellín, Colombia
2022





"The dimmed outlines of phenomenal things all merge into one another unless we put on the focusing glass theory and screw it up to one pitch of definition and then to another so as to see down into different depths through the great millstone of the world."
-James Clerk Maxwell





ABSTRACT

This document presents the development of a linear diattenuation sensitive, semi-autonomous and portable digital lensless holographic microscope (DLHM). With the development of this project, we aim to improve the performance of this microscopy technique and broaden the possibilities for a portable DLHM device. We believe our microscope can potentially be used in the diagnosis of diseases.

In order to address this aim, the following aspects were investigated within this project's scope.

i) The design of specialized illumination sources for DLHM that are efficient, mechanically stable, and easy to align. ii) The implementation of a DLHM sensitive to the linear diattenuation response of samples. iii) The study of machine-learning based autofocus methods to be applied to DLHM holograms. iv) The design of specialized software to acquire and reconstruct DLHM holograms, and iiv) the design and manufacture of proper mechanical couplings that integrate the DLHM setup with the cellphone's digital sensor.

Five papers and six conference proceedings are the resulting academic products of this thesis project. They constitute part of the core of this thesis and are attached at the end of the document.

Keywords: digital lensless holographic microscopy, linear diattenuation, polarization, portability, spherical wavefront source, numerical reconstruction, autofocus.



TABLE OF CONTENTS

Abstract.....	5
1. Theoretical framework & state of the art	11
1.1. Sample close to source DLHM (SCS-DLHM)	12
2. Problem statement.....	16
3. Objectives	17
3.1. General objective.....	17
3.2. Specific objectives	17
4. Linear diattenuation imaging of biological samples with digital lensless holographic microscopy	18
5. Specialized illumination system for portable dlhm	19
6. Portable DLHM	21
7. FocusNET: An autofocusing learning-based model for dLHM.....	25
8. DLHM App	29
8.1. General aspects	29
8.2. Backend.....	30
8.3. Frontend.....	32
8.4. User manual	32
9. Conclusions and future work	34
Acknowledgements.....	36
References.....	37
Published manuscripts.....	42
Manuscripts to be submitted.....	43
Conference proceedings	44
Annexes.....	45



LIST OF FIGURES

Figure 1. Basic in-line digital lensless holographic microscope setup.	13
Figure 2. Photograph of the holographic point source (HPS) illuminated with a planar 633nm coherent wave-source and generating a magnified diffraction pattern of a Siphonaptera.....	19
Figure 3. OpticStudio optical setup for the pinhole-based illumination system for LED source.	21
Figure 4. Designed mechanical coupling for the pinhole based portable DLHM.....	22
Figure 5. (left) designed mechanical coupling for the portable DLHM. (right) Picture of the manufactured prototype of the portable freeform-based DLHM.	23
Figure 6. Intensity reconstruction of a positive USAF target with the portable freeform-based DLHM.	24
Figure 7. Classical autofocusing metrics for a DLHM hologram.	26
Figure 8. Flux diagram of the DLHM-App.....	33



INTRODUCTION

Digital Lensless Holographic Microscopy (DLHM) is the simplest Digital Holography (DH) technique. Inspired by Gabor holography, it is based on an in-line holography technique with a spherical wavefront source [1–3]. As a holographic technique, it allows the retrieval of the complete optical field of the sample, including its amplitude and phase [4]. The phase sensitivity of the device has led to important contributions to biology and medicine applications when analyzing translucent objects, such as microorganisms [5–7]. DLHM is particularly attractive when developing portable devices due to its simplicity. Acquiring a DLHM hologram requires a spherical wavefront source illumination, a sample, and a digital sensor [3]. This feature allows miniaturized microscopes and has broadened microscopy applications [8–10]. DLHM is a technique supported by the principles of holography; therefore, it requires two stages: recording and reconstruction. The recording stage consists of the acquisition of intensity patterns, *holograms*, and the reconstruction involves recovering the information encoded in the holograms through a numerical backpropagation of the acquired hologram using a replica of the spherical wavefront used to illuminate the sample.

DLHM has been the object of study of several research groups [11–15], and two distinctive modalities can be detected in this technique: the on-chip method, in which the sample is located very close to the sensor [13], or the source close to sample: DLHM (SCS-DLHM). In the latter, the sample is illuminated by a point source [16]. As DLHM allows high magnifications and better resolutions without the need for specialized sensors or intensive numerical processing, this regime of DLHM is in which we are most interested. Although this technique has been widely studied for the past two decades, new proposals are constantly reported, and we encountered a few topics that can be addressed to enhance the technique's performance and potentiate its usage in portable devices applied to medicine or biology applications.

In this master thesis, a systematic review has been performed to establish the principal limitations to be addressed in the current available DLHM. The main limitations of the reported proposals are i) the divergent illumination wavefront source usually involves complicated and unstable optical setups, ii) the challenging and computationally time-consuming autofocus methods for DLHM holograms. iii) the two steps of the holographic technique (registration and reconstruction) limit its use, and there are no easy-to-use user interfaces connected to the digital sensor, and iv) there are no straightforward proposals involving the recovery of polarization information using DLHM.

In the context of this master thesis, all these points have been addressed to pave the way to developing new applications and possibilities for DLHM in different fields. For instance, we have implemented a DLHM sensitive to the linear diattenuation response of samples by adding two linear polarizers to the conventional DLHM setup [15]. This setup allowed the measurement of the first and second Stokes parameters of biological samples, achieving the visualization of birefringent crystals and granules present in different biological environments. Following the previously mentioned drawbacks, we proposed, designed, fabricated, and evaluated two novel illumination sources. The first one consists of a holographic optical element (HOE) [17,18]. that provides the required spherical wavefront illumination for lensfree microscopy. Our HPS will



pave the way to further development of lensfree microscopy, considering that HPSs are inexpensive, high-performant, highly efficient and compact elements. Our second proposal consists of a cost-effective freeform lens that focuses the incoming wavefront source of a diode laser providing a divergent spherical wavefront source that meets the requirements for DLHM. Experimental and simulation results show that our new point sources surpasses conventional drawbacks, such as mechanical instability and the need for bulky illumination setups, thus easing the path for robust and miniaturized DLHM implementations. These proposals will be beneficial for fieldwork applications which is one of the primary purposes of DLHM.

Regarding the issue involving the two-step procedure inherent in holography, we have designed a mechanical coupling that can be easily aligned with a cellphone's camera. Moreover, a mobile application, called DLHM-App has been designed and implemented. This App allows the acquisition and reconstruction of holograms directly with the cellphone.

Finally, addressing the autofocus challenge in DLHM, a deep learning convolutional neural network has been trained to predict the location of the sample directly from the DLHM hologram. This model also makes part of our DLHM-App, so the user only requires acquiring the hologram and its recording parameters to visualize reconstructed (in focus) images. The most significant novel results derived from this master thesis have been reported in high-impact Journals of the field and international conferences. The reference to each manuscript is indicated in each chapter of this thesis. We invite the reader to go deeper into each chapter by reading the corresponding article.

The published papers are:

- "Linear diattenuation imaging of biological samples with digital lensless holographic microscopy" [19].
- "Polarimetric microscope web application for simulated and experimental retrieval of polarimetric properties of biological samples" [20].
- "Holographic optical element for digital lensless holographic microscopy ' s illumination" [17].

The submitted papers and papers that will be submitted are:

- "Freeform-based illumination source for digital lensless holographic microscopy." Submitted to Optics Express.
- "FocusNET: An autofocus learning-based model for digital lensless holographic microscopy". To be submitted in Optics and Laser Engineering.

The proceedings from the participation in scientific meetings through oral and poster presentations are:

- "Single-shot dual-wavelength Polarized Microscope to detect Malaria-infected Erythrocytes via birefringence response Maria" [21].
- "Bright Field Polarimetric Microscope Web Application" [22].
- "Holographic point source for digital lensless holographic microscopy" [23].
- "Portable cellphone-based digital lensless holographic microscope" [24].
- "Learning-based autofocus regression model for Digital Lensless Holographic Microscopy" [25].



- "Linear diattenuation sensitive lens-free holographic microscope" [26].

The text below is divided into eight chapters. The theoretical framework and state of the art of DLHM technique are presented initially. Later, the problems we intend to solve with this thesis are presented with the objectives we aim to meet. After that, each chapter includes a brief introduction to a single research topic and the corresponding reference to the derived manuscripts or annexes. Then conclusions and future work are presented. By the end of the manuscript, the five papers and six proceedings that constitute the core of this master thesis are attached.



1. THEORETICAL FRAMEWORK & STATE OF THE ART

Compound microscopy was first proposed in the 16th century; Galileo, Hooke, and Kepler put together two lenses and appreciated a magnified object for the first time [27]. This event made part of the scientific revolution and improved medicine's evolution as it allowed humanity to observe microorganisms that caused and still cause diverse diseases. Until the 18th century, the poor resolution and aberrated images obtained by the scientist in their labs remained intact. In 1886 Carl Zeiss and Erns Abbé developed for the first-time apochromatic microscopic objectives, reducing spherical and chromatic aberrations [6], thus allowing microscopy to reach the theoretical resolution imposed by the wavelength of light [28]. Bright-field microscopy has remained intact despite many hardware enhancements over the years, including polarizers and digital cameras [9]. Compound microscopy consists of three essential elements: an illumination source, a microscope objective, and an ocular [29].

The main limitations of classical microscopy can be split into optical and handling limitations. For the optical limitations, the most representative constraints are the tradeoff between resolution and field of view (or the space bandwidth product) and the limited ability to manage three-dimensional or optical dense samples. Moreover, from the user standpoint, the drawbacks are the bulkiness and cost of the microscopy systems [9,30].

There has been a renaissance of optical microscopy research and development in the past decades to overcome these limitations. Different proposals have been made to improve the resolution and sensitivity of microscopes while at the same time introducing new imaging modalities making existing imaging systems more efficient, accessible, and portable.

A technique denominated computational imaging emerged to improve the existing optical microscopes' resolution [9]. With this technique, the images are formed indirectly from different measurements, and the final result relies on diverse algorithms, such as numerical reconstructions; those proposed methods have increased the images' complexity, quality, and resolution. Among these emerging computational microscopy techniques, coherent diffraction imaging (CDI) appeared as a lens-free proposal that allows two- and three-dimensional reconstructions of samples with a small and simple optical setup that only involves a divergent wavefront source that impinges the sample and a sensor (CMOS or CCD) that registers the information [9]. The sample can be placed in the free space between the illumination source and the sensor. Depending on where the sample is located, the technique differs on its mathematical modeling, the required numerical reconstruction algorithm, and the image's resolution and field of view. Another important advantage of this technique is that by removing refractive elements of the imaging system, the computational image is aberration-free, and its resolution relies only on the diffraction parameters (wavelength, coherence, aperture size, and exposure) [9].



One of the most common CDI configurations found in literature is the on-chip microscopy first proposed by Professor Aydogan Ozcan in 2010 [31]. For this technique, the sample is placed close to the sensor, generally at $< 1\text{mm}$ [8,10]. These microscopes have been explored to bypass various limitations of conventional compound microscope as they provide much more compact and cost-effective imagers. In this microscopic technique, the sensor records an in-line hologram instead of capturing a microscopic image. From this hologram, the amplitude and phase of the object can be recovered using numerical reconstruction [9,32] or deep learning-based algorithms [33]. In these systems, the resolution is primarily influenced by the pixel size, and the field of view is determined by the image sensor area [31]. The recorded spatial information is the interference between a reference light wavefront, the light wavefront passing through the transparent sample unperturbed, and the light wavefront scattered by the samples [9]. From this interference pattern, the optical properties of the unknown object can be recovered by implementing a discrete version of a scalar diffraction integral [30]. A lot of different proposals and variations have emerged from the on-chip technique, such as lens-free shadow imaging [34], scanning lens-free non-holographic on-chip imaging [35,36], lens-free fluorescence [37], reflection imaging on a chip [38], among others [16].

One of the potential limiting factors encountered in the on-chip technique is the sensor quality dependency for the resolution. The primary resolution-limiting factor for the unit-magnification lens-free on-chip imaging geometry becomes the image sensor's pixel size [9]. However, for these cases where the pixel size is the constraining factor, proposals have been made using pixel super-resolution techniques [39,40]; nevertheless, those solutions increase the computational complexity and cost of the devices.

1.1. Sample close to source DLHM (SCS-DLHM)

Contrary to the on-chip technique, this technique seeks to record the diffraction pattern of the magnified sample. It is ideal to place the sample close to the illumination source to achieve this. We call this technique sample close to source DLHM (SCS-DLHM), and in the literature, it can be found simply as DLHM or in-line holography. This technique was first proposed by professor H.J Kreuzer in 1999 [2,41] as a tool that yields 3D imaging of objects with micrometer resolution and allows the study of moving objects. Since 2006, professor J. G-Sucerquia has contributed to this technique and owns a patent registration for a lensless holographic microscope with a methodology to visualize samples [3,42]. The basic SCS-DLHM setup is depicted in Figure 1



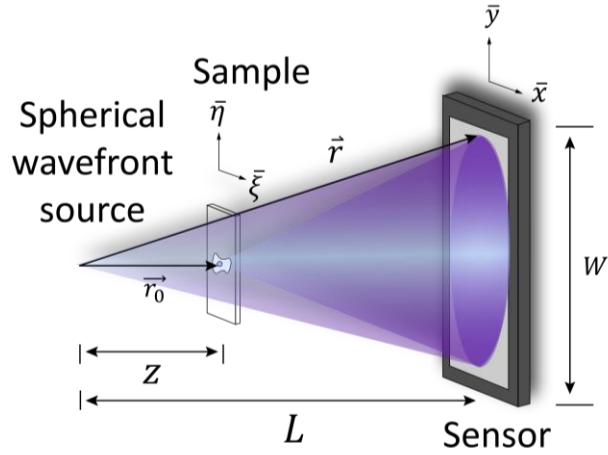


Figure 1. Basic in-line digital lensless holographic microscope setup.

To mathematically describe the SCS-DLHM hologram, consider that the sample transmittance $S(\vec{r}_0)$, placed at a distance z from the point source, is illuminated by a diverging spherical wavefront $\exp[ik\vec{r}]/|\vec{r}|$. The diffracted wavefield is magnified by free-space propagation until it reaches the digital sensor at a distance L from the point source. Vectors $\vec{r}_0 = (\xi, \eta, z)$ and $\vec{r} = (x, y, L)$ denote the source to sample and source to camera position, respectively. The description of the complex-valued intensity that reaches the sensor is given by the Rayleigh-Sommerfeld diffraction formula given by Eq. (1) [43,44].

$$U(\vec{r}) = \int_{\text{sample}} S(\vec{r}_0) \frac{\exp[ik\vec{r}_0]}{|\vec{r}_0|} \frac{\exp[ik(\vec{r} - \vec{r}_0)]}{|\vec{r} - \vec{r}_0|} d\vec{r}_0 . \quad (1)$$

Then, the intensity distribution recorded at the digital plane, known as the in-line or DLHM hologram, is described by Eq. (2),

$$I(\vec{r}) = U(\vec{r}) U^*(\vec{r}). \quad (2)$$

As a holographic technique, the information of the sample $S(\vec{r}_0)$ is retrieved by backpropagating the hologram with a converging spherical wavefront $\exp[ik\vec{r}]/|\vec{r}|$ which is the complex conjugated wavefront used to register the hologram. This diffraction process can be numerically described through a scalar diffraction formula; the sample's information is found via Eq. (3)

$$S(\vec{r}_0) = \int_{\text{sample}} I(\vec{r}) \frac{\exp[-i\vec{k} \cdot \vec{r}]}{|\vec{r}|} \frac{\exp[-i\vec{k} \cdot (\vec{r} - \vec{r}_0)]}{|\vec{r} - \vec{r}_0|} d\vec{r} . \quad (3)$$

From Eq. (3), the complex-valued optical field of the sample is recovered, and the amplitude $|S(\vec{r}_0)|$, intensity $S(\vec{r}_0)S^*(\vec{r}_0)$ or phase $\phi(\vec{r}_0) = \arctan(\text{Im}[S(\vec{r}_0)]/\text{Re}[S(\vec{r}_0)])$ can be retrieved [41,45]



Unlike the on-chip technique presented above, the resolution of this system depends on the geometry of the setup and the illumination wavelength [44], not directly on the pixel size. This dependency allows images to be achieved without needing smaller pixel size sensors. On the other hand, the magnification of this system depends on the distance between the sample and the point source, and it is not strictly necessary to post-process the reconstructions to visualize more details of the samples.

Different proposals and innovative variations have emerged from this technique, such as underwater DLHM and 4D tracking using DLHM [3], numerical darkfield illumination [46], among others. The most recent proposals of SCS-DLHM found in the literature, including portability, polarization, cost-effectiveness, or user interfaces, were studied to encounter the main limitations of the devices to propose a novel SCS-DLHM for this master's thesis project; these proposals are presented below.

- **"Open-source, cost-effective, portable, 3D-printed digital lensless holographic microscope"**

H. Tobon-Maya, S. Zapata-Valencia, E. Zora-Guzmán, C. Buitrago-Duque, and J. Garcia-Sucerquia, *Appl. Opt.* **60**, A205 (2021). [23]

This proposal presents a US\$56 3D-printed DLHM. The device allows numerical apertures from 0.65 to 0.0023 and spatial resolutions from 0.5 to 6.5 μm . This device's resolution and numerical aperture make it appropriate to visualize biological samples in amplitude and phase, such as red blood cells or cheek cells. In this research, several evaluations concerning the alignment of the point source were made, and the final device uses a 0.65 NA plug-and-play aspherical lens to focus a 5mW laser diode light source into a metallic pinhole with a diameter in the order of λ (650nm). The in-line holograms obtained with this device are processed using an open-source ImageJ plugin previously developed by the authors. The development of this DLHM microscope shows great promise as a disposable state-of-the-art microscopy tool to be used in remote areas as a point-of-care diagnosis tool, as a teaching tool for modern microscopy technologies, or as a research tool for laboratories with limited resources.

- **"Digital lensless holographic microscopy: numerical simulation and reconstruction with**

ImageJ" C. Trujillo, P. Piedrahita-Quintero, and J. Garcia-Sucerquia, *Appl. Opt.* **59**, 5788 (2020). [22]

An essential step in all holographic techniques is the reconstruction of the hologram. This paper presents an ImageJ open-source plugin for the numerical simulation and reconstruction of DLHM holograms. This software powered on ImageJ environment has two models: simulation and reconstruction. The simulation model uses a discrete implementation of the Rayleigh-Sommerfield diffraction formula to simulate holograms and reference images. The reconstruction model allows recovering intensity and phase information of experimental or simulated DLHM holograms with the insertion of all the parameters related to the setup. This computing tool tends to simplify the analysis, enhancing, packing, and sorting (among other tasks) of the retrieved information.



- **"Holographic image reconstruction with phase recovery and autofocusing using recurrent neural networks"** L. Huang, T. Liu, X. Yang, Y. I. Luo, Y. Rivenson, and A. Ozcan, (2021). [47]

This work presents a convolutional recurrent neural network (RNN) -based phase recovery algorithm that uses multiple holograms captured at different sample-to-sensor distances to rapidly reconstruct the phase and amplitude information of a sample while also performing autofocusing with the same network. The raw holograms are collected using a lens-free in-line holographic microscopy, and the sample is placed close to the sensor. The results of this research present advantages over existing phase retrieval and holographic image reconstruction methods in terms of image quality, DOF and reconstruction speed.

- **"Deep-learning-enabled Holographic Polarization Microscopy"**. B. Bai, D. Karalli, H. Wang, H. Fu, J. FitzGerald, K. de Haan, T. Liu, Y. Zhang, Y. Rivenson, Y. Luo, H. Wang, D. Karalli, H. Fu, A. Ozcan Conf. Lasers Electro-Optics (2021), Pap. ATh4F.5 (2021). [48]

Polarization microscopy is used as a contrast-enhancing technique; it allows the study of birefringent properties of sub-cellular structures. In this project, a lensless on-chip polarization microscope is presented. The device uses a light source with a large diameter aperture and two circular polarizers to indirectly register birefringent information on the sensor. Using holograms collected under a single polarization state, a deep-learning framework transforms amplitude and phase information of samples into birefringence, retardance, and orientation images.



2. PROBLEM STATEMENT

The arrival of optical microscopy was a fact that revolutionized medicine since it allowed the proper observation of smaller objects than previously possible to resolve and thus understand the biology inside each living being [3]. Thanks to the latter, it has been possible to identify disease-producing agents and diagnose them, thus improving patients' quality of life and life expectancy. Some particular microscopic techniques, such as polarimetric microscopy and digital holography microscopy, have been desirable in the biomedical areas as the polarimetric effects of light account for the nature of tissues and provide structural information. Phase retrieval is particularly needed in this biomedicine as cells and organic tissues are phase elements (transparent) [50–52].

Although the diagnosis and cure are well investigated for most of the diseases that cause and have caused public health problems, there is still a large gap between those who receive the benefits of science and those who do not. This gap is especially appreciable in developing countries [53]. In the U.S, approximately five deaths caused by *Plasmodium* parasite are reported annually [54], whereas, in Nigeria, approximately 108.000 deaths caused by malaria were reported in 2019 [55]. In Colombia, parasitic diseases caused 22% of the deaths registered in 2019 [1,2]. To attend those needs, portable microscopes have emerged as devices that seek to be cheaper than a conventional microscope and easier to transport; besides, due to the rising tide of artificial intelligence, early diagnosis of lethal diseases, such as malaria, have been performed with the use of those portable devices [58–60].

To use a device based on DLHM to mitigate public health problems in Colombia, some limitations must be overcome in the literature on the currently available DLHM devices. Some of the limitations are:

- Although they do not have lenses, the alignment of the light source can be overly complicated, more in the case of the use of pinholes.
- The devices do not provide any user-friendly interface that allows any audience to reconstruct the holograms easily and efficiently.
- Most proposals that include polarimetric information are purely research projects, and portable proposals including polarization were not found.
- Most portable and cellular-based devices are not ergonomically designed, *i.e.*, they are not directly intended to be in a medical and laboratory environment. Some of the factors that should be considered in the design are the person's position to use the device, how the device will be held for an extended period of time, and how the positioning of the sample will be optimized.

Contextualized the importance of microscopy in medicine and epidemiology, the social problems to be mitigated in addition to the limitations found in the portable DLHM proposals found in the literature, a research question arises: *is it possible to develop a portable, low-cost, appropriate performance DLHM microscope which is able to image biological samples in order to be used as a tool to mitigate the public health problem presented in the low-income and tropical areas of Colombia?*



3. OBJECTIVES

3.1. General objective

Develop a diattenuation-sensitive, semi-autonomous, and portable digital lensless holographic microscope (DLHM) to retrieve biological samples information.

3.2. Specific objectives

- I. Create a state of the art of DLHM or in-line technique by performing a systematic review to identify the limitations of the currently available proposals and devices.
- II. Design a specialized illumination system using freeform optics to improve the quality and stability of field portable DLHM.
- III. Implement a DLHM system sensitive to linear diattenuation for polarimetric properties measurements of biological samples.
- IV. Develop a user-friendly cost-effective mechanical coupling that allows the assembly of a DLHM setup with a smartphone camera.
- V. Optimize the automatic focusing of DLHM holograms by studying classical and deep learning-based strategies to enable computationally efficient inspection of microscopic volumes.
- VI. Develop a cellphone application using ReactNative and Flask to retrieve information provided by a portable DLHM.



4. LINEAR DIATTENUATION IMAGING OF BIOLOGICAL SAMPLES WITH DIGITAL LENSLESS HOLOGRAPHIC MICROSCOPY

To increase the information of the samples that can be retrieved with microscopic techniques, a first prototype was implemented. It consisted of a coherent RGB bright field microscopy with two linear polarizers. To implement the polarimeter, a linear polarizer (PSG) was inserted before the microscope objective, and the second linear polarizer was inserted after the sample and the tube lens. With this linear polarimeter, we retrieve the first and second Stokes parameters and find the linear diattenuation response of different biological samples. We encountered that the *plasmodium* parasite presents negative linear diattenuation for $\lambda = 532$ nm. This work was reported in the Conference on Lasers and Electro-Optics (CLEO) 2021. **"Single-shot dual-wavelength Polarized Microscope to detect Malaria-infected Erythrocytes via birefringence response Maria"** [21].

To complement this work, simulations of the polarimetric bright field microscope were made, and a virtual polarimeter was simulated and deployed into a web application. This result was published in the *Optica Pura y Aplicada* journal. **"Polarimetric microscope web application for simulated and experimental retrieval of polarimetric properties of biological"** [20] and presented at the ENO CANCOA congress.

Finally, this linear diattenuation setup was merged into the digital lensless holographic microscopy setup by inserting a first linear polarizer before the spherical wavefront source and a second polarizer after the sample, close to the digital sensor. This implementation successfully achieved the research objective, and linear diattenuation of biological samples was retrieved. The results and details of the implementations were reported in the *Applied Optics* journal. **"Linear diattenuation imaging of biological samples with digital lensless holographic microscopy"** [19]



5. SPECIALIZED ILLUMINATION SYSTEM FOR PORTABLE DLHM

As presented in the state of the art of DLHM, the standard method to create the spherical wavefront source consists of a pinhole-based system [3,9,10]. A microscope objective followed by a micrometrical pinhole creates the spatial coherence required for the DLHM technique. This setup implies a complex alignment and expensive systems, which is unsuitable for developing a portable device. Therefore, the objective *"Design a specialized illumination system using freeform optics to improve the quality and stability of field portable DLHM"* was set.

Two different proposals were implemented to address this objective. The first one used diffractive optical elements to create the point source required. Using an off-axis transmission hologram setup, the point source was holographically registered on a light-sensitive photopolymer. As a result, a phase hologram with the point source information was achieved. To reconstruct the holographic point source (HPS), the hologram must be illuminated with a conjugated wavefront source. A photograph of the HPS is presented on Figure 2.

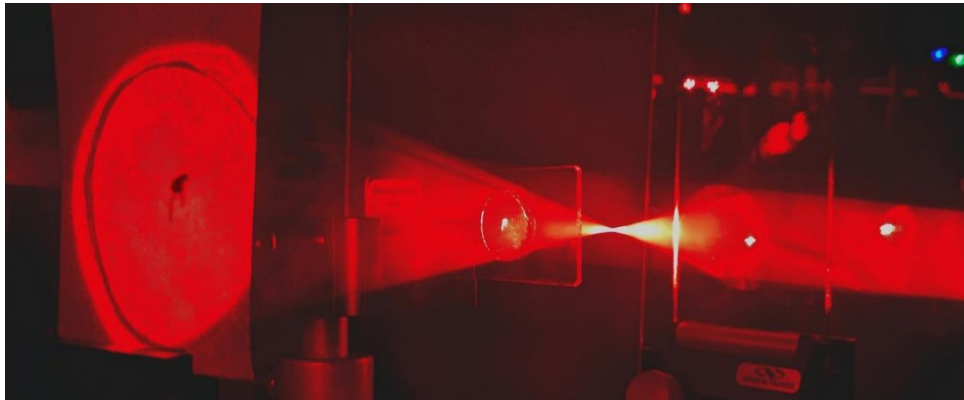


Figure 2. Photograph of the holographic point source (HPS) illuminated with a planar 633nm coherent wave-source and generating a magnified diffraction pattern of a Siphonaptera.

The performance of the HPS was evaluated and contrasted with classical pinhole-based results showing that the HPS is capable of achieving the same performance as the classical techniques but with the advantages of being flat, low-cost, easy to align, and optically more efficient. These results were published in the Optics Letters journal, presented in the Digital Holography and Three Dimensional Imaging Conference 2022, and submitted to the Optics & Photonics News (OPN's) **"Holographic point source for digital lensless holographic microscopy"** [23] **"Holographic optical element for digital lensless holographic microscopy 's illumination"** [17].

A second approach to overcome the drawbacks of the pinhole-based illumination system was the design and fabrication of a freeform lens-based illumination system with the sponsorship of



the B-PHOT group of VUB. A lens with an extended polynomial surface was optimized to achieve a divergent spherical wavefront source after the rear face of the lens. The details of the design and fabrication of the lens and its performance on the DLHM technique are detailed in the manuscript **"Freeform-based illumination source for digital lensless holographic microscopy"** which is already submitted to Optics Express journal.



B-PHOT
BRUSSELS
PHOTONICS

6. PORTABLE DLHM

As we aim to create a device that can be used outside the research environment, for instance, in fieldwork applications, we proposed to develop a user-friendly cost-effective mechanical coupling that allows the assembly of a DLHM setup with a smartphone camera.

The first approach for the portable microscope was designed to include in the illumination source a pinhole-based system with a light-emitting diode (LED) as the light source. The OpticStudio design of this optical setup is presented in Figure 3. A first bi-convex lens collimates the divergent wavefront source, and a second plano-convex lens focuses the beam into a spot. A micrometrical pinhole is located at the focusing plane to achieve the spatial coherence required in the technique. After the pinhole, the sample is placed, and a digital sensor records the information.

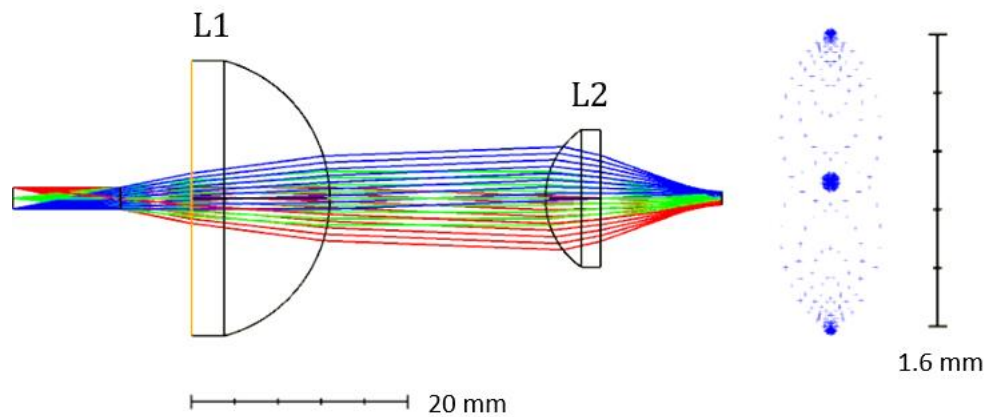


Figure 3. OpticStudio optical setup for the pinhole-based illumination system for LED source.

For the mechanical coupling of this portable version, all the components are embedded in a tube with two axes that allow the components' displacement for alignment purposes. The parts were 3D printed using PLA material and a filament printer. As stated in the specific objective, we aim to replace lab sensors with the digital sensor included in the cellphone cameras, and for this proposal, a Samsung S10+ cellphone was used. The details of the design and the results obtained with this proposal were presented at the Frontiers in Optics + Lasers Science 2021 conference, and the proceedings "**Portable cellphone-based digital lensless holographic microscope**" [24] is the result of this presentation.

A second approach was developed by supervising the bachelor's students Santiago Machado and Tomás Vélez. This approach also includes pinhole-based illumination. The mount consists of an acrylic base that holds the electronic components; then, a 3D printed vertical cantilever holds the 2f lens system and the pinhole. An 8 mm screw is included in the central axis to allow the sample's displacement to change the system's magnification. A Gosky adapter for telescopes and microscopes was included in the design to hold the cellphone. Figure 4 displays the design described.

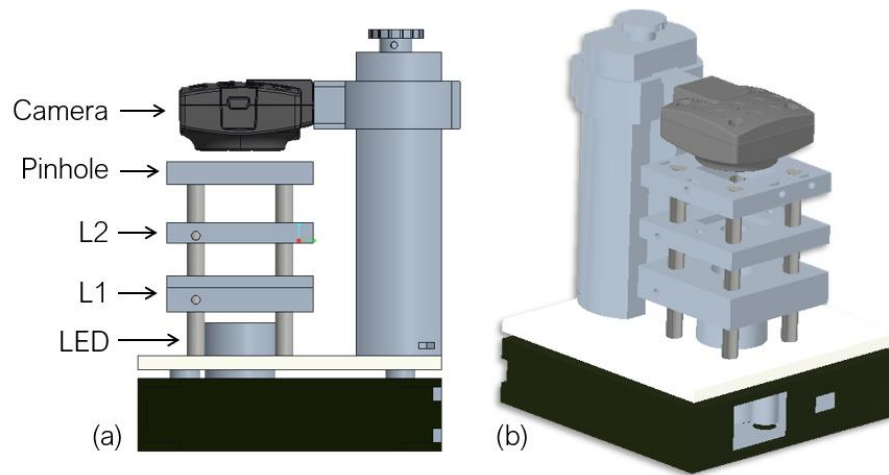


Figure 4. Designed mechanical coupling for the pinhole-based portable DLHM

Finally, another prototype similar to the first one was developed. After performing the research described in section 5, a freeform lens was obtained, and an specialized mechanical coupling was designed and manufactured for this specific light source. This prototype consists of a tube containing the required optical elements. As we demonstrated in this research, the freeform illumination system is much more efficient and easier to align than the conventional pinhole-based systems, and this is the main advantage of this proposal. In this design, we included the Gosky adapter to assemble the microscope with the cellphone. The only required elements for this design are the ones presented in Table 1.

Table 1. List of components required for the portable freeform-based DLHM.

Component	Degrees of freedom	Comment
Battery	Rigid	3.7 V rechargeable battery
On/Off switch	Rigid	
Diode laser	Rigid	407 nm 20 mW diode laser
Freeform lens	Z (slider)	
Microscopy slide	Z and X slider	

The prototype design was performed using the CAD software CREO parametric, paying special attention to the degrees of freedom of the components and the distances between them. Only five 3D-printed components are needed for the assembly of the prototype. Figure 5 presents the computer-assisted design on the left panel and a photograph of the final prototype on the right panel.

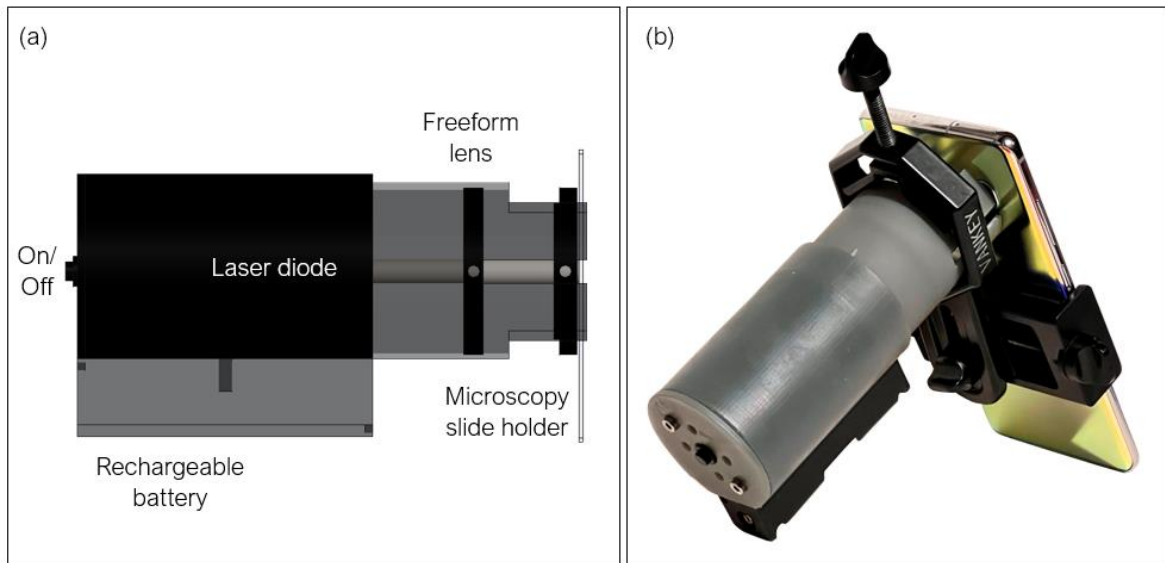


Figure 5. (left) designed mechanical coupling for the portable DLHM. (right) Picture of the manufactured prototype of the portable freeform-based DLHM.

The five parts that compound the mechanical coupling were printed using a Formlabs resin printer. The printing process took 17 hours and was sponsored by Professor Olga Quintero and Professor Juan Felipe Zuluaga. We acknowledge their collaboration in this project. The portable DLHM ensembled has a height of 13.6 cm and a weight of 250 gr.

An important matter that must be considered when working with cellphones is the optical system embedded in the cellphone's cameras. This optical system often projects a demagnified real image into the digital sensor. When using these devices, one must consider that this optical system will modify the illumination cone of the DLHM technique; therefore, the sensor will not be fully illuminated. The primary consequence of including this optical system in the DLHM setup is a decreased spatial resolution. Two solutions to overcome this issue can be implemented. The first one is to include an optical system before the cellphone camera to compensate its demagnification, and the second is to remove the optical system of the cellphone to record the holograms directly on the sensor. A HUAWEI P8 Lite was used as the digital sensor for our prototype. The optical system of the cellphone was removed. The squared size of this sensor is 2.4×2.4 mm, and the pixel pitch is $1.0 \mu\text{m}$. A hologram of a positive USAF target was recorded to validate the performance of the portable freeform-based DLHM. The source to camera distance for the setup was 20mm, and the object was located at 10mm, yielding a $2\times$ magnification, 0.12 NA, and $1.71 \mu\text{m}$ resolution. Figure 6 Presents the intensity reconstruction.

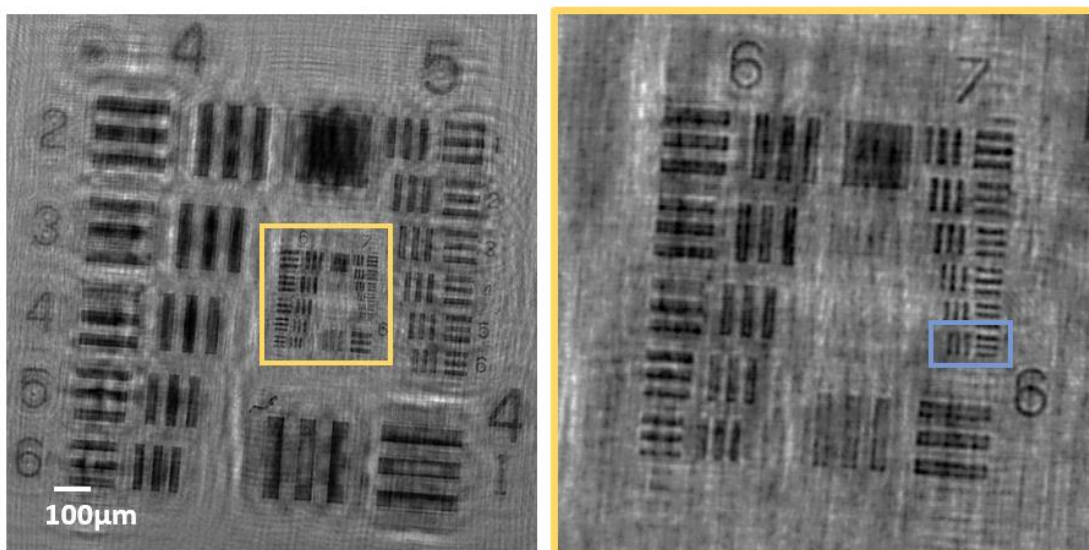


Figure 6. Intensity reconstruction of a positive USAF target with the portable freeform-based DLHM. The yellow zoom-in area shows that the resolution of this system is $2.2\mu\text{m}$.

This resolution target allows measurement of lateral resolutions up to $2.2\mu\text{m}$. As can be observed in the zoom-in area (right panel) defined by the yellow square, the 7-6 group of the target is correctly imaged with a contrast of 0.85 using the portable freeform-based device and a cellphone camera.



B-PHOT
BRUSSELS
PHOTONICS

7. FOCUSNET: AN AUTOFOCUSING LEARNING-BASED MODEL FOR DLHM

When designing and developing a semi-autonomous holographic microscope, the automatic determination of the location of the sample in the holograms is an essential matter as the user cannot directly visualize the sample without the reconstruction step. This fact could make the microscope a hard-to-use device. Therefore, we must propose algorithms and processes in which the user does not have to act, easing the device's usability. To achieve this goal, the first step involves finding the object's focal distance automatically without consuming too much time. As we have stated, the automatic determination of the best focused reconstructed plane among a set of holographic reconstructions is one of the most active research topics, especially in digital holographic microscopy [61,62]. Traditionally, this task has been performed using focus metrics [62]. A number of reconstructions are calculated, and for each reconstruction, a degree of focus is measured [61]. The most referenced technique in DHM to measure this degree of focus is the Dubois metric [63,64]. In this metric, a pixel-wise summation of the amplitude of the reconstructed hologram is performed, then the reconstructed hologram whose degree of focus in minimum corresponds to the best focused reconstruction [61].

$$M = \sum |S(\vec{r}_0)| = \sum_{\xi, \eta} |S_z(\xi, \eta)| \quad (4)$$

Like these metrics, many others can be encountered in the DHM state of the art; some of them include the power spectra of the hologram [61,65], the variance of the reconstructed intensity [66], the Tamura coefficient [65], among others [61,63]. Nevertheless, these previously mentioned proposals fail to autofocus holograms of DLHM [61]. Prof. Trujillo designed a new method for autofocus in DLHM called modified enclosed energy (MEE) [67]. This method considers the spherical nature of the illumination inherent in the lensless technique and has shown to be robust enough to accurately predict the focus distance of DLHM hologram with lower computational complexity than traditional proposals [68]. The MEE proposal still requires iterations, numerical reconstructions, and the definition of specific parameters by the user. To overcome these issues, we propose as an objective of this thesis to optimize the automatic focusing of DLHM holograms by studying classical and deep learning-based strategies to enable computationally efficient inspection of microscopic volumes.

The classical techniques such as Dubois, spectrum-based, gradient-based, and variance-based, were studied and implemented, but they all work in a reduced range or only for specific

samples (amplitude or phase only). Figure 7. presents the focus metrics for a DLHM hologram. This hologram's ground truth in-focus reconstruction distance is 1.73 mm, but the possible focusing distance ranges from 0.3mm to 5mm. When the complete range is considered, panel (a) of Figure 7, we can observe different issues: a minimum is presented at approximately 0.8mm for the conventional metrics, which is not the accurate focusing distance. Also, after 3mm, the metric stabilizes, and for some metrics (Dubois and gradient), these values are lower than the previous results; hence, the algorithm will mispredict the focus distance. When the metrics are computed only within the range [1.5-3] mm, the results are presented in panel (b). In this range, all the metrics correctly predict the focus distance.

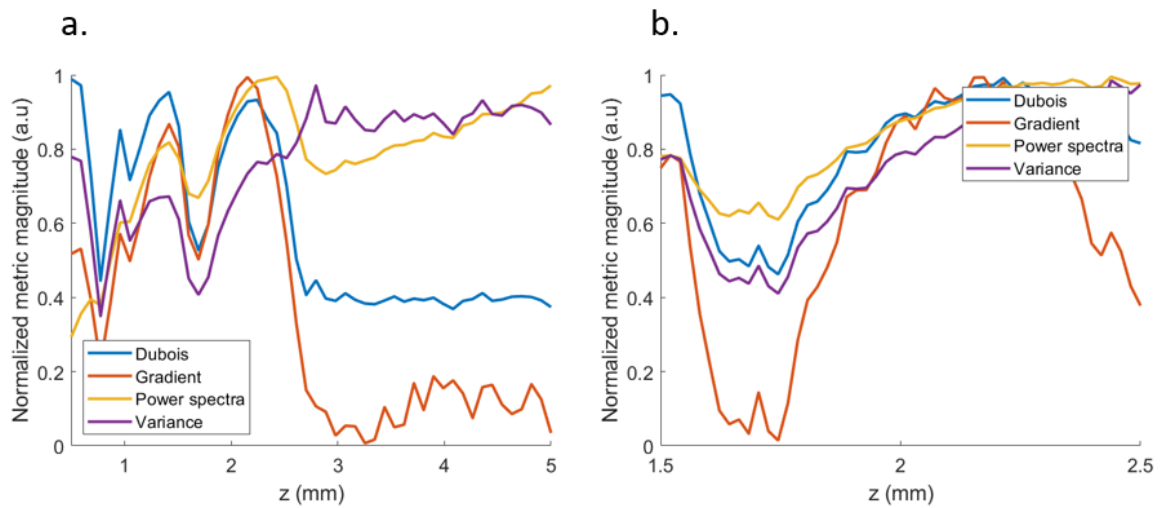


Figure 7. Classical autofocusing metrics for a DLHM hologram.

From this implementation, we noticed that the classical techniques fail to accomplish the goal required as tuning must be performed, and the user should set many parameters to get the object's position. To overcome these issues, a complete study of the possibilities of Machine Learning in this field was performed within the course "*Advanced Statistical*" and the thesis project of the Data Science and Analytics master's student Manuel Montoya.

Several approaches were studied in the statistical course framework: a low numerical aperture DLHM setup (this means large L (larger than 20mm)) as the one presented in Figure 1 was implemented, and 3000 holograms were recorded. The ground truth reconstruction distances were found employing the spectrum-based metric and the angular spectrum reconstruction algorithm. The z values range from 3mm to 36mm. The following samples were used: human cheek sample, cat cheek sample, potato starch granules, red blood cells, and a USAF test.

Inspired by an approach published by Zhu X. in 2018 [69], we started exploring this problem through a classification problem. Five models were implemented: multiclass logistic regression, support vector machines, random forest, and convolutional neural networks (with different architectures). A summary of the result is presented in the following Table 2.



Table 2. List of components required for the portable freeform-based DLHM.

Model	Optimizer	Loss function	Epochs	Accuracy train	Accuracy test
Logistic regression	SGD	Cross entropy	150	0.5	0.56
SVM	N/A	Logarithmic loss	20	1.0	0.87
Random Forest	N/A	OBB	300 (# threes)	1.0	0.87
CNN1	Adam	SGD	50	1.0	0.91
CNN2	Adam	SGD	150	1.0	0.96

With this implementation, we showed that machine-learning-based models are capable to classify holograms in terms of their reconstruction distance (where the classification label is a certain range of reconstructing distances). We obtained a maximum accuracy of 96% for test holograms. However, in practical terms, a second autofocusing step should be performed to obtain the exact value of the reconstruction distance. For that reason, a regression model suits better to solve this problem. In this case, a simple linear regression and the same CNN1 and CNN2 architecture models (but with a single regression layer at the end) were implemented. The results are shown below in Table 3.

Table 3. List of components required for the portable freeform-based DLHM.

Model	Optimizer	Loss function	Epochs	Error train (mm)	Error test (mm)
Linear regression	Adam	Mean squared error	150	16.3	16.6
CNN1	Adam	Mean squared error	150	2.8	9.3
CNN2	Adam	Mean squared error	150	0.6	0.9

The CNN2 architecture showed a reliable performance for the low NA DLHM holograms. This result was presented in the Digital Holography and Three-Dimensional Imaging congress 2022. **"Learning-based autofocusing regression model for Digital Lensless Holographic Microscopy"** [25].

Even though the last results are promising, distance errors of 1mm are still too large for biological applications, where the depth of the objects is in the order of μm . In the framework of the thesis of Manuel Montoya and the G8 project: *"Evaluación de las potencialidades de la microscopia sin lentes soportada en técnicas de aprendizaje profundo en el diagnóstico de malaria."*, we sought to improve the previously presented regression model in order to achieve



lower depth errors. In collaboration with the *Grupo de Investigación Óptica y Procesamiento Opto-digital* of Universidad Nacional de Colombia, a large numerical aperture DLHM dataset was acquired. The previous CNN2 architecture was improved by adding a layer containing the amplitude of the Fourier transform of the hologram, a resizing and dropout layers were also added. The new model denominated FocusNET achieved errors of $60\mu\text{m}$ at prediction times of 0.1 seconds on a 4 Cores CPU. This result represents an improvement in DLHM autofocusing. The paper "**FocusNET: An autofocusing learning-based model for digital lensless holographic microscopy**" reports the complete details of this project and will be submitted to the Optics and Lasers Engineering journal.



UNIVERSIDAD
NACIONAL
DE COLOMBIA

8. DLHM APP

As the design of the portable lensless microscope was intended to be used with a cellphone, as presented in section 6, we proposed to develop a cellphone application to retrieve the information provided by the portable DLHM. We aimed to have an application capable of using the cellphone's digital sensor to record, save and process the holograms. With the development of this objective, we want to facilitate the required procedures between the hologram registration and its reconstruction to decrease the processing time and make our microscope easy to use by any user.

This project was developed by supervising the bachelor's thesis of engineering physics student Sergio Jurado. This chapter presents the general aspects of the design and implementation of the DLHM-App.

8.1. General aspects

Our microscope intends to overcome certain limitations in the DLHM applied to medicine and biology, especially when dealing with low-income and tropical areas. The portability designed for our DLHM still has a bulky second step: the holograms should be acquired with the cellphone's camera and transferred to a computer where all the parameters should be set to reconstruct the DLHM holograms. This step is straightforward when the technique is well known. However, in general terms, the final user is not expected to understand this two-step procedure. Due to this, our device is still cumbersome and hard to use. A tool that connects the two steps of the holographic technique is still required; this is why the development of the DLHM-App was proposed. Below, three main aspects that were considered for the development are presented.

- Cellphone devices were chosen as digital sensors, as more than 78% of the global population owns one [70]. Moreover, Android phones have 89.47% of the smartphone market in Latin America. Phone manufactures make efforts to reduce the cost of the devices while increasing the quality of their software and hardware, paying particular attention to the camera(s) performance [71]. Due to this fact, the targeted smartphones are Android-based.
- To target simplicity and aesthetics in the development of the DLHM-App, React Native and Flask frameworks were chosen to develop the Frontend and Backend of the App. These microframeworks emphasize fast app prototyping and easy app complexity escalation [72].
- Our DLHM only requires a cellphone with a rear camera (one at least), internet connection, minimal internal storage (>1GB), and it must operate with Android API Level 21 at least. Because the hardware specifications of Android phones may vary, the processing duty is hosted by an external server. Via internet connection, the DLHM-App sends the holograms with the required data to the server; it processes the information and sends the result back to the DLHM-App.



- The source codes of the DLHM-App can be accessed via the following repository: <https://github.com/MrAgeo/DLHM-App> [73].

Further details of the Backend and Frontend are provided in the following subsections.

8.2. Backend

The backend of the App was developed using the python-based microframework Flask. The main tasks performed by the backend are the storage (in the ROM memory of the running server) and processing of the images. The processing of the holograms is performed via a built-in DLHM-API, which includes two different propagation models and a machine learning-based model. The details of the scalar version of the propagation models that make part of the DLHM-API are presented below.

- **Angular spectrum**

The angular spectrum propagation formalism was described and adapted from references [43,74,75]. The angular spectrum formalism for light propagation is based upon the spectrum of the propagating wavefront. Considering a wave field $U(x,y,z)$ that propagates along the z direction with a propagating vector $\vec{k} = 2\pi/\lambda$. At $z=0$, $U(x,y,z=0) = U_0(x,y)$. Also, considering that $A(f_x, f_y, z)$ is the Fourier transform of $U(x,y,z)$ the initial wave field U_0 can be described as follows,

$$U_0(x, y) = \iint A_0(f_x, f_y) e^{i2\pi(f_x x + f_y y)} df_x df_y \quad (5)$$

Where the **angular spectrum** of the wavefield U_0 is,

$$A_0(f_x, f_y) = \iint U_0(x, y) e^{-i2\pi(f_x x + f_y y)} dx dy \quad (6)$$

From Eq (5) one can notice that the term $e^{i2\pi(f_x x + f_y y)}$ is a plane wave at $z=0$ with direction cosines given by equations (7)-(9)

$$\alpha = \lambda f_x \quad (7)$$

$$\beta = \lambda f_y \quad (8)$$

$$\gamma = \sqrt{1 - (\lambda f_x)^2 - (\lambda f_y)^2} \quad (9)$$

Then, as the optical field $U(x,y,z)$ satisfies the Helmholtz equation, its angular spectrum satisfies it as well [43], therefore

$$A(f_x, f_y, z) = A_0(f_x, f_y) e^{iz \sqrt{k^2 - 4\pi^2(f_x^2 + f_y^2)}} \quad (10)$$

And then the optical field at a distance z becomes

$$U(x, y, z) = \iint A_0(f_x, f_y) e^{iz \sqrt{k^2 - 4\pi^2(f_x^2 + f_y^2)}} e^{i2\pi(f_x x + f_y y)} df_x df_y \quad (11)$$



Which can be simply summarized as follows: (FT: Fourier transform)

$$U(x, y, z) = \text{FT}^{-1} \left\{ \text{FT} \{ U_0(x, y) \} \cdot e^{iz \sqrt{k^2 - 4\pi^2(f_x^2 + f_y^2)}} \right\} \quad (12)$$

To numerically compute Eq. (12), it must be discretized. Through the Fast Fourier Transform, the value of the optical field of a sample located at a distance z can be easily encountered. For the discretization, let us consider a digital sensor with pixel pitches Δx and Δy and $M \times N$ number of pixels where m and n are the discrete indexes.

$$U[m\Delta x, n\Delta y, z] = \text{FFT}^{-1} \left\{ \text{FFT} \{ U_0(m\Delta x, n\Delta y) \} \cdot e^{iz \sqrt{k^2 - 4\pi^2((\Delta f_x m)^2 + (\Delta f_y n)^2)}} \right\} \quad (13)$$

If a DLHM hologram $I(\vec{r})$ (equations (1) and (2)) is registered with a plane wavefront, the information of the sample can be retrieved straightforwardly from equation (12). Nevertheless, as in the DLHM techniques a spherical source is used, this formalism is only accurate for plane wavefront illumination; this is valid for low numerical apertures ($\text{NA} < 0.1$) and magnifications close to one. When higher numerical apertures and high magnifications are used in the registration process, the angular spectrum will retrieve the information of the sample with an extra spherical phase component which can be interpreted as spherical aberration [76]. This aberration will also affect the accurate reconstruction distance of the object. The sample will be reconstructed at a different position.

- **Fresnel-Bluestein transform, Kreuzer's algorithm**

As previously mentioned, for proper reconstruction of DLHM holograms, a numerical propagator considering spherical wavefront illumination must be used. The Fresnel approximation of the Kirchhoff diffraction formula is the most suitable case as the size of the reconstruction plane increases while the distance z increases. Using the Fresnel-Bluestein transform, a simple kernel-convolution process is needed to reconstruct holograms with inherent magnifications [77]. The unidimensional discrete version of the Fresnel transform is presented above.

$$U_p(z) = \frac{e^{ikz}}{i\lambda z} e^{\frac{i\pi \lambda z p^2}{M^2 \Delta x^2}} \times \sum_{n=0}^{M-1} I_n e^{\frac{ik}{2z} \Delta x^2 n^2} \times e^{-i2\pi \frac{np}{M}}. \quad (14)$$

In Eq. (14), k is the wavenumber, $\xi = p\Delta\xi$ is the horizontal position at the reconstruction plane, therefore in the discrete version, $\Delta\xi$ is the pixel pitch at the reconstruction plane (Figure 1), and p is the discretization number, and this case the number of pixels. Similarly, in the hologram plane, $x = n\Delta x$, where n is the number of pixels and Δx is the sensor's pixel pitch. The casting process imposes the constrain that the input and output pitches must be related through $\Delta\xi = \lambda z / (M\Delta x)$.

The Fresnel-Bluestein transform involves rewriting the Fourier transform kernel: the product $2np$ as $2np = n^2 + p^2 - (p-n)^2$. This substitution was introduced by Bluestein and used by Kreuzer [78].



After replacing the expression in the Eq. (14) kernel, the Fresnel-Bluestein transform is obtained.

$$U_p(z) = \frac{e^{ikz}}{i\lambda z} e^{\frac{i\pi}{\lambda x} \Delta \xi (\Delta x - \Delta \xi) p^2} \times \sum_{n=0}^{M-1} I_n e^{\frac{i\pi}{\lambda z} \Delta x (\Delta x - \Delta \xi) n^2} \times e^{\frac{i\pi}{\lambda z} \Delta x \Delta \xi (p-n)^2} \quad (15)$$

Eq. (15) is in the form of a discrete convolution; its evaluation is commonly performed using the well-known discrete Fourier transform convolution approach [77]. Finally, this convolution can only be performed by guaranteeing the circularity of the convolving functions, which is satisfied by zero padding [77].

- **FocusNET**

The implemented learning-based autofocusing model FocusNET, described in section 7, is also included in the DLHM-API. The API uploads the model to the backend server, the *helpers* file, and the required *TensorFlow* functions and classes. Once the hologram is uploaded to the server, FocusNET finds the reconstruction distance, and with Kreuzer's algorithm, the sample's optical field is retrieved.

8.3. Frontend

The *frontend* is the graphical user interface or presentation layer that connects the interface's functionality with the user. The framework *ReactNative* was used for the *frontend* implementation. The *frontend* is in charge of holding the repository images, uploading and downloading the holograms from the cellphone's memory, and cleaning the cache whenever required. It connects the mobile App to the Flask server to process the previously described holograms. More than this, one of the main functionalities of the App is the camera; the *frontend* uses the primary cellphone's camera to acquire the holograms. To perform this, the *Expo-Camera* library was used. Using *JavaScript*, we modified this library to include some required features. The DLHM-App camera is capable of acquiring holograms, and the user is free to modify the following features of the camera:

- Exposure time
- Focus plane
- White balance
- ISO

8.4. User manual

Once the DLHM app is installed, it will be launched on the home page of the cellphone. The backend should be running in the server for the App to work. To use the App, one must open it and set the IP direction to connect the backend and *frontend*. As future work, we propose deploying this App to a web server to avoid this step.

The DLHM app has three main functionalities: to save the holograms in the repository from the local storage, acquire new holograms and save them in the repository, and reconstruct them. Once the App is opened, the user can process holograms from the repository, upload new holograms from the local storage or take new holograms with the DLHM-app camera. To process the hologram, the user should select it (with or without reference) and then select the



reconstruction formalism from the bottom bar of the App; depending on which formalism is selected, the parameters should also be set. The hologram (or hologram + reference) is uploaded to the server, and with the DLHM-API, the reconstruction is attained. The user can decide to save or discard the image and return to change the reconstruction parameters and reconstruct this hologram again or start from the home page and select a new one. Figure 8 presents the flux diagram of the DLHM-App.

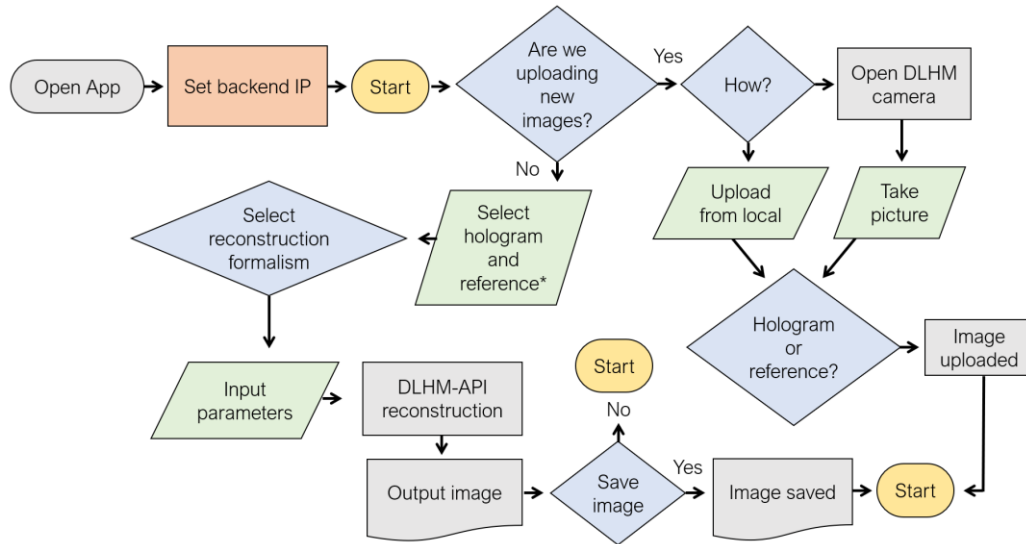


Figure 8. Flux diagram of the DLHM-App.

For a better understanding of the functionality of the DLHM-App, the user manual extracted from Jurado's thesis is attached in the annexes at the end of this document.

9. CONCLUSIONS AND FUTURE WORK

The main results obtained in the development of this master thesis can be summarized as follows:

A linear diattenuation sensitive DLHM (LD-DLHM) consisting of two linear polarizers inserted before and after the sample was reported. This setup allows the measurement of the linear diattenuation response of samples. Birefringent samples were used to test the device's sensitivity, and the results show their expected negative diattenuation response. The LD-DLHM is expected to enhance the diagnosis of diseases that are easier to evaluate via their polarization response.

Two new and novel spherical wavefront illumination sources were proposed to overcome the limitations imposed by the conventional pinhole-based illumination method. We develop a holographic point source and a freeform lens-based point source. The first proposal allows micrometrical point sources that enable divergent cones with high numerical apertures by modifying the incoming wavefront. Our HPS generates high-quality DLHM holograms obtaining high lateral resolution ($\sim 1\mu\text{m}$) reconstructions. The second proposal involves the design, optimization, and manufacture of a freeform lens specially designed to generate a divergent cone from a diode laser source. This element provides a highly stable, easy-to-align system suitable to be used in portable DLHM devices.

A machine learning-based autofocusing model was implemented to facilitate the in-focus reconstruction of the DLHM holograms. Our new method, FocusNET, predicts the object's location with an accuracy of $60\mu\text{m}$. This prediction is 600 times faster for a single hologram than the classical Dubois, spectrum-based, variance-based, and gradient-based metrics. More than this, our model can handle the prediction 1200 times faster than classical approaches when dealing with a batch of holograms. When processing with a computer powered with GPU, the prediction time can increase up to video-rate prediction.

A new 3D-printed mechanical coupling was designed, which enables a portable DLHM with a freeform-based illumination system. This mechanical coupling integrates freeform-based illumination system with a cellphone (any cellphone). With our design, the digital sensor of the cellphone registers the DLHM holograms. In order to facilitate the usability of our device, the DLHM-App was designed. The App controls the cellphone camera and allows the direct registration of the information. Also, the App includes the angular spectrum and Kreuzer reconstruction formalism together with our FocusNET model in order to perform the autofocusing procedure in a more efficient way.

Our DLHM-App, which includes the FocusNET model, together with the 3D-printed freeform-based portable DLHM and the LD-DLHM proposal, constitutes a microscope that is portable, stable, easy to align, and easy to use, that enhances the DLHM technique and, in general, the



portable devices which can be applied to potentiate the diagnosis of certain diseases such as malaria.

For this master thesis, two main lines are derived for further work,

The development of the holographic point source (HPS) is a novel proposal with enormous potential. The first developed proposal is yet limited by the light source that should be used for its reconstruction. This wavefront could be a planar or spherical wavefront source, but it should be radially symmetrical. As we have mentioned, we seek low-cost proposals, and even though our HPS is a cheap element, it requires a laser to be reconstructed. We propose to register this point source using as a reference beam an astigmatic source that mimics the typical irradiance of a diode laser in order to use the HPS with these light sources.

FocusNET model could be further developed by improving the ground truth focusing distance currently available. The distance is given by an XYZ mechanical stage used in the setup. We believe that a robust autofocus algorithm should give the ground truth distance. Additionally, the model's generalization can be improved by adding new holograms from different samples and DLHM geometries. A second proposal to improve the machine learning-based proposals is to implement an end-to-end model, which could be based on GAN network architectures [79]. With this model, we expect to decrease the processing time by removing the numerical propagation procedure.

Altogether, the improvements reported in the development of this thesis will lead to further work in the field of video-rate reconstructions, high-performance, low-cost illumination sources for DLHM, and its miniaturization aiming at fieldwork applications in the point-of-care diagnosis of diseases.



ACKNOWLEDGEMENTS

Everything I have achieved has not been on my own. There is no individual growth but collective growth. *"If I have seen further than others, it is by standing upon the shoulders of giants"* - Newton.

Thanks to the *vicerectoría de ciencia, tecnología e innovación* of Universidad EAFIT for the **research recognition** grant and to the G8 Metropolitan Area Universities for the financial support.

I would especially like to thank Professor Carlos for his inspiration, trust and support in every moment. To Professor Daniel Velásquez, for being my mentor and for inspiring every idea. To my mother for her unconditional support and Manuel Montoya for his patience and unconditional love.

To all my colleagues in the Applied Optics research group, for the support, the advices, the displays of creativity. Prof. René, Sofi, Arge, Nicoll, Diego, Waira, ~José. Thank you all!

To the engineering physics students who chose to contribute to this degree work within their projects, Santiago, Tomás, Sergio. Thank you

To Andrea Ortiz and Prof. Olga for their collaboration with the mechanical prototype.

To my B-PHOT teammates: Yunfeng, Ast, Tatev, Alejo and Koen for their friendship and collaborations. Special thanks to Professor Heidi for her trust and for making possible the design and fabrication of the FF-DLHM project.

To Professor Mauricio Arroyave for the USAF phase test measurements in the AFM.

To my two families, Lopera Acosta, Montoya Zuluaga. For being the unconditional pillars of my life.

All the people who have crossed my path have been a direct or indirect part of each of my achievements. Thank you very much for your contribution!



REFERENCES

1. E. N. Leith and J. Upatnieks, "Reconstructed Wavefronts and Communication Theory*," JOSA, Vol. 52, Issue 10, pp. 1123-1130 **52**, 1123–1130 (1962).
2. H. J. Kreuzer, I. A. Meinertzhagen, M. H. Jericho, and W. Xu, "Digital in-line holography of microspheres," Appl. Opt. Vol. 41, Issue 25, pp. 5367-5375 **41**, 5367–5375 (2002).
3. J. Garcia-Sucerquia, W. Xu, S. K. Jericho, P. Klages, M. H. Jericho, and H. J. Kreuzer, "Digital in-line holographic microscopy," Appl. Opt. **45**, 836–850 (2006).
4. G. Saxby, *Practical Holography* (Institute of Physics Pub, 2004).
5. D. Issadore and R. M. Westervelt, eds., *Point-of-Care Diagnostics on a Chip*, Biological and Medical Physics, Biomedical Engineering (Springer Berlin Heidelberg, 2013).
6. S. K. Jericho, J. Garcia-Sucerquia, W. Xu, M. H. Jericho, and H. J. Kreuzer, "Submersible digital in-line holographic microscope," Rev. Sci. Instrum. **77**, 043706 (2006).
7. M. Kim K, *Digital Holographic Microscopy, Principles, Techniques, and Applications* (2012), Vol. 2.
8. O. Mudanyali, C. Oztoprak, D. Tseng, A. Erlinger, and A. Ozcan, "Detection of waterborne parasites using field-portable and cost-effective lensfree microscopy," Lab Chip **10**, 2419–2423 (2010).
9. E. McLeod and A. Ozcan, "Unconventional methods of imaging: Computational microscopy and compact implementations," Reports Prog. Phys. **79**, (2016).
10. H. Tobon-Maya, S. Zapata-Valencia, E. Zora-Guzmán, C. Buitrago-Duque, and J. Garcia-Sucerquia, "Open-source, cost-effective, portable, 3D-printed digital lensless holographic microscope," Appl. Opt. **60**, A205 (2021).
11. M. Sanz, J. Á. Picazo-Bueno, L. Granero, J. García, and V. Micó, "Multi-illumination single-holographic-exposure lensless Fresnel (MISHELF) microscopy using 4 channels," Imaging Appl. Opt. 2019 (COSI, IS, MATH, pcAOP) JW2A.1 (2019).
12. M. Rogalski, J. A. Picazo-Bueno, J. Winnik, P. Zdańkowski, V. Micó, and M. Trusiak, "Accurate automatic object 4D tracking in digital in-line holographic microscopy based on computationally rendered dark fields," Sci. Reports 2022 121 **12**, 1–7 (2022).
13. Y. Wu and A. Ozcan, "Lensless digital holographic microscopy and its applications in biomedicine and environmental monitoring," Methods **136**, 4–16 (2018).
14. J. Garcia-Sucerquia, "RGB digital lensless holographic microscopy," 8th Iberoam. Opt. Meet. 11th Lat. Am. Meet. Opt. Lasers, Appl. **8785**, 878572 (2013).
15. M. J. Lopera and C. Trujillo, "Linear diattenuation imaging of biological samples with digital lensless holographic microscopy," Appl. Opt. **61**, B77 (2022).
16. W. Xu, M. H. Jericho, I. A. Meinertzhagen, and H. J. Kreuzer, "Digital in-line holography for biological applications," Proc. Natl. Acad. Sci. U. S. A. **98**, 11301–11305 (2001).
17. M. J. Lopera and C. Trujillo, "Holographic optical element for digital lensless holographic microscopy's illumination," (2022).
18. M. J. Lopera and C. Trujillo, "Holographic optical element for digital lensless holographic microscopy ' s illumination," in *Digital Holography and Three Dimensional Imaging* (n.d.), Vol. 2, pp. 7–8.
19. M. J. Lopera and C. Trujillo, "Linear diattenuation sensitive lens-free holographic microscope," (2022).
20. M. J. Lopera and C. Trujillo, "Polarimetric microscope web application for simulated and



- experimental retrieval of polarimetric properties of biological samples," *Opt. Pura y Apl.* **55**, 51077 (2022).
21. M. J. Lopera, A. Pabón, and C. A. Trujillo, "Single-shot dual-wavelength Polarized Microscope to detect Malaria-infected Erythrocytes via birefringence response," *CLEO 2021 OSA 2021* (2021).
 22. M. J. (Universidad E. Lopera and C. (Universidad E. Trujillo, "Bright field polarimetric microscope web application," in *XVII ENO VIII CANCOA (Encuentro Nacional de Optics, Conferencia Andina y Del Caribe En Óptica y Sus Aplicaciones)* (2021).
 23. M. J. Lopera and C. Trujillo, "Holographic point source for digital lensless holographic microscopy," *Opt. Lett.* **47**, 2862 (2022).
 24. C. Trujillo and M. J. Lopera, "Portable cellphone-based digital lensless holographic microscope," *Front. Opt. + Laser Sci.* 2021 (2021), Pap. JTh5A.14 JTh5A.14 (2021).
 25. M. Montoya, M. J. Lopera, and C. Trujillo, "Learning-based autofocusing regression model for Digital Lensless Holographic Microscopy," (2022).
 26. M. J. Lopera and C. Trujillo, "Linear diattenuation sensitive lens-free holographic microscope," in *Digital Holography and 3-D Imaging 2022* (n.d.).
 27. R. Hooke, *Micrographia* ([The Royal Society]], 1665).
 28. E. Hecht, *Optics* (Addison-Wesley, 2002).
 29. H. K. V Lotsch, W. T. Rhodes, E. B. A. Adibi, T. Asakura, T. W. Hänsch, T. Kamiya, F. Krausz, B. Monemar, H. Venghaus, H. Weber, H. Weinfurter, and W. T. Rhodes, *Digital Holographic Microscopy* (2009).
 30. A. Ozcan and E. McLeod, "Lensless Imaging and Sensing," *Annu. Rev. Biomed. Eng.* **18**, 77–102 (2016).
 31. W. Bishara, T.-W. Su, A. F. Coskun, and A. Ozcan, "Lensfree on-chip microscopy over a wide field-of-view using pixel super-resolution," *Opt. Express* **18**, 11181 (2010).
 32. M. Özcan and M. Bayraktar, "Digital holography image reconstruction methods," *Pract. Hologr. XXIII Mater. Appl.* **7233**, 72330B (2009).
 33. L. Hervé, D. C. A. Kraemer, O. Cioni, O. Mandula, M. Menneteau, S. Morales, and C. Allier, "Alternation of inverse problem approach and deep learning for lens-free microscopy image reconstruction," *Sci. Reports 2020 101* **10**, 1–12 (2020).
 34. A. Ozcan and U. Demirci, "Ultra wide-field lens-free monitoring of cells on-chip," *Lab Chip* **8**, 98–106 (2007).
 35. S. O. Isikman, I. Sencan, O. Mudanyali, W. Bishara, C. Oztoprak, and A. Ozcan, "Wide field-of-view lensless imaging of *Caenorhabditis Elegans* on a chip," in *Optics InfoBase Conference Papers* (Optical Society of America (OSA), 2010), p. AMC5.
 36. X. Cui, L. M. Lee, X. Heng, W. Zhong, P. W. Sternberg, D. Psaltis, and C. Yang, "Lensless high-resolution on-chip optofluidic microscopes for *Caenorhabditis elegans* and cell imaging," *Proc. Natl. Acad. Sci.* **105**, 10670–10675 (2008).
 37. A. Shanmugam and C. D. Salthouse, "Lensless fluorescence imaging with height calculation," *J. Biomed. Opt.* **19**, 016002 (2014).
 38. A. F. Coskun, I. Sencan, T.-W. Su, and A. Ozcan, "Wide-field lensless fluorescent microscopy using a tapered fiber-optic faceplate on a chip," *Analyst* **136**, 3512–3518 (2011).
 39. A. Yurt, A. Lambrechts, D. Braeken, L. Lagae, R. Stahl, V. Reumers, and Z. Luo, "Pixel super-resolution for lens-free holographic microscopy using deep learning neural networks," *Opt. Express*, Vol. 27, Issue 10, pp. 13581–13595 **27**, 13581–13595 (2019).



40. M. Wang, S. Feng, and J. Wu, "Resolution-enhanced digital in-line holographic microscope with segmentation and pixel super-resolution technique," **10558**, 105580J (2018).
41. H. J. Kreuzer, N. Pomerleau, K. Blagrove, and M. H. Jericho, "Digital in-line holography with numerical reconstruction," *SPIE Interferom. '99 Tech. Technol.* **3744**, 65–74 (1999).
42. T. A. CARLOS ALEJANDRO, R. A. JHON FREDY, and G. S. JORGE IVAN, "CO7620179 MICROSCOPIO, HOLOGRÁFICO SIN LENTES (MHDSL) Y MÉTODO PARA VISUALIZAR MUESTRAS," (2016).
43. J. W. Goodman, "Introduction to Fourier optics," (1968).
44. C. Trujillo, P. Piedrahita-Quintero, and J. Garcia-Sucerquia, "Digital lensless holographic microscopy: numerical simulation and reconstruction with ImageJ," *Appl. Opt.* **59**, 5788 (2020).
45. P. Piedrahita-Quintero, C. Trujillo, and J. García-Sucerquia, "Digital Lensless Holographic Microscopy plugin for ImageJ," <https://unal-optodigital.github.io/DLHM/>.
46. C. Trujillo and J. Garcia-Sucerquia, "Numerical dark field illumination applied to experimental digital lensless holographic microscopy for reconstructions with enhanced contrast," *Opt. Lett.* **43**, (2018).
47. L. Huang, T. Liu, X. Yang, Y. I. Luo, Y. Rivenson, and A. Ozcan, "Holographic image reconstruction with phase recovery and autofocusing using recurrent neural networks," (2021).
48. A. Ozcan, B. Bai, D. Karalli, H. Wang, H. Fu, J. FitzGerald, K. de Haan, T. Liu, Y. Rivenson, Y. Luo, Y. Zhang, Y. Rivenson, Y. Luo, Y. Luo, Y. Luo, H. Wang, H. Wang, H. Wang, D. Karalli, H. Fu, Y. Zhang, Y. Zhang, Y. Zhang, J. FitzGerald, A. Ozcan, A. Ozcan, A. Ozcan, and A. Ozcan, "Deep-learning-enabled Holographic Polarization Microscopy," *Conf. Lasers Electro-Optics* (2021), Pap. ATh4F.5 ATh4F.5 (2021).
49. L. Bruslind and Open Oregon State, "Microscopes | Microbiology," <http://library.open.oregonstate.edu/microbiology/chapter/microscopes/>.
50. C. Cano, "TESIS DE MAESTRÍA: Diseño e implementación de un microscopio de luz polarizada para la medición cuantitativa de propiedades polarimétricas en muestras biológicas," Universidad EAFIT (2017).
51. E. Collett, *Field Guide to Polarization*, Volume FG0 (SPIE Field Guides, 2005).
52. I, C. Yu, R. Chen, J. J. Li, J. J. Li, M. Drahansky, M. . Paridah, A. Moradbak, A. . Mohamed, H. abdulwahab taiwo Owolabi, FolaLi, M. Asniza, S. H. . Abdul Khalid, T. Sharma, N. Dohare, M. Kumari, U. K. Singh, A. B. Khan, M. S. Borse, R. Patel, A. Paez, A. Howe, D. Goldschmidt, C. Corporation, J. Coates, and F. Reading, "Phase and Polarization Contrast Methods by Use of Digital Holographic Microscopy: Applications to Different Types of Biological Samples," *Intech i*, 13 (2012).
53. P. M. Tripathi and S. K. Tiwari, "SOCIO-ECONOMIC CHALLENGES OF GLOBALIZATION," *Indian J. Polit. Sci.* **69**, 717–725 (n.d.).
54. Centers for Disease Control and Prevention, "CDC and Malaria in the United States.," (n.d.).
55. C.-C. for D. C. and Prevention, "CDC - Malaria - About Malaria - Where Malaria Occurs," (2020).
56. C. DANE, "Defunciones no Fetales 2020," <https://www.dane.gov.co/index.php/estadisticas-por-tema/salud/nacimientos-y-defunciones/defunciones-no-fetales/defunciones-no-fetales-2020>.



57. F. Coral-Montenegro, "Trabajos libres XVI Congreso Colombiano de Parasitología y Medicina Tropical," (n.d.).
58. S. Seo, T. W. Su, D. K. Tseng, A. Erlinger, and A. Ozcan, "Lensfree holographic imaging for on-chip cytometry and diagnostics," *Lab Chip* **9**, 777–787 (2009).
59. D. K. Das, R. Mukherjee, and C. Chakraborty, "Computational microscopic imaging for malaria parasite detection: A systematic review," *J. Microsc.* **260**, 1–19 (2015).
60. C. W. Pirmstill and G. L. Coté, "Malaria Diagnosis Using a Mobile Phone Polarized Microscope," *Sci. Rep.* **5**, 1–13 (2015).
61. C. A. Trujillo Anaya, "Improved-performance digital holographic microscopy," (2018).
62. P. Langehanenberg, G. von Bally, and B. Kemper, "Autofocusing in digital holographic microscopy," *3D Res.* 2011 21 **2**, 1–11 (2011).
63. C. Trujillo and J. Garcia-Sucerquia, "Cooperative execution of auto-focusing metrics in digital lensless holographic microscopy for internal-structured samples," *Appl. Opt.* Vol. 56, Issue 21, pp. 5877–5882 **56**, 5877–5882 (2017).
64. C. Yourassowsky, C. Schockaert, F. Dubois, and N. Callens, "Focus plane detection criteria in digital holography microscopy by amplitude analysis," *Opt. Express*, Vol. 14, Issue 13, pp. 5895–5908 **14**, 5895–5908 (2006).
65. M. Fatih Toy, S. Richard, J. Kühn, A. Franco-Obregón, M. Egli, C. Depeursinge, N. J. Penley, C. P. Schafer, and J. F. Bartoe, "Enhanced robustness digital holographic microscopy for demanding environment of space biology," *Biomed. Opt. Express*, Vol. 3, Issue 2, pp. 313–326 **3**, 313–326 (2012).
66. K. Jeong, M. J. Lopera, J. J. Turek, and D. D. Nolte, "Common-path interferometer for digital holographic Doppler spectroscopy of living biological tissues," <https://doi.org/10.1117/1.JBO.26.3.030501> **26**, 030501 (2021).
67. C. A. Trujillo and J. Garcia-Sucerquia, "Automatic method for focusing biological specimens in digital lensless holographic microscopy," *Opt. Lett.* Vol. 39, Issue 9, pp. 2569–2572 **39**, 2569–2572 (2014).
68. C. Trujillo and J. Garcia-Sucerquia, "Comparative analysis of the modified enclosed energy metric for self-focusing holograms from digital lensless holographic microscopy," *Appl. Opt.* **54**, 5102 (2015).
69. Z. Xu, Z. Ren, and E. Y. M. Lam, "Autofocusing in digital holography using deep learning," **56** (2018).
70. A. Ozcan and TedXBigApple, "TEDxBigApple - Aydogan Ozcan - Microscopy on a Cellphone: An Emerging Telemedicine Platform - YouTube," <https://www.youtube.com/watch?v=6ewdosy5aOk&t=77s>.
71. K. T. Ivan, "The One OS to Rule Them All - 33 Android vs iOS Market Share Stats," <https://kommandotech.com/statistics/android-vs-ios-market-share/>.
72. Technostacks, "Top 10 Mobile App Development Frameworks in 2022 | Technostacks," <https://technostacks.com/blog/mobile-app-development-frameworks/>.
73. S. Jurado and M. J. Lopera, "Repository DLHM-App," <https://github.com/MrAgeo/DLHM-App>.
74. O. K. Ersoy, "Diffraction, fourier optics, and imaging," 413 (2007).
75. P. Piedrahita-Quintero, C. Trujillo, and J. Garcia-Sucerquia, "JDiffracton: A GPGPU-accelerated JAVA library for numerical propagation of scalar wave fields," *Comput. Phys. Commun.* **214**, 128–139 (2017).
76. J. E. Greivenkamp, *Field Guide to Geometrical Optics* (SPIE Press, 2004).



77. J. Restrepo, J.F. , García Sucerquia, "Magnified reconstruction of digitally recorded holograms by Fresnel-Bluestein transform.," Appl. Opt. **49**, (2010).
78. Kreuzer, "HOLOGRAPHIC MICROSCOPE AND METHOD OF HOLOGRAM RECONSTRUCTION US 6,411,406 B1 ,," (1993).
79. R. Castaneda, C. Trujillo, and A. Doblas, "Video-Rate Quantitative Phase Imaging Using a Digital Holographic Microscope and a Generative Adversarial Network," Sensors 2021, Vol. 21, Page 8021 **21**, 8021 (2021).



PUBLISHED MANUSCRIPTS



Linear diattenuation imaging of biological samples with digital lensless holographic microscopy

MARIA J. LOPERA*  AND CARLOS TRUJILLO 

Applied Optics Group, Physical Sciences Department, School of Science, Universidad EAFIT, Medellín, Colombia

*Corresponding author: mloper23@eafit.edu.co

Received 23 August 2021; revised 23 October 2021; accepted 29 October 2021; posted 2 November 2021; published 18 November 2021

A digital lensless holographic microscope (DLHM) sensitive to the linear diattenuation produced by biological samples is reported. The insertion of a linear polarization-states generator and a linear polarization-states analyzer in a typical DLHM setup allows the proper linear diattenuation imaging of microscopic samples. The proposal has been validated for simulated and experimental biological samples containing calcium oxalate crystals extracted from agave leaves and potato starch grains. The performance of the proposed method is similar to that of a traditional polarimetric microscope to obtain linear diattenuation images of microscopic samples but with the advantages of DLHM, such as numerical refocusing, cost effectiveness, and the possibility of field-portable implementation. © 2021 Optical Society of America

<https://doi.org/10.1364/AO.440376>

1. INTRODUCTION

Polarization-sensitive digital holography allows simultaneous recovery of amplitude, phase, and the quantitative evaluation of polarization properties of a given sample [1]. One of the first proposals to attain a digital holography setup that provides information on the polarization state of light was in [2]. In this proposal, to recover the polarization state of the light scattered by a birefringent sample, two reference wavefronts with orthogonal polarization states were made to interfere with the object wavefront to create a digital hologram from which the said information could be recovered via numerical processing [2]. Regarding digital holographic microscopy, several approaches combining the possibility to image wave fields scattered by microscopic samples and elements to quantify the polarization state of these wave fields have been proposed [3–6]. In [3], a proposal involving implementing a polarization digital holography setup and a digital holographic microscopy setup were joined together to image the birefringence induced by internal stress in a stripped optical fiber. In [4], a system composed of two lasers, microscope objectives, multiple mirrors, and beam splitters was implemented to provide multi-imaging capability in a single-shot acquisition for full polarization information recovery. To avoid the numerical processing underlying the retrieval of information via off-axis setups, Nomura *et al.* in [5] proposed a polarimetric imaging method for 3D objects by using an on-axis phase-shifting digital holography scheme. Although the latter and similar methods have been applied in areas such as biology and medicine, their performance is still limited by one or more of the following aspects: (i) the need to

implement bulky interferometric setups, (ii) the use of lenses for magnification, and (iii) these implementations are not cost effective. To overcome the latter setbacks, in-line lensless microscopy techniques have been proposed [7,8].

Since computation has become more powerful, cheaper, and portable over the last decades, lensless microscopic techniques have emerged using simple and inexpensive hardware. These lensless microscopic techniques rely on computational methods to recover the information of unstained biological specimens [8]. The hardware simplicity of these techniques is synthesized in terms of the required elements: a divergent spherical-wave source, usually a point source, and a digital camera. Two different modalities of lensless microscopy are distinguished based on the location of the sample to the point source and the digital camera. In the first type of lensless microscopy, the sample is almost in contact with the camera. These systems are known as computational microscopy [9], and their resolution, which is comparable to the pixel size, can be improved by using super-resolution techniques [7], single-shot multi-wavelength acquisitions [10], learning-based approaches [11], or combinations of all of them [12–15]. Polarization-sensitive computational microscopy has been applied to pathological crystal [16] and birefringent synovial fluid [17] imaging. In the second type of lensless microscopy, named digital lensless holographic microscopy (DLHM) [8], the diffraction pattern of the sample, magnified during its propagation to the camera, allows the retrieval of the information of microscopic samples by using a discrete version of the scalar diffraction integral. The resolution in DLHM is dictated by the numerical aperture of the

optical system, which depends on the geometry of the optical imaging system [8]. The latter avoids the need for computationally demanding methods or sophisticated setups required in computational microscopy. DLHM has been perfected to the point that micrometric spatial resolution is routinely achieved in samples with or without internal structure with single-shot measurements [8,18]. Although further developments in this technique have been reported recently to widen its range of application, such as the implementation of compact setups for field portability [19], cost-effective implementations [20], contrast enhancement of its reconstructions [21,22], and more robust and efficient autofocus methods [23], the possibility to quantify polarization properties of samples in this imaging technique has not been reported. The need for proposals involving simple experimental setups with potential field portability and straightforward numerical processing is still a research topic in DLHM. Therefore, this paper reports a digital lensless holographic microscope that is sensitive to the linear diattenuation, or alternatively linear dichroism, produced by biological samples. This proposal requires only the insertion of two linear polarizers in a conventional DLHM setup and point-wise operations between the intensity reconstructions from two acquisitions.

2. LINEAR DIATTENUATION DIGITAL LENSLESS HOLOGRAPHIC MICROSCOPY

The proposed linear diattenuation-sensitive digital lensless holographic microscope (LD-DLHM) setup is depicted in Fig. 1. A laser beam is the illumination source of the system. A linear polarizer is used as a polarization-states generator (PSG) to assure a complete vertical polarization state for the incident beam. A divergent spherical wavefront source produces the illumination waves impinging on the sample. This point source can be built by using pinholes [8], Blu-ray pickups [24], or cone-shaped optical fibers [25], among others. The divergent spherical wavefront source must fulfill the degree of spatial coherence required to register DLHM holograms successfully [8]. A second linear polarizer, which serves as a polarization-states analyzer (PSA), is placed close to the camera. Finally, the sample and the CCD or CMOS sensor are placed at distances z and L from the point source, respectively. In the LD-DLHM, the source-to-camera distance L and the camera sensor's size W determine both the lateral resolution S and the numerical aperture NA of the imaging system according to $S \geq \lambda/2\text{NA}$

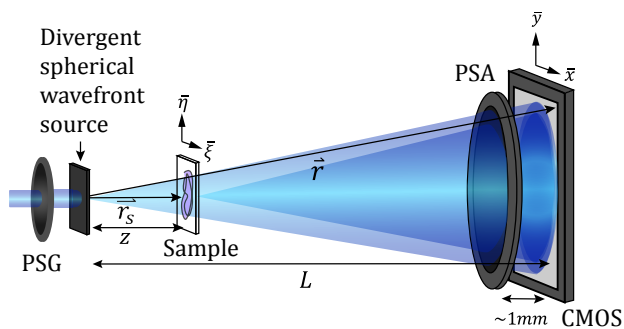


Fig. 1. Illustration of the linear diattenuation-sensitive digital lensless holographic microscope LD-DLHM setup. See text for further details.

and $\text{NA} = W/2\sqrt{(W/2)^2 + L^2}$. In turn, the source-to-sample z distance controls the system's magnification M according to $M = L/z$. The exact selection of these parameters must be determined considering the proper imaging of the microscopic samples and the insertion of the PSG and PSA in the setup.

A series of acquisitions with the PSA rotated at different angles for its transmission axis was performed to study the effect of the divergent spherical wavefront source on the resulting polarization state of the illumination wavefront before the sample. All the DLHM and LD-DLHM holograms presented in this paper were recorded with a 1024×1024 pixels Thorlabs CMOS sensor with $3.6 \mu\text{m}$ pixel pitch and a CW 473 nm laser from Lasermate Group as the light source. When the transmission axis of the PSG is perpendicular or parallel to that of the PSA, the recorded intensity is minimum or maximum, respectively; for intermediate angles between the transmission axis of the PSG and that of the PSA, intermediate intensity values are obtained. According to this, a Malus law-like [26] experiment is achieved with our proposal. These results are expected considering that the divergent spherical wavefront source, in its different versions, is composed of only refracting elements. These refracting elements modify the shape of the impinging wavefront without introducing any retardance due to its characteristic optical isotropy [27]. Therefore, no polarization-state changing properties are presented for this element; thus, the polarization state of the incident beam established by the PSG is kept up to the sample plane.

To produce digital images carrying point-wise information of linear diattenuation $D(\vec{r}_s)$ [28] with a DLHM setup such as that in Fig. 1, first S_0 and second S_1 Stokes parameters must be recovered. Then, to recover $D(\vec{r}_s)$, Eq. (1) is computed:

$$D(\vec{r}_s) = \frac{S_1}{S_0} = \frac{I_0 + I_{90}}{I_0 - I_{90}}. \quad (1)$$

In Eq. (1), I_0 and I_{90} are the transmitted intensities when the PSA transmission axis is set parallel and perpendicular to that of the PSG in a given location $\vec{r}_s = (\zeta, \eta, z)$, respectively; (ζ, η) are the coordinates at the sample plane. The complete process to compute Eq. (1) with our proposal can be summarized in three steps.

- (i) The DLHM holograms from which I_0 and I_{90} are to be recovered must be accurately acquired. The transmission angle for the PSG is set to 0° , i.e., vertical axis. Then the PSA is fixed first at 0° and then at 90° to register the two required acquisitions.
- (ii) To recover I_0 and I_{90} from the DLHM holograms acquired in (i), a numerical reconstruction process is required. A DLHM hologram could be thought of as the intensity distribution yielded from the superposition between the portions of the illumination wavefront that are diffracted by the sample and other portions that travel with no perturbation. The actual of the complex-valued diffracted wave field is performed by backpropagating a converging spherical wavefront $\exp[-i\vec{k} \cdot \vec{r}]/|\vec{r}|$ as it illuminates the resulting diffraction pattern acquired at the camera sensor, i.e., the registered DLHM hologram. In DLHM, this diffraction process can be numerically described through a scalar diffraction formula [29]:

$$S(\vec{r}_s) = \frac{z}{i\lambda} \int_{\text{Digital Camera}} I(\vec{r}) \frac{\exp[-i\vec{k} \cdot \vec{r}]}{|\vec{r}|} \frac{\exp[-i\vec{k} \cdot (\vec{r} - \vec{r}_s)]}{|\vec{r} - \vec{r}_s|} d\vec{r}. \quad (2)$$

In Eq. (2), $\vec{r} = (x, y, z)$ is a vector denoting a given position at the camera plane, and $I(\vec{r})$ is the DLHM hologram. The exact details of the most suitable numerical reconstruction in DLHM can be read in [30,31]. Equation (2) is a complex-valued quantity from which one can compute the intensity $S(\vec{r}_s)S^*(\vec{r}_s)$ at the sample plane. By applying Eq. (2) over the DLHM holograms acquired in (i), I_{90} and I_0 are obtained.

- (iii) With the I_{90} and I_0 transmittances recovered in (ii), the subsequent calculation of a sample's point-wise linear diattenuation response can be straightforwardly performed by using Eq. (1).

3. RESULTS OF THE PROPOSED METHOD ON MODELED AND EXPERIMENTAL SAMPLES

For initial testing purposes, a numerically modeled response of the proposed LD-DLHM was implemented. The numerically implemented sample is composed of chopstick-like objects presenting negative linear diattenuation in a transparent non-polarizing medium. For this sample, I_0 displays the information of the objects with low-intensity values in a bright background [Fig. 2(a)]. Conversely, I_{90} displays the information of the objects with high-intensity values in a dark background [Fig. 2(b)]. As expected, after applying Eq. (1), a linear diattenuation image of the sample presenting negative diattenuation for the chopstick-like objects is obtained [Fig. 2(c)]. The image in Fig. 2(c) will serve as a reference linear diattenuation image of this sample when testing it in the numerical LD-DLHM. To build DLHM holograms containing information for both I_0 and I_{90} for the selected numerical sample, a procedure connecting scalar diffraction theory and polarimetric calculations has been designed. Considering the definition of a Jones vector, we can split the numerical propagation procedure for two different matrices: one containing the information of the horizontal $S(\vec{r}_s)_x$ component of the complex wave field at a given location $S(\vec{r}_s)$, and the other containing the information of its vertical component $S(\vec{r}_s)_y$. A point-wise Jones calculus is then performed to determine the changes in the polarization state of light at the sample plane and then at the PSA plane. At the sample plane, a matrix multiplication between the Jones matrix of a point $\mathfrak{M}(\vec{r}_s)$ and the Jones vector representing the polarization state of the incident wavefront at that same point $[S(\vec{r}_s)_x^{\text{before}}, S(\vec{r}_s)_y^{\text{before}}]$ will yield the polarization state of the wavefront just after the sample plane $[S(\vec{r}_s)_x^{\text{after}}, S(\vec{r}_s)_y^{\text{after}}]$, i.e.,

$$\begin{bmatrix} S(\vec{r}_s)_x^{\text{after}} \\ S(\vec{r}_s)_y^{\text{after}} \end{bmatrix} = \mathfrak{M}(\vec{r}_s) \times \begin{bmatrix} S(\vec{r}_s)_x^{\text{before}} \\ S(\vec{r}_s)_y^{\text{before}} \end{bmatrix}. \quad (3)$$

In Eq. (3), $\mathfrak{M}(\vec{r}_s)$ is the identity matrix $[1, 0; 0, 1]$ for points representing the non-polarizing transparent medium and $[0, 1; 0, 1]$ for points representing the chopstick-like objects with negative diattenuation. Depending upon the orientation of the PSG, $[S(\vec{r}_s)_x^{\text{before}}, S(\vec{r}_s)_y^{\text{before}}]$ could be that representing horizontal polarization $[1, 0]$ or vertical polarization $[0, 1]$.

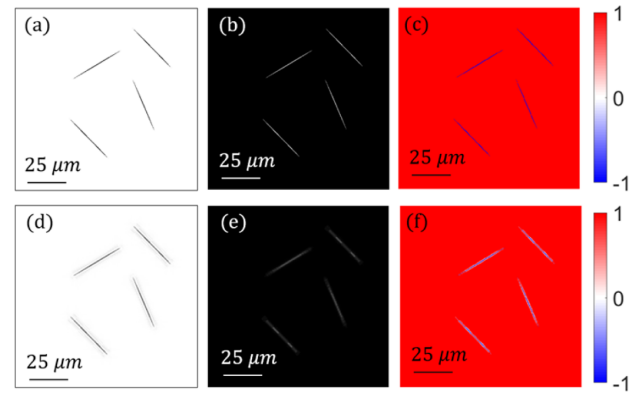


Fig. 2. Modeled response of a numerical sample presenting negative diattenuation via our proposed LD-DLHM. (a)–(c) Modeled $T_{\max}(\vec{r}_s)$, $T_{\min}(\vec{r}_s)$, and $D(\vec{r}_s)$ used as references. (d)–(f) Modeled $T_{\max}(\vec{r}_s)$, $T_{\min}(\vec{r}_s)$, and $D(\vec{r}_s)$ via our proposed LD-DLHM. See text for further details.

Once $[S(\vec{r}_s)_x^{\text{after}}, S(\vec{r}_s)_y^{\text{after}}]$ is computed for every point in the sample plane, each independent component is propagated to the PSA plane via a discrete implementation of the Rayleigh–Sommerfeld diffraction formula for high numerical apertures, which is mainly developed for DLHM [21,32]. Next, to determine the point-wise change of light's polarization state at this plane due to the PSA, Eq. (3) is computed again. For all points in the PSA plane, $\mathfrak{M}(\vec{r}_s)$ is either $[1, 0; 0, 0]$ or $[0, 0; 0, 1]$ for horizontal or vertical orientations of the linear polarizer, respectively. Then, each resulting component is propagated to the camera plane via a discrete version of the angular spectrum formalism [33]. To calculate the point-wise intensity values composing the DLHM hologram, Eq. (4) is computed:

$$I_{\text{mod}}(\vec{r}) = \sqrt{S(\vec{r})_x^2 + S(\vec{r})_y^2}. \quad (4)$$

Once the latter procedure has been executed to build the DLHM holograms containing the information of I_{90} and I_0 , these two intensity distributions can be recovered via Eq. (2). Finally, the modeled linear diattenuation response of the numerical sample can be computed via Eq. (1). In Figs. 2(d)–(f), the modeled I_0 , I_{90} , and $D(\vec{r}_s)$ via LD-DLHM are presented. When compared to the reference images, (a)–(c), the intensity images obtained by our proposal are recovered adequately except for some noise surrounding the chopstick-like objects, which is due to the diffraction-associated phenomena underlying the DLHM. The latter confirms our proposal for imaging ideal microscopic objects presenting negative linear diattenuation.

To experimentally validate our proposal, three biological samples were studied. Initially, a sample containing calcium oxalate crystals was imaged using the proposed LD-DLHM. This sample was obtained from the maceration of the leaves of an *Agave Chiapensis* plant. The maceration was centrifuged for 1 min at 4500 rpm to obtain sediment with high crystal density. In addition to crystals, this complex sample contains other organic components such as chlorophyll, inulin, and agave fibers. An image obtained with a bright-field microscope with a depth of field of approximately 15 μm and a numerical aperture of 0.1 of this sample is presented in Fig. 3(a). For this sample, the intensity recovered via traditional DLHM and the

linear diattenuation response with the proposed LD-DLHM system are depicted in Figs. 3(b) and (d), respectively. For this validation, the source-to-sample distance was 3 mm, and the source-to-camera distance was 20 mm, yielding a numerical aperture of 0.0896, a lateral resolution of $3.21\ \mu\text{m}$, and a depth of field of $62\ \mu\text{m}$ for both the DLHM and LD-DLHM systems. As can be seen in the zoom-in areas of Fig. 3, the visualization of the oxalate crystal by our proposal, (d), shows the accurate linear diattenuation response of the sample, compared with the polarimetric bright-field image in (c). The results in Fig. 3(d) suffer from some noise that is not present in Fig. 3(c). Two factors explain the latter: (i) the high degree of temporal coherence of the illumination used in DLHM, which is not used in bright-field microscopy; (ii) the required numerical propagation procedure to recover the complex wave field at the sample plane, which adds some artifacts in the intensity reconstructions due to the nature of the sample. The sample containing the calcium oxalate crystals in this experiment contains pure phase objects, as already described. Therefore, in a conventional bright-field microscope, these transparent elements will not be imaged. On the other hand, as DLHM-based techniques are sensitive to phase elements, their presence will distort the background of the reconstructions after the numerical propagation procedure, a problem that has been covered in different works [21,22]. Moreover, the measurement of the linear diattenuation with our proposal shows that this sample presents negative diattenuation, which agrees with other already reported works [17,35]. This measurement cannot be done via traditional DLHM; therefore, the capability of our proposal to provide complementary information of samples with polarizing properties is demonstrated.

The detection of crystals such as calcium oxalate represents a significant feature that allows our proposal to be used in biomedical fields to detect and diagnose certain diseases. For instance, the retention of calcium oxalate crystals in the

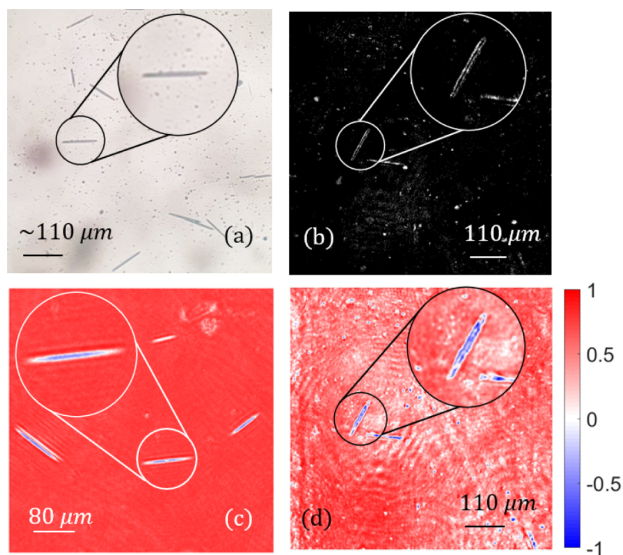


Fig. 3. Linear diattenuation response of an experimental sample with calcium oxalate crystals. (a) Intensity bright-field image of the sample. (b) Intensity reconstruction obtained via conventional DLHM. (c) Linear diattenuation response of the sample, using a polarimetric bright-field microscope [34]. (d) Linear diattenuation response via the proposed LD-DLHM of the same sample in (b).

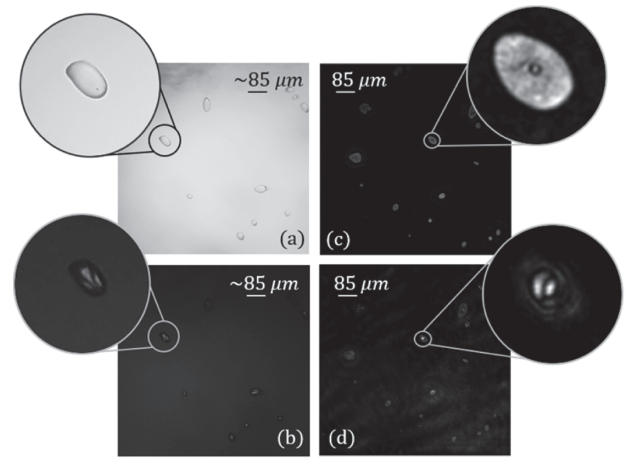


Fig. 4. Intensity images of a starch grains sample. (a) Intensity bright-field image. (b) Polarized bright-field intensity image (I_{90}). (c) Intensity reconstruction via traditional DLHM. (d) I_{90} intensity image of the potato starch sample with the proposed LD-DLHM.

kidney is an essential early step in renal stone formation [36]; these crystals are expelled in the urine and can be detected with polarimetry techniques. On the other hand, gout is a common and debilitating disease where monosodium urate (MSU) crystals deposit and elicit inflammation in a joint. Diagnosis of gout relies on detecting the MSU crystals with a polarized light microscope in synovial fluid [16,17,37]. MSU has similar optical properties as calcium oxalate [16]; in particular, these crystals present inverse linear diattenuation [17], a property that has been validated to be detected and quantified by our LD-DLHM proposal. In short, identifying monosodium and calcium oxalate crystals is clinically relevant when performing a synovial fluid or urine analysis for crystals, and both organic components can be imaged with the proposed LD-DLHM.

To further test the LD-DLHM proposal, a sample containing starch grains was used. Potato tissues were crushed and then dried to prepare this sample. The resulting powder was later spread in a sample holder and fixed with pure ethanol. The results for the starch grains sample are shown in Fig. 4. In Fig. 4(a), a bright-field image of the sample is presented. In (b), a polarimetric bright-field image is shown. The intensity image recovered via traditional DLHM for the sample is presented in (c). Figure 4(d) shows the I_{90} intensity obtained via the proposed LD-DLHM. The geometrical parameters for the DLHM and LD-DLHM in this experiment are those used to image the calcium oxalate crystals. When potato starch granules are imaged with polarized light, they exhibit different birefringent patterns in the form of lobes creating Maltese crosses [38]. These features cannot be retrieved in the intensity image obtained via conventional bright-field microscopy or DLHM [(a) and (c)]. In contrast, the visualization of the Maltese crosses in both (b) and (d) is expected considering the positive birefringence in this sample, which indicates that the starch grain has a high degree of aligned molecules or crystals [38]. Therefore, the proposed LD-DLHM provides more information on samples with a polarizing response when compared to traditional DLHM.

To compare the performance of our method against other related proposals to potato starch characterization, the intensity

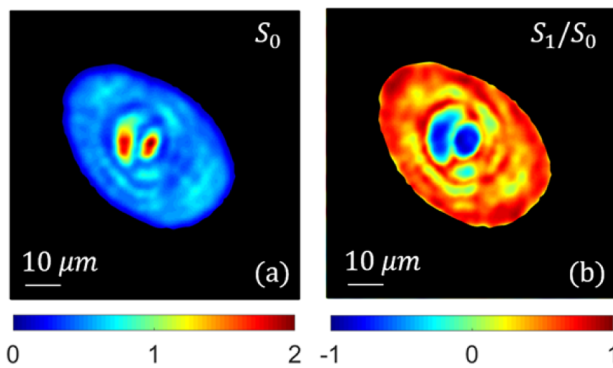


Fig. 5. (a) Total Stokes intensity S_0 calculation for one single starch grain. (b) Linear diattenuation S_1/S_0 of the same starch grain.

images for the first Stokes parameters and the linear diattenuation [Eq. (1)] are also presented. The intensity Stokes parameter S_0 of one single grain from the sample is presented in Fig. 5(a). It can be observed in this image that the starch grain lobes present higher intensity, which is due to the increase in the crystalline order of the starch granules in this section of the sample [39]. Stokes parameters of starch granules demonstrate that an excitation pulse of linearly polarized light is transformed into right or left elliptically polarized light, which can be appreciated as a negative linear diattenuation [40]. The linear diattenuation of this starch grain is shown in (b).

The visualization of these Maltese crosses, also called polarization crosses, with the proposed LD-DLHM represents an essential feature of the device and confirms that it can be a useful tool in biology areas where this polarization property is commonly found. For example, the proposed LD-DLHM could be used to detect zooplankton or veliger in plankton samples [41,42] or to detect drug-induced changes in alveolar type II cells [43].

Finally, to validate our proposal to recover linear diattenuation information of an intricate biological specimen, a sample containing a layer of onion cells has been imaged with our LD-DLHM system. In Fig. 6, the results for I_0 , I_{90} , and the diattenuation response of this biological sample are presented in (a), (b), and (c), respectively. For this experiment, the source-to-sample distance was 3.7 mm, and the source-to-camera distance was 12 mm, yielding a numerical aperture of 0.15 and a lateral resolution of $1.57 \mu\text{m}$. As can be observed in the zoom-in areas of Fig. 6(c), the cell wall of these specimens presents strong negative linear diattenuation, in contrast with the inner structures of the cells, which present low positive or even no diattenuation response. These results agree with the theoretical expectation

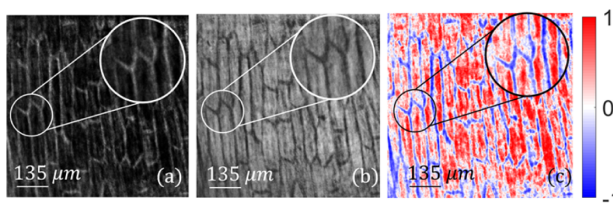


Fig. 6. Intensity images and diattenuation response recovered via our LD-DLHM of a sample containing a layer of onion cells. (a) I_0 intensity image, (b) I_{90} intensity image, and (c) diattenuation response of the sample.

considering that the cell wall is composed of cellulose fiber, polysaccharides, and proteins [44]; since these compounds, particularly the cellulose fiber, are composed of well-aligned molecules, a strong dichroic response is expected for these parts of the specimen due to their intrinsic anisotropic absorption [45]. The results reported for the oxalate crystals of agave plants, the potato starch grains, and the layer of onion cells validate our proposal to successfully recover the linear diattenuation response of biological specimens.

4. CONCLUSION

In this paper, a linear diattenuation-sensitive digital lensless holographic microscope has been presented. The proposal considers the insertion of two linear polarizers in the conventional DLHM setup: one before the point source working as a PSG and the other placed after the sample plane, just before the camera sensor, working as a PSA. To produce linear diattenuation images of static microscopic samples, a two-shot procedure involving acquisitions at the maximum and minimum intensities, which are obtained by rotating the PSA from 0° to 90° , is performed before straightforward numerical processing. The proposal has been validated with a numerically modeled sample of objects presenting negative diattenuation response and experimental biological samples of calcium oxalate crystals, starch grains, and a layer of onion cells. The method has successfully recovered polarimetric information of specimens that cannot be retrieved via conventional DLHM. Regarding the retrieval of intensity images, our proposal has a performance similar to that of the traditional polarimetric microscope but with superior advantages, owed to holographic techniques such as the numerical refocusing of the samples. Also, our proposal widens the range of applications of DLHM concerning the study of biological samples presenting birefringent behavior, which could boost the application of this cost-effective field-portable technique in medicine and biology.

Funding. Universidad EAFIT.

Acknowledgment. The authors acknowledge the support by Vicerrectoría de Descubrimiento y Creación from Universidad EAFIT. M. Lopera acknowledges the collaboration of the biology department of Universidad EAFIT to obtain the oxalate crystals sample.

Disclosures. The authors declare no conflicts of interest.

Data Availability. Data underlying the results presented in this paper are not publicly available at this time but may be obtained from the authors upon reasonable request.

REFERENCES

1. G. Coppola and M. A. Ferrara, "Polarization-sensitive digital holographic imaging for characterization of microscopic samples: recent advances and perspectives," *Appl. Sci.* **10**, 4520 (2020).
2. T. Colomb, P. Dahlgren, D. Beghuin, E. Cuche, P. Marquet, and C. Depeursinge, "Polarization imaging by use of digital holography," *Appl. Opt.* **41**, 27–37 (2002).
3. T. Colomb, F. Dürr, E. Cuche, P. Marquet, H. G. Limberger, R.-P. Salathé, and C. Depeursinge, "Polarization microscopy by use of digital holography: application to optical-fiber birefringence measurements," *Appl. Opt.* **44**, 4461–4469 (2005).
4. T. D. Yang, K. Park, Y. G. Kang, K. J. Lee, B.-M. Kim, and Y. Choi, "Single-shot digital holographic microscopy for quantifying a

- spatially-resolved Jones matrix of biological specimens," *Opt. Express* **24**, 29302–29311 (2016).
5. T. Nomura, B. Javidi, S. Murata, E. Nitanai, and T. Numata, "Polarization imaging of a 3D object by use of on-axis phase-shifting digital holography," *Opt. Lett.* **32**, 481–483 (2007).
 6. Y. Kim, J. Jeong, J. Jang, M. W. Kim, and Y. Park, "Polarization holographic microscopy for extracting spatio-temporally resolved Jones matrix," *Opt. Express* **20**, 9948–9955 (2012).
 7. W. Bishara, U. Sikora, O. Mudanyali, T. W. Su, O. Yaglidere, S. Luckhart, and A. Ozcan, "Holographic pixel super-resolution in portable lensless on-chip microscopy using a fiber-optic array," *Lab Chip* **11**, 1276–1279 (2011).
 8. J. Garcia-Sucerquia, W. Xu, S. K. Jericho, P. Klages, M. H. Jericho, and H. J. Kreuzer, "Digital in-line holographic microscopy," *Appl. Opt.* **45**, 836–850 (2006).
 9. A. Ozcan, "Computational microscopy, sensing, and diagnostics (presentation video)," *Proc. SPIE* **9166**, 91660K (2014).
 10. M. Sanz, J. A. Picazo-Bueno, J. García, and V. Micó, "Improved quantitative phase imaging in lensless microscopy by single-shot multi-wavelength illumination using a fast convergence algorithm," *Opt. Express* **23**, 21352–21365 (2015).
 11. S. Banik, S. K. Melanthota, Arbaaz, J. M. Vaz, V. M. Kadambalithaya, I. Hussain, S. Dutta, and N. Mazumder, "Recent trends in smartphone-based detection for biomedical applications: a review," *Anal. Bioanal. Chem.* **413**, 2389–2406 (2021).
 12. C. Fournier, F. Jolivet, L. Denis, N. Verrier, E. Thiebaut, C. Allier, and T. Fournel, "Pixel super-resolution in digital holography by regularized reconstruction," *Appl. Opt.* **56**, 69–77 (2017).
 13. Z. Xiong, J. E. Melzer, J. Garan, and E. McLeod, "Optimized sensing of sparse and small targets using lens-free holographic microscopy," *Opt. Express* **26**, 25676–25692 (2018).
 14. Z. Luo, A. Yurt, R. Stahl, A. Lambrechts, V. Reumers, D. Braeken, and L. Lagae, "Pixel super-resolution for lens-free holographic microscopy using deep learning neural networks," *Opt. Express* **27**, 13581–13595 (2019).
 15. X. Wu, J. Sun, J. Zhang, L. Lu, R. Chen, Q. Chen, and C. Zuo, "Wavelength-scanning lensfree on-chip microscopy for wide-field pixel-super-resolved quantitative phase imaging," *Opt. Lett.* **46**, 2023–2026 (2021).
 16. B. Bai, H. Wang, T. Liu, Y. Rivenson, J. FitzGerald, and A. Ozcan, "Pathological crystal imaging with single-shot computational polarized light microscopy," *J. Biophoton.* **13**, e201960036 (2020).
 17. Y. Zhang, S. Y. C. Lee, Y. Zhang, D. Furst, J. Fitzgerald, and A. Ozcan, "Wide-field imaging of birefringent synovial fluid crystals using lens-free polarized microscopy for gout diagnosis," *Sci. Rep.* **6**, 28793 (2016).
 18. J. Garcia-Sucerquia, D. C. Alvarez-Palacio, and H. J. Kreuzer, "High resolution Talbot self-imaging applied to structural characterization of self-assembled monolayers of microspheres," *Appl. Opt.* **47**, 4723–4728 (2008).
 19. S. Rawat, S. Komatsu, A. Markman, A. Anand, and B. Javidi, "Compact and field-portable 3D printed shearing digital holographic microscope for automated cell identification," *Appl. Opt.* **56**, D127–D133 (2017).
 20. H. Tobon-Maya, S. Zapata-Valencia, E. Zora-Guzmán, C. Buitrago-Duque, and J. Garcia-Sucerquia, "Open-source, cost-effective, portable, 3D-printed digital lensless holographic microscope," *Appl. Opt.* **60**, A205–A214 (2021).
 21. C. Trujillo and J. Garcia-Sucerquia, "Numerical dark field illumination applied to experimental digital lensless holographic microscopy for reconstructions with enhanced contrast," *Opt. Lett.* **43**, 4096–4099 (2018).
 22. H. Tobon, C. Trujillo, and J. Garcia-Sucerquia, "Preprocessing in digital lensless holographic microscopy for intensity reconstructions with enhanced contrast," *Appl. Opt.* **60**, A215–A221 (2021).
 23. C. Trujillo and J. Garcia-Sucerquia, "Cooperative execution of auto-focusing metrics in digital lensless holographic microscopy for internal-structured samples," *Appl. Opt.* **56**, 5877–5882 (2017).
 24. S. Amann, M. von Witzleben, and S. Breuer, "3D-printable portable open-source platform for low-cost lens-less holographic cellular imaging," *Sci. Rep.* **9**, 11260 (2019).
 25. B. Patiño-Jurado, J. F. Botero-Cadavid, and J. Garcia-Sucerquia, "Cone-shaped optical fiber tip for cost-effective digital lensless holographic microscopy," *Appl. Opt.* **59**, 2969–2975 (2020).
 26. E. Hecht, *Optics*, 4th ed. (2001), Vol. 1.
 27. M. Born, E. Wolf, A. B. Bhatia, P. C. Clemmow, D. Gabor, A. R. Stokes, A. M. Taylor, P. A. Wayman, and W. L. Wilcock, *Principles of Optics* (Cambridge University, 1999).
 28. M. Bass, *Handbook of Optics, Volume I: Geometrical and Physical Optics, Polarized Light, Components and Instruments* (1996).
 29. J. W. Goodman, *Introduction to Fourier Optics* (Roberst & Company, 2005).
 30. M. H. Jericho and H. J. Kreuzer, "Point source digital in-line holographic microscopy," in *Coherent Light Microscopy*, P. Ferraro, A. Wax, and Z. Zalevsky, eds. (2011), pp. 3–30.
 31. C. Trujillo, P. Piedrahita-Quintero, and J. Garcia-Sucerquia, "Digital lensless holographic microscopy: numerical simulation and reconstruction with ImageJ," *Appl. Opt.* **59**, 5788–5795 (2020).
 32. J. F. Restrepo and J. Garcia Sucerquia, "Magnified reconstruction of digitally recorded holograms by Fresnel-Bluestein transform," *Appl. Opt.* **49**, 6430–6435 (2010).
 33. P. Piedrahita-Quintero, C. Trujillo, and J. Garcia-Sucerquia, "JDiffraction: a GPGPU-accelerated JAVA library for numerical propagation of scalar wave fields," *Comput. Phys. Commun.* **214**, 128–139 (2017).
 34. M. J. Lopera, A. Pabón, and C. A. Trujillo, "Single-shot dual-wavelength polarized microscope to detect malaria-infected erythrocytes via birefringence response," in *Conference on Lasers and Electro-Optics (CLEO) (OSA, 2021)*.
 35. F. Palacios, O. Font, G. Palacios, J. Ricardo, M. Escobedo, L. Ferreira, I. Vasconcelos, M. Muramatsu, D. Soga, A. Prado, and V. Jos, "Phase and polarization contrast methods by use of digital holographic microscopy: applications to different types of biological samples," in *Holography - Basic Principles and Contemporary Applications* (InTech, 2013).
 36. M. Asselman, A. Verhulst, M. E. De Broe, and C. F. Verkoelen, "Calcium oxalate crystal adherence to hyaluronan-, osteopontin-, and CD44-expressing injured/regenerating tubular epithelial cells in rat kidneys," *J. Am. Soc. Nephrol.* **14**, 3155–3166 (2003).
 37. Y. Yoo, Y. J. Seo, M. Huh, J. H. Yoo, K. H. Yun, and S. J. Kim, "Gout and coexisting pseudogout in the knee joint," *Knee Surg. Sport. Traumatol. Arthrosc.* **19**, 553–555 (2011).
 38. X. Zhao, M. Andersson, and R. Andersson, "Resistant starch and other dietary fiber components in tubers from a high-amylose potato," *Food Chem.* **251**, 58–63 (2018).
 39. N. Mazumder, L. Y. Xiang, J. Qiu, and F.-J. Kao, "Investigating starch gelatinization through Stokes vector resolved second harmonic generation microscopy," *Sci. Rep.* **7**, 1–9 (2017).
 40. C. M. Romero, F.-J. Kao, J. Qiu, M. R. Foreman, N. Mazumder, and P. Török, "Stokes vector based polarization resolved second harmonic microscopy of starch granules," *Biomed. Opt. Express* **4**, 538–547 (2013).
 41. L. E. Johnson, "Enhanced early detection and enumeration of zebra mussel (*Dreissena* spp.) veligers using cross-polarized light microscopy," *Hydrobiologia* **312**, 139–146 (1995).
 42. S. Sabbah and N. Shashar, "Polarization contrast of zooplankton: a model for polarization-based sighting distance," *Vision Res.* **46**, 444–456 (2006).
 43. T. Haller, A. Cerrada, K. Pfaller, P. Braubach, and E. Felder, "Polarized light microscopy reveals physiological and drug-induced changes in surfactant membrane assembly in alveolar type II pneumocytes," *Biochim. Biophys. Acta, Biomembr.* **1860**, 1152–1161 (2018).
 44. D. Ye, S. Rongpipi, S. N. Kiemle, W. J. Barnes, A. M. Chaves, C. Zhu, V. A. Norman, A. Liebman-Peláez, A. Hexemer, M. F. Toney, A. W. Roberts, C. T. Anderson, D. J. Cosgrove, E. W. Gomez, and E. D. Gomez, "Preferred crystallographic orientation of cellulose in plant primary cell walls," *Nat. Commun.* **11**, 4720 (2020).
 45. A. Van Eeckhout, E. Garcia-Caurel, T. Garnatje, J. C. Escalera, M. Durfort, J. Vidal, J. J. Gil, J. Campos, and A. Lizana, "Polarimetric imaging microscopy for advanced inspection of vegetal tissues," *Sci. Rep.* **11**, 3913 (2021).

Polarimetric microscope web application for simulated and experimental retrieval of polarimetric properties of biological samples.

Aplicación web de un microscopio polarimétrico para la recuperación simulada y experimental de propiedades polarimétricas de muestras biológicas.

Maria J. Lopera * and Carlos Trujillo

*Applied Optics Group, Physical Sciences Department, School of Science, Universidad EAFIT,
Medellín, Colombia.*

✉ E-mail: mloper23@eafit.edu.co

S: miembro de SEDOPTICA / SEDOPTICA member

Received: 01/12/2021

Accepted: 20/02/2022

DOI: 10.7149/OPA.55.1.51077

ABSTRACT:

This paper reports a bright field polarimetric microscope's numerical simulation in a web application. In the main interface or layout of this software, the user can interact with the elements that compose a polarimetric microscope, such as the polarization-states generators and analyzers, the Jones matrices that make up the sample, the optical magnification of the imaging system, the numerical aperture of the instrument, and the wavelength of the illumination source. The web application includes two more layouts for experimental or synthetic data post-processing. The first one allows the computing of the dichroic response of a microscopic sample. The second layout allows computing the Stokes parameters of a light beam and its general, linear, and circular degree of polarization. The ease of use and its cross-platform portability establish our web application as a valuable tool for different teaching and research applications in the field of microscopy and polarimetry of biological samples. This web application can be accessed freely in[1].

Key words: Polarimetry, polarization, polarized, , microscopy, web app, user interface, software, modeling, simulation.

RESUMEN: En este artículo se reporta la simulación numérica de un microscopio polarimétrico de campo brillante en una aplicación web. En la interfaz principal o *layout* de este software, el usuario puede interactuar con los elementos que componen un microscopio polarimétrico, como los generadores y analizadores de estados de polarización, las matrices de Jones que componen la muestra, la magnificación óptica del sistema formador de imagen, la apertura numérica del instrumento y la longitud de onda de la fuente de iluminación. La aplicación web incluye dos *layouts* adicionales para el procesamiento posterior de datos experimentales o sintéticos. El primero permite calcular la respuesta dicróica de una muestra microscópica. El segundo *layout* permite calcular los parámetros de Stokes de un haz de luz y su grado de polarización general, lineal y circular. La facilidad de uso y su portabilidad multiplataforma establecen a nuestra aplicación web como una herramienta valiosa para diferentes aplicaciones en docencia e investigación en el campo de la microscopía y la polarimetría de muestras biológicas. Esta aplicación web se puede acceder libremente a través de[1].

Palabras clave: Polarimetría, polarización, polarizado, microscopía, aplicación web, interfaz de usuario, software, modelado, simulación.

REFERENCES AND LINKS / REFERENCIAS Y ENLACES

- [1] M. J. Lopera Acosta and C. A. Trujillo, "Bright Field Polarimetric Microscope Repository," 2021.

- [Online]. Available:
https://github.com/mloper23/BF_Polarimeter_Microscope/blob/main/README.md. [Accessed: 13-Sep-2021].
- [2] M. Bass, *Handbook of Optics, Volume I: Geometrical and Physical Optics, Polarized Light, Components and Instruments*. 1996.
- [3] V. V. Tuchin, "Polarized light interaction with tissues," *J. Biomed. Opt.*, vol. 21, no. 7, p. 071114, 2016.
- [4] E. Collett, *Field Guide to Polarization*, Volume FG0. Washington: SPIE Field Guides, 2005.
- [5] B. Bai, H. Wang, T. Liu, Y. Rivenson, J. FitzGerald, and A. Ozcan, "Pathological crystal imaging with single-shot computational polarized light microscopy," *Journal of Biophotonics*. 2020.
- [6] G. P. Agrawal, "Chapter 6. Polarization effects," in *Nonlinear Fiber Optics*, 2019th ed., E. Inc., Ed. 2019, pp. 189–244.
- [7] M. J. Lopera and C. Trujillo, "Linear diattenuation imaging of biological samples with digital lensless holographic microscopy," *Appl. Opt.*, vol. 61, no. 5, p. B77, Feb. 2022.
- [8] L. Trifonyuk *et al.*, "Differential Mueller matrix imaging of partially depolarizing optically anisotropic biological tissues," *Lasers Med. Sci.*, vol. 35, no. 4, pp. 877–891, Jun. 2020.
- [9] M. Dubreuil, F. Tissier, S. Rivet, and Y. Le Grand, "Linear diattenuation imaging of biological tissues with near infrared Mueller scanning microscopy," *Biomed. Opt. Express*, vol. 12, no. 1, p. 41, Jan. 2021.
- [10] I. L. Maksimova, V. V. Tuchin and L. P. Shubochkin, "Polarization features of eye's cornea," *Opt. Spectrosc. (USSR)*, 60 (4), 801–807 (1986). OPSUA3 0030-400X
- [11] A. Pabón, C. A. Trujillo, and M. J. Lopera, "Single-shot dual-wavelength Polarized Microscope to detect Malaria-infected Erythrocytes via birefringence response," *Conf. Lasers Electro-Optics (2021), Pap. JTu3A.16*, p. JTu3A.16, May 2021.
- [12] C. W. Pirnstill and G. L. Côté, "Malaria Diagnosis Using a Mobile Phone Polarized Microscope," *Sci. Rep.*, vol. 5, pp. 1–13, 2015.
- [13] E. Mahoney, J. Kun, M. Smieja, and Q. Fang, "Review—Point-of-Care Urinalysis with Emerging Sensing and Imaging Technologies," *J. Electrochem. Soc.*, vol. 167, no. 3, p. 037518, Jan. 2020.
- [14] M. Asselman, A. Verhulst, M. E. De Broe, and C. F. Verkoelen, "Calcium Oxalate Crystal Adherence to Hyaluronan-, Osteopontin-, and CD44-Expressing Injured/Regenerating Tubular Epithelial Cells in Rat Kidneys," *J. Am. Soc. Nephrol.*, vol. 14, no. 12, pp. 3155–3166, Dec. 2003.
- [15] J. W. Goodman, *Introduction to Fourier Optics*. Greenwood Village: Roberst & Company Publishers, 2005.
- [16] J. Rick Tu, "Ray Optics Simulation," 2016. [Online]. Available: <https://ricktu288.github.io/ray-optics/>. [Accessed: 13-Sep-2021].
- [17] R. Mehta *et al.*, "Wireless, Web-Based Interactive Control of Optical Coherence Tomography with Mobile Devices," *Transl. Vis. Sci. Technol.*, vol. 6, no. 1, pp. 5–5, Jan. 2017.
- [18] V. Singh, R. Dubey, P. K. Panigrahi, and K. Muralidhar, "An educational website on interferometry," *Proc. - 2012 IEEE Int. Conf. Technol. Enhanc. Educ. ICTEE 2012*, 2012.
- [19] E. Hecht, *Optics 4th edition*, vol. 1. 2001.
- [20] M. Born and E. Wolf, *Principles of Optics*, 7th ed. Cambridge, UK: Cambridge University Press, 2005.
- [21] "Dash Documentation & User Guide | Plotly." [Online]. Available: <https://dash.plotly.com/>. [Accessed: 28-Nov-2021].
- [22] Y. Yoo, Y. J. Seo, M. Huh, J. H. Yoo, K. H. Yun, and S. J. Kim, "Gout and coexisting pseudogout in the knee joint," *Knee Surgery, Sport. Traumatol. Arthrosc.*, vol. 19, no. 4, pp. 553–555, Apr. 2011.
- [23] Y. Zhang *et al.*, "Wide-field imaging of birefringent synovial fluid crystals using lens-free polarized microscopy for gout diagnosis OPEN," *Nat. Publ. Gr.*, 2016.
- [24] D. Ye *et al.*, "Preferred crystallographic orientation of cellulose in plant primary cell walls," *Nat. Commun.*, vol. 11, no. 1, p. 4720, Dec. 2020.
- [25] A. Van Eeckhout *et al.*, "Polarimetric imaging microscopy for advanced inspection of vegetal tissues," *Sci. Rep.*, vol. 11, no. 1, p. 3913, Dec. 2021.



- [26] M. J. Lopera, A. Pabón, and C. A. Trujillo, "Single-shot dual-wavelength Polarized Microscope to detect Malaria-infected Erythrocytes via birefringence response," *CLEO 2021 OSA 2021*, 2021.
- [27] W. Bishara *et al.*, "Handheld, lensless microscope identifies malaria parasites."

1. Introduction

The measurement of the different properties of light polarization can be related to structural information of microscopic samples by using polarimetric microscopes[2]. Among the information that can be retrieved from a polarimetric microscope are accounted the concentration and detection of a given substance [3], the detection of regions in the sample with a given molecular arrangement[4], and the detection of objects and features in the sample that cannot be resolved by traditional brightfield microscopes[5][6]. Different technologies involving polarimetric measurements in a microscope have been applied to biological samples[7]–[9]. Thanks to the latter, polarimetric microscopes have recently been used in biomedical applications; some of those include the examination of tissues as the eye cornea [10], the detection of malaria in red blood cells [11], [12], and the early diagnosis of gout disease [5] and other urinary diseases [13][14]. Despite their extensively reported use, these technologies do not have user interfaces open to the general academic community for the numerical processing of the information they provide. As a result, their use is restricted to laboratories and specialized research centers.

Numerical simulations are essential tools when developing an optical system[15]. These computer-based approaches complement the experimental setup by validating and predicting their behavior, helping to solve setbacks efficiently, and reducing development times and costs. Nonetheless, implementing numerical simulations of optical devices requires deep knowledge of optics fundamentals, which in many cases inhibits their applicability. Web applications have been developed to cope with this limitation by facilitating access to simulations in optics concerning ray tracing[16], optical coherence tomography[17], and interferometry[18], and many others. Among the advantages of web applications are i) their quick and easy access, ii) no local installations or updates are required, and iii) their compatibility with any internet-enabled device, such as cell phones.

This paper reports a web application for polarimetric and microscopic imaging for teaching and research purposes. The web application is divided into three layouts to simulate a polarimetric microscope, compute the dichroic response of samples from intensity images, and calculate the Stokes parameters of an illumination beam. The web application is validated using experimental samples of onion cells, red blood cells, and experimental microscope illuminations. The remainder of the paper is organized as follows. The fundamentals of a polarimetric microscope are presented in Section 2. The algorithms behind the simulators are explained in detail in section 3. The user interfaces and layouts that compose the web application are presented in section 4. The experimental validation of the polarimetric performance of the proposal is described in section 5. In section 6, the imaging performance of the simulated microscope is studied. The text finishes with conclusions.

2. Fundamentals of a polarimetric microscope

The fundamentals of a polarimetric microscope are provided in this section. First, the polarization response of the instrument is presented. Then, according to Fourier optics theory, the physical principles are introduced to describe the features of the imaging system.

2.a. Polarizing response of the instrument

When light interacts with a sample, be it a biological tissue, a cell culture, or an inorganic material, its polarization state changes according to the birefringent or dichroic behavior of some structures or regions of the sample under study. In this case, the sample acts as a linear system that modifies the polarization state of the impinging wavefront[3]. Thus, specific information about the sample can be retrieved by extracting i) the depolarization degree of the initially polarized light, ii) the transformation of its polarization state or iii) the polarized components in the scattered light[3]. Jones's calculus[2] is employed to model and simulate the behavior of coherent and polarized light interacting with a linear polarizing sample. According to this formalism, polarized light in a homogeneous isotropic non-attenuating medium is appropriately described as transversal waves and is represented via two perpendicular polarization components[19]. On the other hand, linear polarizing optical elements are described as 2x2 matrices. Following this formalism, our proposal is aimed to image and/or simulate low-depolarizing samples. The

resulting transformation of an arbitrary incident polarized beam after illuminating a lineal optical sample can be described as a system that relates the incident (input) and the scattered (output) components. Mathematically, this transformation can be expressed as shown in Equation (1).

$$\mathbf{E}_{output} = \begin{bmatrix} E_{ox} \\ E_{oy} \end{bmatrix} = \begin{bmatrix} J_{11} & J_{12} \\ J_{21} & J_{22} \end{bmatrix} \begin{bmatrix} E_{ix} \\ E_{iy} \end{bmatrix} \quad (1)$$

In Equation (1) $\begin{bmatrix} E_{ix} \\ E_{iy} \end{bmatrix}$ is the input Jones vector and it describes the polarization components of the incident light, J_{nn} are the complex elements of the Jones matrix representing the sample polarizing properties and $\begin{bmatrix} E_{ox} \\ E_{oy} \end{bmatrix}$ is the output Jones vector that describes the polarization components of the resulting wavefront. Figure 1 shows the normalized Jones and Stokes vectors for the degenerated polarization states of light.

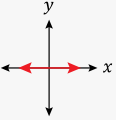
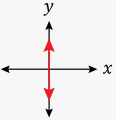
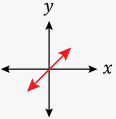
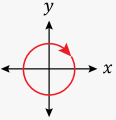
Polarization	Jones vector	Stokes vector	Representation
Horizontal	$\begin{bmatrix} 1 \\ 0 \end{bmatrix}$	$\begin{bmatrix} 1 \\ 1 \\ 0 \\ 0 \end{bmatrix}$	
Vertical	$\begin{bmatrix} 0 \\ 1 \end{bmatrix}$	$\begin{bmatrix} 1 \\ -1 \\ 0 \\ 0 \end{bmatrix}$	
Linear at 45° from x axis	$\frac{1}{\sqrt{2}} \begin{bmatrix} 1 \\ \pm 1 \end{bmatrix}$	$\begin{bmatrix} 1 \\ 0 \\ \pm 1 \\ 0 \end{bmatrix}$	
Right (+) [RCP] and left (-) [LCP] circular	$\frac{1}{\sqrt{2}} \begin{bmatrix} 1 \\ \pm i \end{bmatrix}$	$\begin{bmatrix} 1 \\ 0 \\ 0 \\ \pm 1 \end{bmatrix}$	

Figure 1. Normalized Jones and Stokes vector for the degenerated polarization states of light.

A coherent digital polarimetric microscope involves a monochromatic light source, a polarization states generator (PSG), the sample, a magnifying imaging system, a polarization stated analyzer (PSA), and a digital sensor. For simplicity, the light source in this system is a monochromatic plane wavefront whose wavelength is λ . The PSG and the PSA are optical arrays that produce all the degenerated polarization states; these arrays are composed of a linear polarizer followed by a quarter-wave plate. The magnifying imaging system comprises an infinity-corrected microscope objective (*MO*) and a tube lens (*TL*). Figure 2 illustrates the described monochromatic polarized microscope setup.

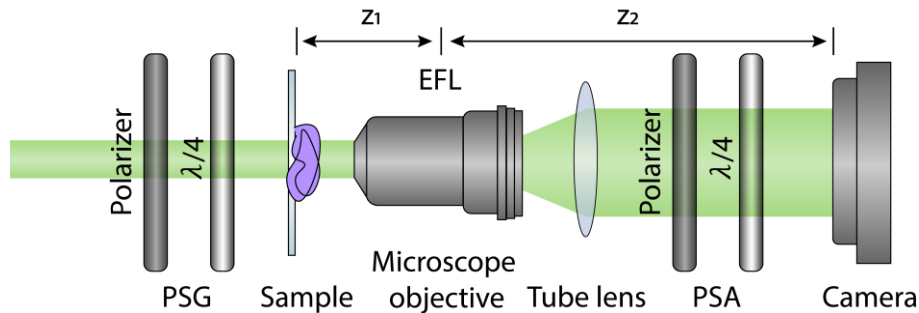


Figure 2. Monochromatic polarimetric microscope setup.

Considering that the PSA and PSG provide any degenerated polarization state, the Jones vector after the sample can be calculated using Equation (2).

$$E_{output} = PSA \cdot S \cdot PSG \cdot E_{input} = \begin{bmatrix} PSA_{11} & PSA_{12} \\ PSA_{21} & PSA_{22} \end{bmatrix} \begin{bmatrix} J_{11} & J_{12} \\ J_{21} & J_{22} \end{bmatrix} \begin{bmatrix} PSG_{11} & PSG_{12} \\ PSG_{21} & PSG_{22} \end{bmatrix} \begin{bmatrix} E_{ix} \\ E_{iy} \end{bmatrix} \quad (2)$$

In Equation (2), PSA_{nn} and PSG_{nn} are the components of the transfer matrix of each polarization element. In this model, it is assumed that the magnifying imaging system does not change the polarization state of light; the latter is based on the fact that the imaging system is composed of refracting elements that modify the shape of the impinging wavefront without introducing any retardance due to its characteristic optical isotropy[20]. Therefore, no polarization-state changing properties are presented for this system; thus, the polarization state of the incident beam established by the PSG and then modified by the sample is kept up to the PSA. The resulting intensity distribution is finally recorded by the digital sensor (CMOS or CCD camera).

2.b. Microscope imaging system

The magnified image produced by the microscope can be modeled by considering the MO and the TL as a single linear shift-invariant system in amplitude with a point spread function (PSF) as expressed in Equation (3). This expression is valid in those cases where the imaging system satisfies the lens equation *i.e.*, $\frac{1}{z_1} + \frac{1}{z_2} = \frac{1}{f}$; where f is the effective focal length of the system and z_1, z_2 , are the distances from the sample to the MO's pupil and from the MO's pupil to the image plane.

$$h(u, v; \xi, \eta) = \frac{1}{\lambda^2 z_1 z_2} e^{j \frac{k}{2z_2}(u^2+v^2)} e^{j \frac{k}{2z_1}(\xi^2+\eta^2)} \iint_{-\infty}^{\infty} P(x, y) e^{-jk(ux+vy)} dx dy \quad (3)$$

In Equation (3) u, v are the coordinates at the image plane or the sensor plane. ξ, η are the input coordinates at the sample plane and $P(x, y)$ is the entrance pupil of the system. Since the magnification of the system can be computed as $M = -\frac{z_2}{z_1}$, the geometrical-optics prediction of the image can be obtained according to Equation (4)

$$U_{image}(u, v) = \frac{1}{|M|} U_{object}\left(\frac{u}{M}, \frac{v}{M}\right) \quad (4)$$

The resulting complex field (Equation (5)) is given by the convolution between the geometrical-optics prediction of the image (Equation (4)) and the PSF of the imaging system (Equation (3)), which is the Fraunhofer diffraction pattern of the lens pupil [15].

$$U_{image}(u, v) = \iint_{-\infty}^{\infty} \frac{1}{|M|} U_{object}\left(\frac{\xi}{M}, \frac{\eta}{M}\right) h(u - \xi, v - \eta) d\xi d\eta \quad (5)$$

The transfer function of this linear system is defined as the Fourier transform of its PSF, $H(f_u, f_v) = \mathcal{F}\{h(u, v; \xi, \eta)\}$, therefore, the diffracted image can be obtained by multiplying the Fourier transform of the magnified geometrical image with the transfer function of the system

$$U_{image}(u, v) = \mathcal{F}^{-1} \left\{ \mathcal{F} \left\{ \frac{1}{|M|} U_{object}\left(\frac{\xi}{M}, \frac{\eta}{M}\right) \right\} H(u, v; \xi, \eta) \right\} \quad (6)$$

For a free-aberration (diffraction-limited) optical system, the output image is a scaled version of the object's intensity distribution at the sample plane. The following section presents the details of the discrete implementation of Equation (6) and its use in the simulation of a polarimetric microscope.

3. Polarimetric microscope algorithm

As described in section 2, a polarimetric microscope can be understood as two independent systems: a microscope and a polarimeter. The microscope's magnified image is modeled initially, and then the

polarimetric response of the sample is retrieved. To model the microscope's image, the magnified geometrical optics prediction of the sample $I_{GO}(u, v) = I(\frac{\xi}{M}, \frac{\eta}{M})$ is computed by performing straightforward cropping and interpolation of the input image $I(\xi, \eta)$. This procedure is shown in Figure 2.

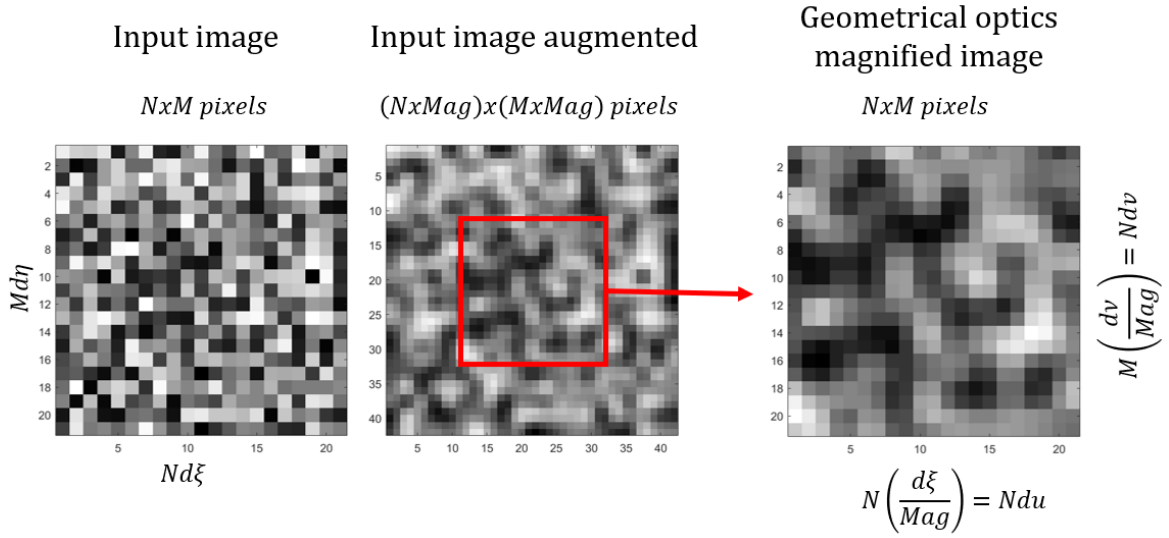


Figure 3. Interpolation procedure to obtain the geometrical-optics image from the input image. (Left) the input image, (center) the magnified image, and (right) the geometrical-optics prediction.

The input image $I(\xi, \eta)$ has $N \times M$ pixels (Left panel in Figure 2). This image is resampled to an image with an increased number of pixels in each dimension (Central panel in Figure 2). Then the geometrical-optics image is obtained by cropping the desired section of this new matrix (Right panel in Figure 3). The cropped image has the same number of pixels as the original image, but its pixel pitches du and dv are smaller than the original ones $d\xi$ and $d\eta$, specifically $\Delta u = \frac{d\xi}{Mag}$ and $dv = \frac{d\eta}{Mag}$.

To find the resulting image which considers the diffraction-related imaging effects, the convolution of the magnified geometrical optics and the PSF of the system must be calculated via the discrete version of equation (6). The transfer function of the system can be estimated by computing the following discrete expression

$$H[n\Delta f_u, m\Delta f_v] = \mathcal{F}\{h[n\Delta u, m\Delta v; p\Delta\xi, q\Delta\eta]\}$$

$$H[n\Delta f_u, m\Delta f_v] = \lambda^2 z_1 z_2 e^{j\frac{k}{2z_2}((n\Delta u)^2 + (m\Delta v)^2)} e^{j\frac{k}{2z_1}((p\Delta\xi)^2 + (q\Delta\eta)^2)} P[\lambda z_2 f_u, \lambda z_2 f_v] \quad (7)$$

In equation (7) $\Delta u, \Delta v$ and $\Delta\xi, \Delta\eta$ are the pixel sizes in the space domain for the output and input planes respectively, $P[\lambda z_2 f_u, \lambda z_2 f_v]$ is the pupil function of the lens, f_u and f_v are the frequency coordinates of the output plane. The microscope output image I_o is finally found by computing equation (8). This process is illustrated in Figure 5.

$$I_o[n\Delta u, m\Delta v] = \frac{1}{\lambda^2 z_1 z_2} e^{j\frac{k}{2z_2}((n\Delta u)^2 + (m\Delta v)^2)} e^{j\frac{k}{2z_1}((p\Delta\xi)^2 + (q\Delta\eta)^2)} \mathcal{F}^{-1}\{\mathcal{F}\{I_{GO}\}P[\lambda z_2 f_u, \lambda z_2 f_v]\} \quad (8)$$

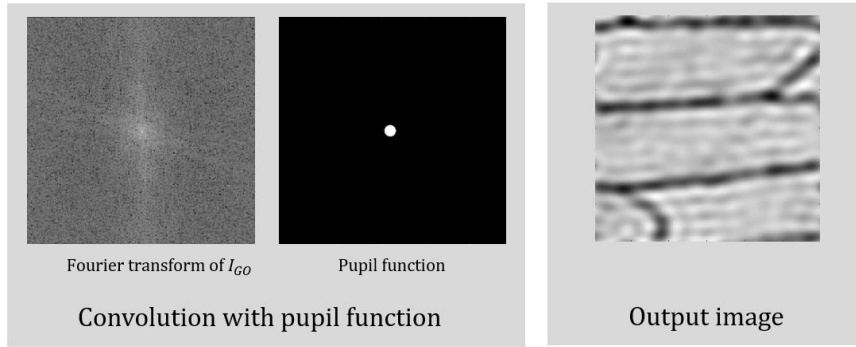


Figure 4. Procedure to compute the microscopic image of the sample. The Fourier transform of the geometrical prediction is convolved with the pupil function of the imaging system to produce the output image of the simulated microscope.

The second part of the algorithm uses the output image of the microscope as the input for the polarimeter. This algorithm assigns a Jones matrix to each pixel of the image I_o , creating a cell array as shown in Figure 5. The matrices are assigned using a thresholding procedure. The input image is normalized, and a threshold in range (0,1) is defined. For pixel values under the threshold, a given Jones matrix is assigned; on the other hand, for pixel values above this value, another Jones matrix is assigned. The same procedure can be performed with two thresholds values to assign three different Jones matrices to the sample. Once the Jones matrices of the sample are assigned J_{ij} , equation (2) can be applied to each i, j component of the cell array. Figure 5 presents the procedure mentioned above. Each pixel intensity P_{ij} is multiplied for a Jones matrix J_{ij} previously defined by the thresholding procedure. Then equation (2) is applied, and finally, the x and y polarization components of the resulting optical field are computed. The intensity of each pixel is yielded by computing the square modulus of the polarization vector.

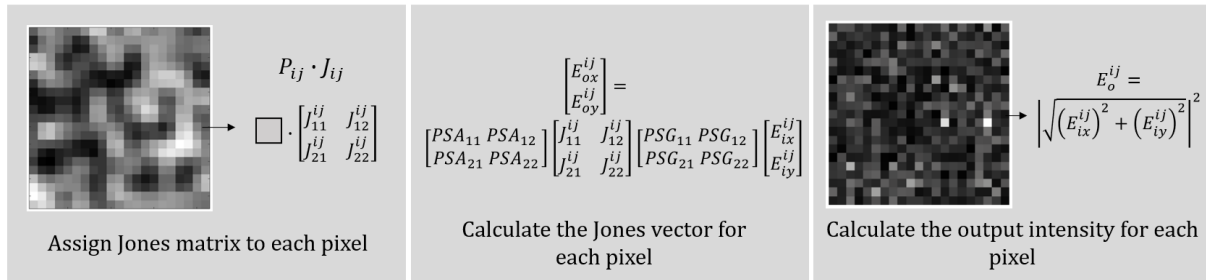


Figure 5. Step-by-step illustration of the simulated polarimeter algorithm.

4. User interface of the reported web application

Considering user-friendliness, a web application (web app) has been developed using the Python's framework Dash, which is based on Flask, Plotly and ReactJS[21]. The web app is rendered in a browser and consists of three different windows: Polarimetric Microscope, Stokes Vector, and Dichroic Response. Our web app can be accessed via the following repository [1].

4.a. Polarimetric microscope layout

The first window contains the polarimetric microscope simulation layout. This layout includes a window of theory description; below, the variable input section is available. The required inputs to this simulator are those expressed in equations (8) and (2). That is, the digital sample which can be a red-green-blue (RGB) or black-and-white (BW) image, the distances z_1 and z_2 , the wavelength λ , the numerical aperture (NA), the effective focal length (EFL), and desired magnification of the system. Although the layout simulation assumes that the system satisfies the lens equation, the user can modify z_1, z_2 and EFL parameters; therefore, when the lens equation is not satisfied, the resulting image will be fuzzy and defocused, as expected. Below the microscope's variables, the user finds the polarimeter parameters: the PSG and PSA matrices and the thresholding for the sample's Jones matrices. The pixel sizes are selected to meet the Nyquist-Shannon criterion [15] automatically. Finally, the user can visualize the algorithm's outputs, which are the magnified and polarimetric response images. The user can download these images for further

processing. This layout is aimed to provide a teaching tool that allows understanding how different polarizing properties of samples will yield different polarimetric measurements in an actual polarimetric microscope. In our proposal, the polarizing properties of the samples are controlled by a thresholding procedure to assign a given Jones matrix to every point of the input image.

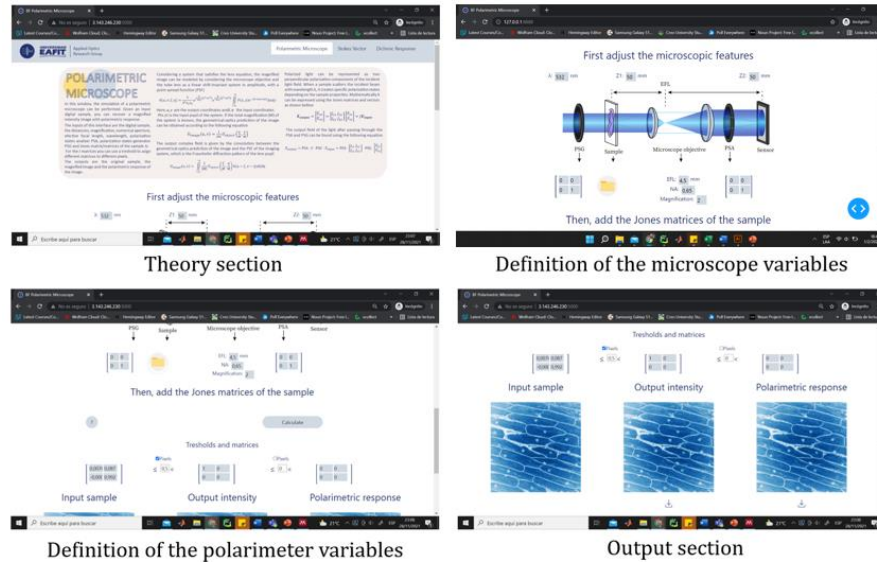


Figure 6. Screenshots of the polarimetric microscope layout.

4.b. Stokes vector layout

Another necessary formalism used when working with the polarization of light are the Stokes parameters [4]. It is a convenient alternative to describing incoherent or partially polarized light. Mathematically, the parameters are found by manipulating the polarization ellipse formula [19]. The parameters are often combined into a 4-entries vector known as the Stokes vector. Unlike the polarimetric microscope layout, the Stokes vector formalism allows the retrieval of experimental results involving partially polarized illumination and/or depolarizing samples.

With the idea to process data (either coherent or incoherent) carrying polarimetric information of experimental samples, this layout is provided to compute the Stokes vector, the degree of polarization (DOP), the degree of linear polarization (DOLP), the degree of circular polarization (DOCP) and the two main angles of the polarization ellipse of a light beam. To do this, six images must be acquired, either in an experimental polarimetric setup or in the fully polarized polarimetric microscope simulator layout (described in section 4a). The required images are:

- h : P_0° image acquired with a horizontal polarizer as $PSA = \begin{bmatrix} 1 & 0 \\ 0 & 0 \end{bmatrix}$
- v : P_{90}° image acquired with a vertical polarizer as $PSA = \begin{bmatrix} 0 & 0 \\ 0 & 1 \end{bmatrix}$
- p : P_{45}° image acquired with a linear polarizer with transmission axis at 45° as $PSA = \frac{1}{2} \begin{bmatrix} 1 & 1 \\ 1 & 1 \end{bmatrix}$
- n : P_{-45}° image acquired with a linear polarizer with transmission axis as $PSA = \frac{1}{2} \begin{bmatrix} 1 & -1 \\ -1 & 1 \end{bmatrix}$
- r : P_{rcp} image acquired with a linear polarizer with transmission axis at 45° followed by a quarter-wave plate as $PSA = \frac{1}{2} \begin{bmatrix} 1 & i \\ -i & 1 \end{bmatrix}$
- l : P_{lcp} image acquired with a linear polarizer with transmission axis at -45° followed by a quarter-wave plate as $PSA = \frac{1}{2} \begin{bmatrix} 1 & -i \\ i & 1 \end{bmatrix}$

Once these images are input to the layout, the Stokes vector of the resulting light beam is calculated via equation (8) [6].

$$s = \begin{bmatrix} s_0 \\ s_1 \\ s_2 \\ s_3 \end{bmatrix} = \begin{bmatrix} P_{0^\circ} + P_{90^\circ} \\ P_{0^\circ} - P_{90^\circ} \\ P_{45^\circ} - P_{-45^\circ} \\ P_{rcp} - P_{lcp} \end{bmatrix} = \begin{bmatrix} h + v \\ h - v \\ p - n \\ r - l \end{bmatrix} \quad (9)$$

From the Stokes parameters, the different types of degree of polarization of the studied light beam can be directly calculated using the following expressions [19]:

- Degree of polarization, $DOP = \frac{\sqrt{s_1^2 + s_2^2 + s_3^2}}{s_0}$
- Degree of linear polarization, $DOLP = \frac{\sqrt{s_1^2 + s_2^2}}{s_0}$
- Degree of circular polarization, $DOCP = \frac{|s_3|}{s_0}$
- Angle of polarization 1, $2\psi = \tan^{-1}\left(\frac{s_2}{s_1}\right)$
- Angle of polarization 2, $2\chi = \tan^{-1}\left(\frac{s_3}{\sqrt{s_1^2 + s_2^2}}\right)$

For a deep analysis of the resultant angles of polarization, we encourage the reader to review [4].

In this layout, the user can visualize the average Stokes vector and the polarization degrees of the studied light beam. Also, these parameters can be evaluated for each pixel of the resulting field of view. In the *selected* panel, these values for individual pixels are displayed. The functionality of the Stokes vector layout constitutes a valuable tool when retrieving polarimetric properties of experimental samples quantitatively. The retrieved measurements by this layout can be employed to detect substances or specimens in biomedical samples, which can be further used in the diagnostic procedure of different diseases [[5], [22], [23]].

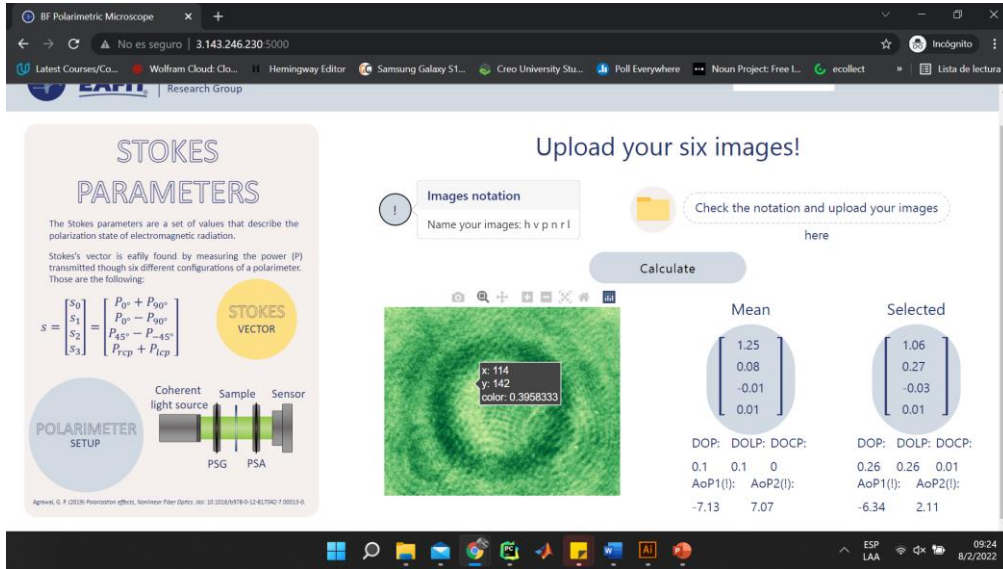


Figure 7. Screenshot of the Stokes vector layout.

4.c. Dichroic response layout

Another important measurable polarimetric property is the linear dichroism of the linear diattenuation response of a sample. Dichroism refers to the selective absorption of one of the two orthogonal components of a beam [19]. This layout allows the calculation of the dichroic response of a sample given two experimental or synthetic (subsection 4a) images as an input (Figure 8). The required images are:

- $I_{par} = I_{\parallel}$ Image recorded with the PSA parallel to PSG.
- $I_{per} = I_{\perp}$ Image recorded with the PSA perpendicular to PSG.

The dichroic response is calculated using the expression (9)[19].

$$d(\lambda) = \frac{I_{\parallel} - I_{\perp}}{I_{\parallel} + I_{\perp}} \quad (10)$$

As the dichroism depends on the wavelength, the user can specify whether the BW or RGB input images are used. If an RGB image is selected, a channel split is performed, and the dichroism is calculated independently for each channel. As for the Stokes vector layout, the Dicroich response layout provides a preprocessing method to detect substances or specimens in the samples that can be further used in the diagnosis procedure. In particular, in this layout, the latter can be done by requiring only two sample acquisitions, which diminishes the overall retrieving of information procedures in biomedical applications.

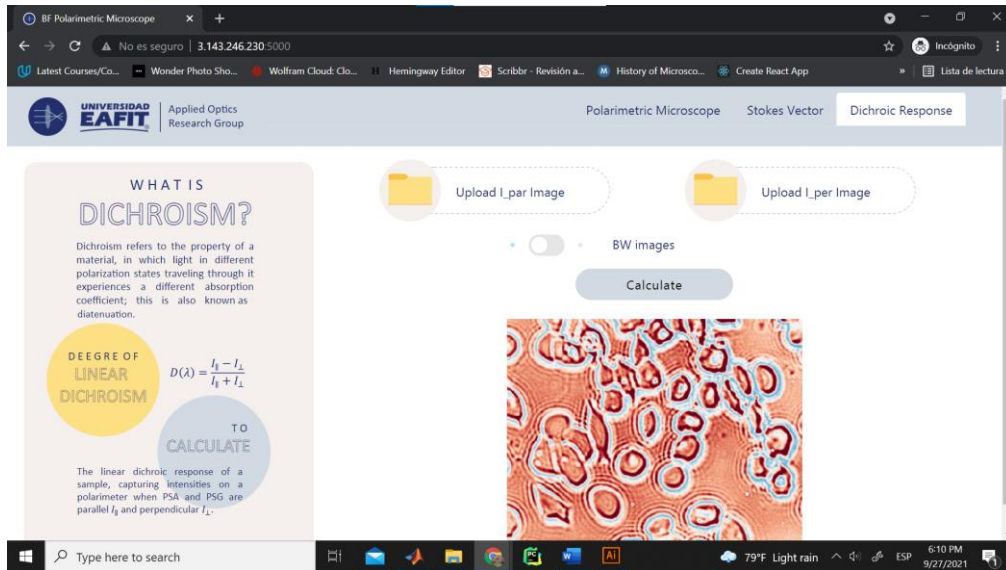


Figure 8. Screenshot of the Dichroic response layout.

5. Validation of the polarimetric performance of the web application.

Initially, an experimental setup as the one depicted in Figure 1 has been implemented to validate the results obtained with the polarimetric microscope layout. The illumination source in this setup is a 533 nm Cobolt Solid State laser. The collimated beam impinges the PSG composed of a linear polarizer and a quarter-wave plate at 533nm. Then the polarized light illuminates the sample, and a 40X/0.65 microscope objective (MO) collects the scattered wavefront to produce a focused image of the specimens at the camera sensor plane employing a 300mm focal length tube lens; this configuration provides a 66X total magnification. A PSG comprising a linear polarizer and a quarter-wave plate is placed between the tube lens and the digital sensor. The digital sensor is a Thorlabs CMOS color camera with 1024x1280 square pixels, each of 3.6μm pitch.

The first evaluated biological sample comprises epidermis onion cells. Figure 9 shows the intensities recorded for this biological sample when the PSG is a horizontal polarizer and the PSA is a linear polarizer parallel to the PSG (a) and when the PSA is perpendicular to the PSG (b); in this figure, the intensities computed via the polarimetric microscope layout under the same conditions are also depicted, panels (c) and (d). An arbitrary thresholding method has been implemented to assign the Jones matrices to the different regions of this experimental sample to produce these simulated intensities using the polarimetric microscope layout. For this particular experimental sample, it is well known that the cell wall of these specimens is composed of cellulose fiber, so a dichroic response is present in these parts of the specimen. The latter implies that a lower gray level is retrieved when these parts of the samples are imaged via brightfield microscopy; therefore, we related the gray level of each pixel to its pointwise assigned Jones matrix for the overall sample. Although this procedure will not yield highly accurate results, it is a first step in the students' understanding of the Jones calculus in their optical modeling training. In panels (a) and (b), one can appreciate that the cell wall induces optical activity in the sample since it presents maximum

intensities when the PSG and PSA polarizers are crossed, while the internal part of the cells behaves linearly with respect to the PSA transmission axis. The thresholding procedure identifies the pixel intensity values of the image in which the cell wall is located; for these values, the Jones matrix of a linear polarizer whose transmission axis is 85° has been assigned. On the other hand, a Jones matrix of a linear polarizer whose transmission axis is parallel to the PSG has been assigned to the inner part of the cells.

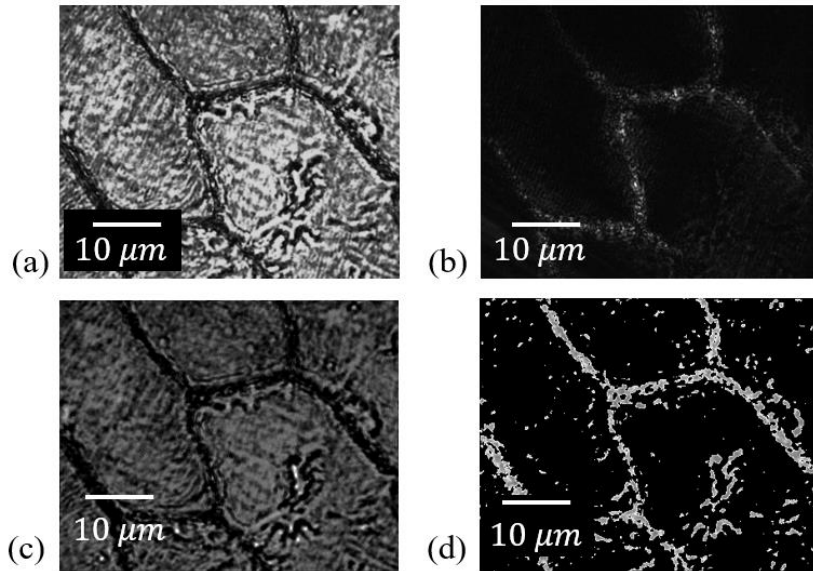


Figure 9. Recovered intensities by the experimental and simulated polarimetric microscopes for a biological sample of epidermic onion cells. (a) Experimental intensity recorded when the PSA and PSG are parallel. (b) Experimental intensity recorded when the PSA and PSG are perpendicular. (c) Simulated intensity by the proposed polarimetric microscope layout computed when the PSA and PSG are parallel. (d) Simulated intensity by the proposed polarimetric microscope layout computed when the PSA and PSG are perpendicular.

To explain the results depicted in Figure 9, one must analyze the two different cases separately. In the case where the transmission angles of the PSG and PSA are parallel (Figure 9 (a)), the regions of the biological sample with high transmittance (in effect, the cell themselves) do not induce any change in the polarization of the beam as the intensity of the transmitted light remains unchanged. Otherwise, for the low-transmission regions, the sample behaves as a linear polarizer whose transmission angle is perpendicular to the PSA as the intensity in this portion of the sample decays to zero. The same analysis applies when the PSG and PSA transmission angles are perpendicular (Figure 9(b)). In this case, the high-transmission regions of the sample behave as linear polarizers whose transmission angles are perpendicular to the PSG's, hence parallel to the PSA's. The low-transmission regions of the sample behave conversely. Figure 9(c) and Figure 9(d) show that the proposed polarimetric microscope layout also accounts for the latter polarimetric behavior of the sample. Although panels (a) and (c) are in remarkable agreement, the opposite occurs for panels (b) and (d). The latter can be explained considering that a two-step thresholding method has been implemented. A more developed procedure to fine-tune the polarimetric behavior of this sample can be implemented; nonetheless, the proposed procedure is validated as a proof-of-concept of the proposed polarimetric microscope layout.

To find the dichroic response for the epidermic onion cells sample, the Dichroic response layout is employed for both the experimental and simulated intensity images (Figure 10). As can be observed in the dichroic response computed from the experimental images (Figure 10(a)), the cell wall of these specimens presents negative linear dichroism, in contrast to the inner structures of the cells, which present positive dichroic response. These results agree with the theoretical expectation considering that the cell wall is composed of cellulose fiber, polysaccharides, and proteins[24]; since these compounds, particularly the cellulose fiber, are composed of well-aligned molecules, a strong dichroic response is expected for these parts of the specimen due to their intrinsic anisotropic absorption[25]. As for the dichroic response obtained with the simulated intensities, the similarity of the results for the inner part of the cells and the cell walls is also evidenced. As explained before, a fine-tuned thresholding procedure could lead to more reliable results.

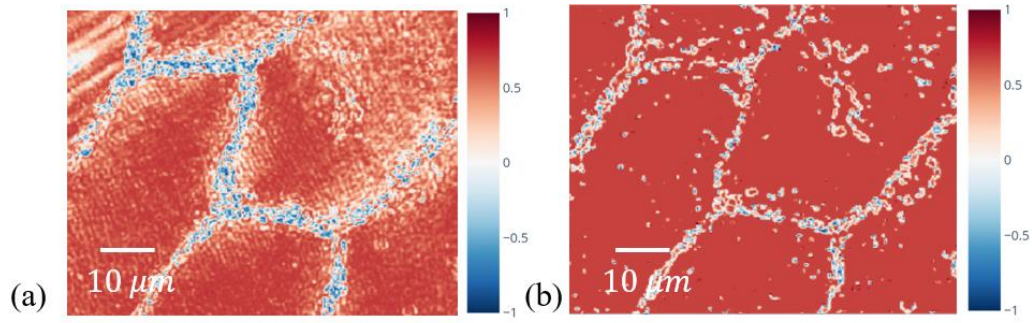


Figure 10. Dichroic response for onion cells using the Dichroic response layout. (a) Dichroic response from experimental intensities and (b) Dichroic response from simulated intensities.

To further validate the proposed web application, intensity images of experimental samples of red blood cells infected with the *Plasmodium* parasite (Malaria disease) have been recorded with the polarimetric microscope optical setup previously described. The images have been processed with the Dichroic response layout. It has been shown that this parasite presents negative linear dichroism when imaged in a polarimetric microscope with laser light at 532nm wavelength[26], [27]. Figure 11(a) presents the experimental linear dichroic response of this sample. The simulated dichroic response of the sample is presented in Figure 11(b). As can be seen in these results, the contrast of the parasite is higher for the dichroic response when compared to the regular intensity recording. This result confirms that a polarimetric microscope is a powerful device for diagnosing diseases such as malaria and that our proposed Dichroic response layout paves the way to this purpose.

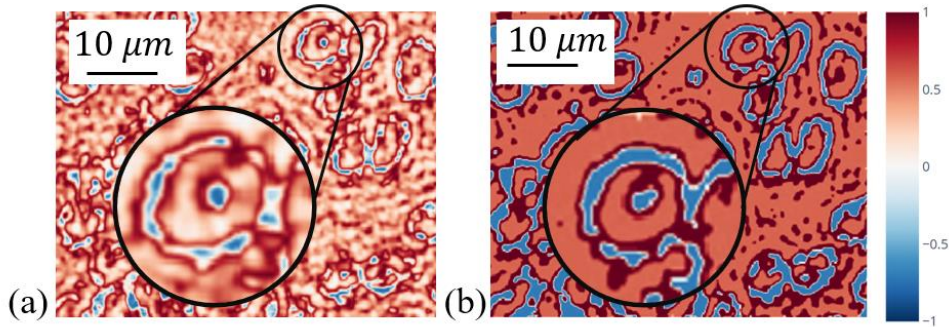


Figure 11. (a) Experimental result of the dichroic response of the malaria-infected RBCs. (b) Simulated result of the dichroic response of the malaria-infected RBCs.

Finally, as a validation of the Stokes parameters layout, the six required images described in section 4.b. have been acquired using the polarimetric microscope previously described. The PSG has been fixed as a linear polarizer whose transmission angle is 45° with respect to the vertical axis. The Stokes parameters of a light beam with linear polarization at 45° is $S_{45} = [1 \ 0 \ 1 \ 0]$ [19]. As can be appreciated in Figure 12, the calculated Stokes vector in this case is $[0.9 \ -0.03 \ 0.9 \ 0.02]$, which leads to a total error of 6.25% when compared to the theoretical results. This error can be explained by unstable experimental conditions during recording the six images; nevertheless, these results validate the proposed Stokes parameters layout. Moreover, the degree of linear polarization of the input beam is 100%, as depicted in Figure 12, which further validates this layout.

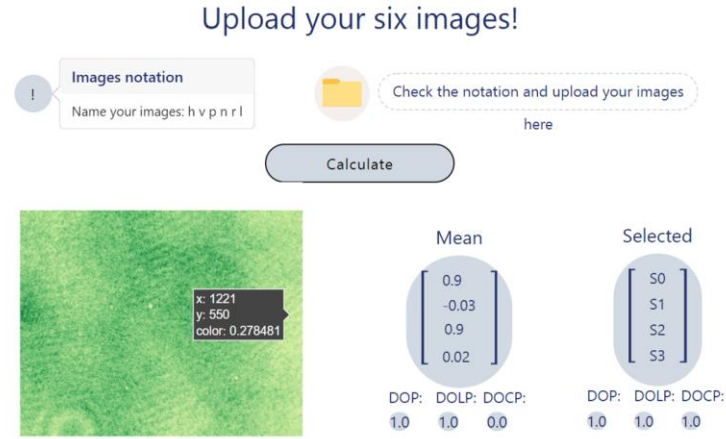


Figure 12. Screenshot of the Stokes layout with the Stokes calculation of a light beam with 45° linear polarization.

6. Imaging performance of the simulated microscope.

Linear systems can be described as "black boxes" with an entrance pupil that limits the information that enters the system and an exit pupil that modifies the amplitude and phase of the propagating wavefronts. For coherent imaging, the amplitude mapping is space-invariant [15], and transfer-function concepts can be applied to measure the performance of microscopic imaging systems. The transfer function for coherent illumination, which is called the Amplitude Transfer Function (ATF), is defined as the Fourier transform of the PSF of the system (Equation (3)). The ATF is a scaled version of the pupil function, as expressed in equation (10).

$$H(f_u, f_v) = F\{h(u - \xi, v - \eta)\} = A \lambda z_2 P(\lambda z_2 f_u, \lambda z_2 f_v) \quad (11)$$

The numerical aperture (NA) of the first lens (commonly the microscope objective) limits light entrance on a microscope. Therefore, in this analysis, the lens's NA is considered the entrance pupil of the system. In this case, a 40x/0.65 MO has been considered: its NA is 0.65, and its working distance is 0.6mm. The radius of the pupil is approximately 3 mm, according to the manufacturer. To compute the cutoff frequency of the system, a green laser $\lambda = 532.8 \text{ nm}$ has been selected as the light source and the reconstruction distance of the microscope $z_2 = 2 \text{ mm}$. The theoretical cutoff frequency for this system is $f_{oc} = \frac{w}{\lambda z_2} = 2.7 \frac{\text{cycles}}{\mu\text{m}}$. According to these results, the lateral resolution $\delta_{x,y} = \frac{1}{f_o}$ for this coherent system is $0.4 \mu\text{m}$.

Two Dirac deltas have been placed at the input plane of the Polarimetric microscope layout to validate this result. Since in this experiment, the pixel pitch is $0.4 \mu\text{m}$, and knowing that the area of the input plane is 1 mm^2 , then the resulting image is 2500×2500 pixels. Figure 13 (a) presents the input and output planes, when the separation between the Dirac deltas' is $1.2 \mu\text{m}$. One can observe in the output plane that both dots are properly imaged (Figure 13 (b)). In Figure 13 (c), the Dirac deltas are separated $0.4 \mu\text{m}$, which is the theoretical lateral resolution. For this case, both dots are still resolvable (Figure 13 (d)), but a third lobe appears between the objects; this artifact avoids proper imaging of these point objects, as theoretically expected. This result validates the imaging performance of the proposed web app concerning the minimal achievable lateral resolution of the resulting images.

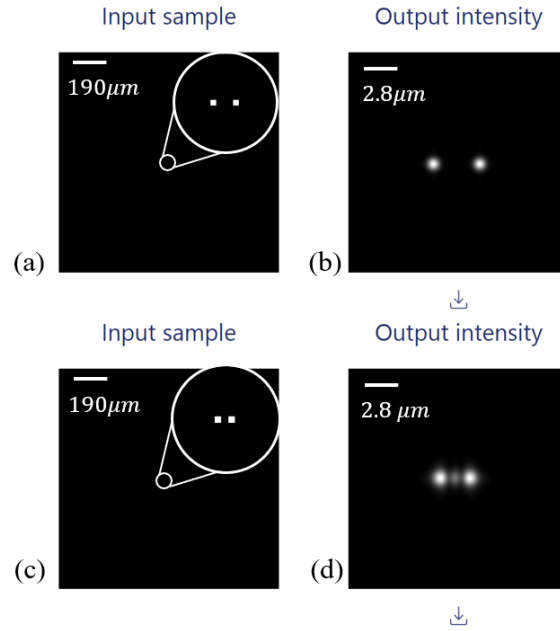


Figure 13. Simulated results by the Polarimetric microscope layout for two Dirac deltas when the imaging system yields a theoretical 0.4μm lateral resolution. (a) For the input plane, the distance between objects is 1.2μm. (b) Simulated results by the Polarimetric microscope layout when the input is panel(a). (c) Input plane when the distance between objects is 0.4μm. (d) Simulated results by the Polarimetric microscope layout when the input is panel (c).

As a final experiment, we proposed to simulate an aberration that can be easily present in the physical system: the focusing error. For this simulation, we have placed at the input plane of the layout a Spoke target image. The parameters used in the simulation are:

- $z_1 = 50mm$
- $z_2 = 50mm$ and $55mm$
- $\lambda = 532nm$
- $NA = 0.65$
- $EFL = 4.5mm$
- $PSG = PSA = \begin{bmatrix} 1 & 0 \\ 0 & 0 \end{bmatrix}$
- Sample $\begin{bmatrix} 1 & 0 \\ 0 & 0 \end{bmatrix}$

The obtained output intensity image for this experiment is presented in Figure 14(a) when the system is focused. This image is an exact zoomed area of the spoked target; it can be noticed that the modulation of the fringes is lower (the expected white lines are actually gray) as expected. Otherwise, Figure 14 (b) shows the output plane when the system is defocused by 5 mm. For this case, the modulation of the fringes presents the characteristic contrast reversion as the frequency increases [15]. As can be seen in the results by the polarimetric microscope layout concerning simulated lateral resolution and defocusing of the imaging system, a high agreement between the simulated and theoretical results is achieved. The latter results and those previously reported for the polarimetric layouts of the web application confirm its validity for microscopic and polarimetric imaging of biological samples.

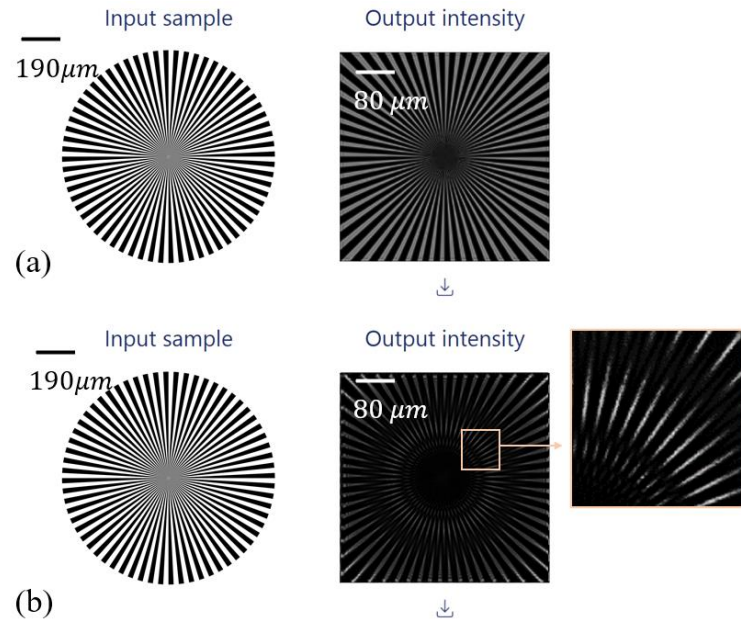


Figure 14. Focusing error aberration simulated with the polarimetric microscope layout of the proposed web application. (a) Screenshot of the input and output intensities from the layout when the Spoke target is at a focus distance. (b) Screenshot of the input and output intensities from the web application when the Spoke target is 5mm out of focus.

7. Conclusions

The mathematical modeling and simulation of a polarimetric microscope have been reported. Using this simulation, a Dash® web application (web app) has been implemented. This web app includes three windows: i) a polarimetric microscope simulator layout, ii) a dichroic response layout, and iii) a Stokes vector calculation layout. As for the polarimetric microscope layout, an algorithm to simulate this optical system provides the polarimetric response of a sample given the following inputs: an image with the information of the microscope specimen, the linear polarization state of the polarization states analyzer (PSA), and that of the polarization states generator (PSG), the magnification of the imaging system, the numerical aperture of the microscope objective and the object and image distances (z_1, z_2). The dichroic response layout, in turn, provides the dichroic response of the imaged specimen by inputting the intensity images obtained with an experimental or simulated polarimetric microscope when the PSG and PSA are both parallel and perpendicular. Finally, the Stokes vector layout outputs the pointwise and overall average polarization state of an illumination light beam, providing six intensity images at different configurations of two polarizing elements.

To validate the polarimetric results yielded by our web app, a brightfield polarimetric microscope based on a 40x/0.65 microscope objective has been experimentally implemented. Initially, for an experimental biological sample of onion cells, the typical dichroic response has been successfully obtained with experimental and simulated results. To further validate the proposed web app and potentialize the early diagnosis of malaria, a sample of red blood cells infected with the *Plasmodium Falciparum* parasite has also been processed. The experimental and simulated results show that a polarimetric microscope is a powerful tool for early diagnostics of the disease, since this parasite presents a strong negative dichroic response that eases its detection. Our polarimetric microscope layout yielded some differences between the experimental results and the simulated results: the experimental instrument leads to soft changes between the different regions of the specimens while the simulation involves a two-step thresholding method. A more developed procedure to fine-tune the polarimetric behavior of this sample can be implemented; nonetheless, the proposed procedure is validated a proof-of-concept of the proposed polarimetric microscope layout.

To validate the proper imaging performance of the simulated microscope, a validation of its lateral resolution and the possibility to correctly image out-of-focus objects has also been performed using our web app. First, a microscope with a theoretical 0.4 μm lateral resolution has been successfully simulated using the polarimetric microscope layout. In this simulation, images of two points separated by distances equal to and larger than the aforementioned lateral resolution have been input into the layout. The objects are properly resolved when their separation is larger than 0.4 μm. On the other hand, the system cannot

resolve these objects correctly when the separation of the objects is equal to $0.4\mu m$, which confirms the theoretical expectation. As for the focusing error aberration, a spoke target has been used as an input sample, obtaining gradual contrast attenuation and contrast reversals as the spatial frequency of the sample increases; these results are in total agreement with the theoretical predictions [15]. Considering the latter validation results, the ease of use, and its cross-platform portability, our web application is a valuable tool for different teaching and research applications in the field of microscopy and polarimetry of biological samples.

Acknowledgements

The authors thank PhD. Adriana Pabón-Vidal from Universidad de Antioquia for the preparation of the malaria-infected erythrocytes sample.

Optics Letters

Holographic point source for digital lensless holographic microscopy

MARIA J. LOPERA^{1,2}  AND CARLOS TRUJILLO^{1,3} 

¹Applied Optics Group, Physical Sciences Department, School of Applied Science and Engineering, Universidad EAFIT, Medellín, Colombia

²e-mail: mloper23@eafit.edu.co

³e-mail: catrujilla@eafit.edu.co

Received 23 March 2022; revised 5 May 2022; accepted 5 May 2022; posted 6 May 2022; published 26 May 2022

A holographic point source (HPS) developed for digital lensless holographic microscopy (HPS-DLHM) is presented. The HPS is an off-axis phase transmission hologram of an experimental micrometer pinhole recorded on a photopolymer holographic film. An amplitude division interferometer, adjusted to operate at maximum diffraction efficiency, has been employed to record the hologram. The results of HPS-DLHM have been contrasted with the results obtained via conventional DLHM, and the two techniques were found to give similar measurements. Compared with conventional pinhole-based DLHM illumination, our cost-effective proposal provides increased mechanical stability, the possibility of wider spherical illumination cones, and shorter reconstruction distances. These superior features pave the way to applying this quantitative phase imaging (QPI) technique in biomedical and telemedicine applications. The imaging capabilities of our HPS-DLHM proposal have been tested by using an intricate sample of a honeybee leg, a low-absorption sample of epithelial cheek cells, a 1951 USAF test target, and smeared human erythrocytes. © 2022 Optica Publishing Group

<https://doi.org/10.1364/OL.459146>

Lensless microscopy comprises computational imaging techniques that were developed to overcome disadvantages of conventional digital holographic microscopy, such as the need to implement bulky interferometric setups, the need for lenses in image magnification, and its high costs [1]. Since technological advances in computation have led to powerful, cost-effective, and portable solutions in recent decades [2], computational lensless microscopy techniques have been proposed that use inexpensive and straightforward implementations [3]: a divergent spherical-wavefront illumination source and a digital camera are the hardware needed. Although different modalities of lensless microscopy have been reported, a clear distinction can be made regarding the sample-to-sensor distance [4]. In on-chip microscopy [5], where the sample is close to the camera sensor, outstanding imaging performance is attained by using computationally demanding super-resolution techniques, learning-based approaches, or complex multiple-shot recording procedures [6–8]. The second modality is digital lensless holographic microscopy (DLHM) [9]. In this technique, the

sample's diffraction pattern, magnified during its propagation to the camera, allows the numerical retrieval of information about microscopic samples. As opposed to on-chip microscopy, in single-shot DLHM, the lateral resolution is dictated by the geometry of the optical imaging system [9]; that is, the sensor's size and the light cone generated by the point source.

In DLHM, wider illumination cones and shorter source-to-sample distances are desired to achieve high numerical apertures and large image magnifications [9]. The conventional method that is used to meet these conditions is based on micrometer pinholes [9]. The divergence of the illumination cone obtained by this method depends on the focal distance of the microscope objective used to focus the illumination wavefront and the pinhole size. The main drawbacks of this pinhole-based illumination approach are its challenging optical alignment, the lack of mechanical stability for in-field applications, the cost of the elements involved, and the restriction that the optical mounts impose for the sample to come into contact with the pinholes. Further developments in point sources for DLHM have been reported, such as the use of LED [10] and SLED [11] sources, pulsed laser radiation [12], illumination through GRIN lenses [13] or fiber optics [14], or the use of an electrically tunable lens [15]. Although these proposals reportedly provide good performance, they still have significant drawbacks: they involve bulky and expensive hardware, are difficult to align, or both. Proposals involving point sources that provide larger numerical apertures, shorter source-to-sample distances, and increased mechanical stability without adding complexity to the technique are still needed.

This Letter reports a holographic point source (HPS) for digital lensless holographic microscopy (HPS-DLHM). Holographic optical elements (HOE) are lightweight, thin, planar surfaces that base their operation on efficiently diffracting an impinging wavefront through microstructure profiles [16,17]. Various types of off-the-shelf HOEs are provided by different manufacturers [18]. As opposed to lenses, the light transmitted by a HOE can be reshaped to almost any desired form depending upon the recorded interference pattern, driving interesting applications of these optical elements in diverse fields [19]. Notwithstanding the latter advantages of HOEs, to the authors' best knowledge, these elements have not been proposed as point sources for DLHM. In the present work, an experimental micrometer pinhole has been recorded on a photopolymer

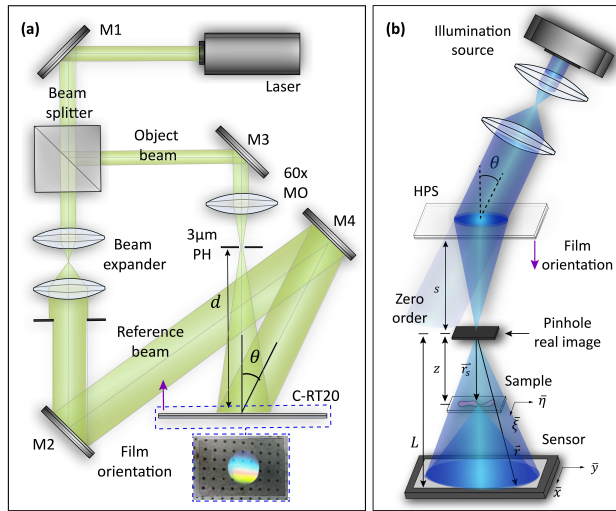


Fig. 1. (a) Illustration of the HPS recording setup. Photograph of the recorded HPS (dotted blue line). (b) Illustration of the HPS-DLHM setup.

holographic film using an amplitude division interferometer adjusted to output the maximum optical power efficiency. Once the HPS had been recorded, it was later illuminated to produce a holographic image of the micrometer pinhole, hence, the required spherical illumination in DLHM.

The off-axis amplitude division interferometer depicted in Fig. 1(a) has been used to record the transmission hologram of a micrometer point source. A 532 nm Cobolt laser is the illumination source of the system, and a cost-effective C-RT20 photopolymer holographic film from Litholo [20] is employed. A non-polarizing beam-splitter cube divides the incident beam into the object and reference wavefronts. The reference wavefront spot is expanded using a beam-expanding stage comprising two positive lenses in an afocal configuration. The reference wavefront then impinges over the holographic film at a tilting angle θ after being reflected by mirrors M2 and M3. In the other arm of the interferometer, the object wavefront is focused by a 60×0.85 Newport microscopy objective lens into an aluminum foil pinhole 3 μm in diameter. Assuming accurate alignment, this configuration assures the highly spatially coherent spherical illumination required in conventional DLHM [9]. Finally, the reference and object wavefronts interfere at the holographic film to record the interferogram carrying the information about the experimental point source.

The recording parameters, such as the exposure (30 mJ/cm^2), the optical power of the reference (0.25 mW) and object (0.20 mW) wavefronts, the total optical power (0.45 mW) illuminating the film, the exposure time (67 s), and the ratio of the reference to the object wavefront intensities (~ 1) of the HPS have been adjusted according to the manufacturer's density curve for the employed holographic film to yield the maximum diffraction efficiency [20]. The reference wavefront tilting angle has been set to consider the acceptable angle range of the holographic film illumination. The optical power efficiency of the first diffracted order of the HPS (the actual optical power employed to illuminate the sample) reaches 52% when the manufacturer's optimal recording parameters are met [20]. Once the HPS has been recorded, it must be illuminated to form a real image of the micrometer point source, as illustrated in Fig. 1(b). As depicted

in that figure, the orientation of the transmission hologram must be changed to generate the required spherical illumination wavefront in DLHM (see the purple arrows indicating the orientation of the holographic film in both panels of Fig. 1). The illumination light must impinge at θ to guarantee maximum diffraction efficiency.

An interesting feature of any HOE is that these elements can be reconstructed using an illumination wavelength λ_I that is different from that used during the holographic recording (λ_R). In this case, the location of the pinhole real image and the divergence of the resulting spherical wavefront will depend on the aforementioned wavelengths. To study the dependency of the angle θ_I of the resulting spherical illumination cone on different optical and geometrical factors, physical modeling of the HPS functioning has been performed; the procedure is summarized in the following steps. (i) First, the experimental pinhole (a circular aperture of diameter a) is illuminated by a converging spherical wavefront and then propagated to the holographic film plane, where it is superimposed with a tilted plane reference wavefront to yield the interference pattern at the holographic film plane such that $HPS(\vec{r}_h) \sim (1/\lambda_R k_R a \vec{r}_h) J_1(k_R a \vec{r}_h / 2d)$. In this expression, \vec{r}_h is a vector denoting a position at the HPS plane; $k_R = 2\pi/\lambda_R$, d is the distance between the experimental pinhole location and the holographic film, and $J_1(*)$ stands for the Bessel function of the first kind and first order. (ii) This interference pattern is illuminated with a conjugate reference wavefront and then propagated to a distance s again to obtain the intensity distribution of the focused real image of the pinhole $\text{circ}(dk_I 2\vec{r}_r / sk_R a)$; in this expression, $k_I = 2\pi/\lambda_I$ and \vec{r}_r is a vector denoting a position in the real image plane. Considering that the latter intensity distribution is that of a circular aperture with diameter $\phi = s\lambda_I a / d\lambda_R$, then when $\lambda_I = \lambda_R$, s equals d and $\phi = a$. On the other hand, when $\lambda_I > \lambda_R$, $\phi < a$, since $s < d$. (iii) Finally, to obtain an expression for θ_I , the radius of the resulting Airy disk of the real image of the pinhole at a reconstruction distance z , $r_{Ai} \approx 1.22z\lambda_I/\phi$, is considered. Then, expressing for the angle of the resulting illumination cone θ_I , Eq. (1) is derived:

$$\theta_I = \tan^{-1}\left(\frac{1.22\lambda_I}{a\lambda_I s / d\lambda_R}\right) = \tan^{-1}\left(\frac{1.22\lambda_R}{a} \frac{d}{s}\right). \quad (1)$$

From Eq. (1), it can be observed that, aside from the recording wavelength and the diameter of the experimental pinhole, the angle θ_I is proportional to the factor d/s for $\theta_I < \pi/2$. This result implies that if an illumination wavelength $\lambda_I > \lambda_R$ is used, the HPS will produce a larger angle for the resulting illumination cone when compared with that attained by the equivalent pinhole-based method. Larger illumination angles are advantageous in DLHM, as larger numerical apertures can be obtained. It must also be noted that, since the resolution limit is proportional to the illumination wavelength, using a larger wavelength will penalize the lateral resolution of the system. Therefore, a trade-off between the illumination NA and λ_I must be considered when designing the HPS-DLHM configuration. Nevertheless, with our proposal, the system's lateral resolution can be easily tuned by selecting the appropriate recording and reconstruction wavelengths and the DLHM geometry.

To acquire DLHM holograms using the spherical illumination provided by the illuminated HPS (HPS-DLHM), the experimental sample and the digital sensor must be located as shown in Fig. 1(b). In that illustration, z is the reconstruction distance, i.e., the distance between the real image of the pinhole (the point source) and the sample plane; L is the distance between the point

source and the camera sensor plane. According to this geometry, the magnification of the DLHM system is given by $M = L/z$, and its numerical aperture by $NA = W/2\sqrt{(W/2)^2 + (L-z)^2}$, where W is the camera sensor's size [9]. This numerical aperture of the DLHM system yields a lateral resolution $S \geq \lambda_i/2NA$, where λ_i is the illumination wavelength used during the acquisition of the DLHM holograms. The latter expressions for NA and S hold provided the detector sampling is smaller than the theoretical lateral resolution and the divergent illumination covers the full sensor area. Our proposed HPS-DLHM provides a new possibility for DLHM: the reconstruction distance z can be as short as desired. Thus, larger magnifications can be achieved compared with traditional pinhole-based illuminations in which the mechanical coupling of the pinhole physically limits the actual minimum reconstruction distance.

A numerical reconstruction process is mandatory to recover the sample's optical information from its digitally acquired HPS-DLHM hologram. The diffraction process that a converging spherical wavefront $\exp[-i\vec{k} \cdot \vec{r}]/|\vec{r}|$ suffers as it illuminates a given DLHM hologram and propagates toward the sample plane reproduces its complex-valued diffracted wave field. In DLHM, this diffraction process can be numerically described through a scalar diffraction formula [17]. The exact details of the most suitable numerical reconstruction method in DLHM can be read in [21].

To validate our proposal, experimental samples of biological specimens have been imaged with our HPS-DLHM and compared against the results from conventional DLHM. The first validation sample was a honeybee leg from a prepared Amscope glass. For this sample, the digital holograms have been acquired using 632.8 nm wavelength laser illumination and a DLHM geometry of $z = 5$ mm, $W = 3.6$ mm, $L = 10$ mm to yield a magnification $M = 2\times$ and a lateral resolution $S = 0.9 \mu\text{m}$. In Fig. 2, the retrieved intensity reconstructions from the proposed HPS-DLHM [panel (a)] and conventional DLHM [panel (b)] are presented. We also demonstrate the QPI capability of our proposal for a low-absorption sample of cheek epithelial cells. In this case, the digital holograms were acquired with $\lambda_i = 473$ nm, $z = 2.1$ mm, $L = 10$ mm and $W = 3.6$ mm to attain $S = 1.1 \mu\text{m}$. The reduced reconstruction distance of 2.1 mm, easily achieved in our HPS-DLHM, provided $M = 5\times$. The resulting phase reconstructions are presented in Fig. 2: panel (c) shows the retrieved wrapped phase map according to our HPS-DLHM proposal, and panel (d) shows the reconstruction retrieved employing conventional DLHM. For both experiments, the average normalized intensity (or wrapped phase) μ and its standard deviation σ have been computed as a measure of the background noise for the rectangular regions enclosed by the red boxes in all panels [22]. As can be seen, similar normalized intensity or wrapped phase values (along with a slightly lower standard deviation) are attained by our method compared with the conventional approach. As for the quality of the retrieved intensity reconstruction, the smallest details of the intricate honey leg sample are successfully recovered by our method [see the zoomed-in areas in Fig. 2(a) and 2(b)]. Likewise, for the epithelial cells, their distinctive nuclei and cellular membranes are retrieved successfully, as indicated by the dark blue arrows in both wrapped phase maps of panels (c) and (d).

After an unwrapping procedure, 3D optical thickness representations of sections including and surrounding the cells were obtained, as presented in the insets (e) and (f) inside Figs. 2(c) and 2(d), respectively. Similar QPI values were obtained with

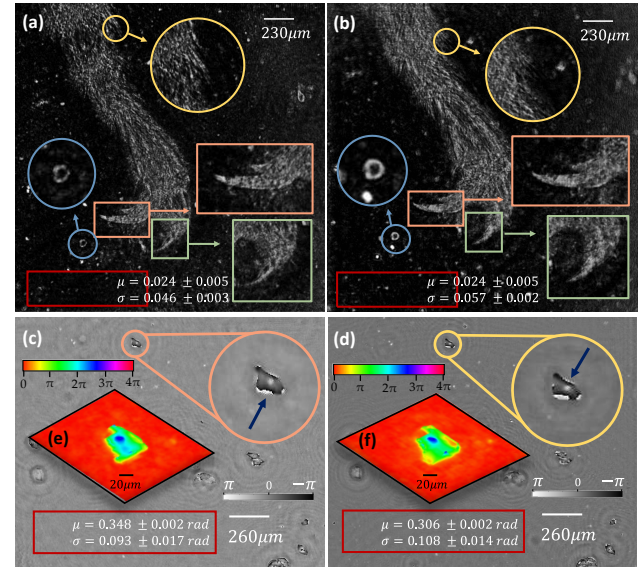


Fig. 2. Intensity reconstruction of a honeybee leg using (a) our HPS-DLHM proposal and (b) conventional DLHM. Raw (wrapped) phase reconstructions and unwrapped 3D topographic views of cheek epithelial cells. Panels (c) and (e) were obtained with our HPS-DLHM, and (d) and (f) via conventional DLHM.

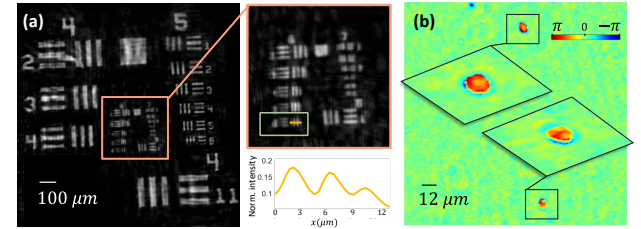


Fig. 3. Further validation of our HPS-DLHM. (a) Intensity reconstruction of a positive 1951 USAF test target to assess the experimental lateral resolution of the proposal. (b) Resulting raw (wrapped) phase map of smeared human erythrocytes using a large-magnification configuration (15 \times).

both techniques. Overall, the intensity and quantitative phase values attained by both techniques are in close agreement in the experiments.

A positive 1951 USAF test target has been imaged to assess the experimental lateral resolution achieved by our proposal. The HPS used for this experiment was recorded with $\lambda_R = 488$ nm and $\theta = 40^\circ$. This HPS-DLHM hologram was registered with $\lambda_i = 488$ nm and a geometrical configuration of $L = 30$ mm, $z = 15$ mm, $W = 4.8$ mm, establishing a theoretical $S = 1.54 \mu\text{m}$. The results are depicted in Fig. 3(a). The smallest resolvable group can be seen in the zoomed-in area: element 6 of group 6 (enclosed by the green box). The corresponding intensity profile along a line (orange) passing through the group is also presented. This result indicates an experimental $S = 4.38 \mu\text{m}$. The following factors explain the difference between the experimental and theoretical lateral resolutions. (i) The limitation of the numerical reconstruction method in any DLHM realization regarding the impossibility of properly modeling an experimental non-perfect spherical illumination wavefront. (ii) The detector sampling. (iii)

Dust particles and other noise sources during the HPS recording affect the provided reconstructions. These factors will be thoroughly investigated and quantified in future work. Finally, a sample of smeared human erythrocytes has been selected to test our proposal in an experiment requiring larger magnification. The HPS and the recording parameters used for this sample were similar to those employed to image the epithelial cells ($\lambda_i = 473$ nm, $z = 1$ mm, $L = 15$ mm, and $W = 3.6$ mm). In this case, $M = 15\times$ and a theoretical $S = 1.9\ \mu\text{m}$ have been accomplished. The wrapped phase map provided by our method in this experiment is presented in Fig. 3(b). As can be appreciated from this panel and the zoom-in 3D views, individual erythrocytes are properly imaged by our method, thus validating that our HPS-DLHM can provide suitable larger magnifications.

In summary, we have proposed a new holographic point source (HPS) for DLHM illumination. The HPS is recorded using a cost-effective off-the-shelf holographic film in an amplitude division interferometer adjusted to meet the optimum manufacturer parameters for maximum diffraction efficiency. Once the HPS is recorded, it is illuminated to produce the illumination required in DLHM. Our proposed HPS-DLHM has been demonstrated with an intricate sample of a section of a honeybee leg and a low-absorption sample of cheek epithelial cells, which yielded similar measurements when contrasted with conventional DLHM. In order to test our system in terms of the achievable experimental lateral resolution and a larger magnification configuration, images of a 1951 USAF test target and smeared human erythrocytes have been retrieved, respectively. Although our proposal successfully provides easy-to-implement (no pinhole required) high-magnification configurations in DLHM ($15\times$), a loss of experimental lateral resolution is obtained compared with the theoretical expectation. The HPS-DLHM proposal provides two additional advantages compared with DLHM. (i) The high mechanical stability conditions required to assure and maintain the proper alignment of conventional point sources are no longer required. (ii) Since a longer wavelength (compared with the wavelength used in the recording process) can be used to illuminate the HPS, smaller pinhole images are formed; thus, wider spherical illumination cones, i.e., potentially higher numerical apertures of the illumination, can be attained. The latter is achieved at the expense of penalizing the system's lateral resolution in terms of the selected illumination wavelength. The advantages of our HPS-DLHM will extend the use of DLHM in in-field applications where mechanical stability, cost-effectiveness, and larger magnifications are demanded of this single-shot technique.

Funding. Universidad EAFIT.

Acknowledgment. The authors acknowledge the support provided by Vicerrectoría de Ciencia, Tecnología e Innovación from Universidad EAFIT.

The authors also acknowledge the unique collaboration of Professor MSc. Daniel Velásquez in this project and for his entire research life dedicated to holography.

Disclosures. The authors declare no conflicts of interest.

Data availability. Data underlying the results presented in this paper are not publicly available at this time but may be obtained from the authors upon reasonable request.

REFERENCES

- W. Xu, M. H. Jericho, I. A. Meinertzhagen, and H. J. Kreuzer, *Proc. Natl. Acad. Sci. U. S. A.* **98**, 11301 (2001).
- E. McLeod and A. Ozcan, *Phys. Today* **70**, 50 (2017).
- H. Tobon-Maya, S. Zapata-Valencia, E. Zora-Guzmán, C. Buitrago-Duque, and J. Garcia-Sucerquia, *Appl. Opt.* **60**, A205 (2021).
- M. Sanz, J. A. Picazo-Bueno, J. García, and V. Micó, *Lab Chip* **18**, 1105 (2018).
- O. Mudanyali, D. Tseng, C. Oh, S. O. Isikman, I. Sencan, W. Bishara, C. Oztoprak, S. Seo, B. Khademhosseini, and A. Ozcan, *Lab Chip* **10**, 1417 (2010).
- A. Ozcan, *Biosensing Nanomedicine VII* **9166**, 91660K (2014).
- X. Wu, J. Sun, J. Zhang, L. Lu, R. Chen, Q. Chen, and C. Zuo, *Opt. Lett.* **46**, 2023 (2021).
- S. Seo, T.-W. Su, D. K. Tseng, A. Erlinger, and A. Ozcan, *Lab Chip* **9**, 777 (2009).
- J. Garcia-Sucerquia, W. Xu, S. K. Jericho, P. Klages, M. H. Jericho, and H. J. Kreuzer, *Appl. Opt.* **45**, 836 (2006).
- C. Trujillo and M. J. Lopera, *Front. Opt. + Laser Sci.* **1**, JTh5A.14 (2021).
- B. Peruchio and V. Micó, *J. Biomed. Opt.* **19**, 016017 (2014).
- A. Calabuig, E. Tajahuerce, J. Lancis, J. Garcia-Sucerquia, O. Mendoza-Yero, and P. Andrés, *Opt. Lett.* **38**, 3205 (2013).
- Z. Frentz, S. Kuehn, and D. Hekstra, *Rev. Sci. Instrum.* **81**, 084301 (2010).
- L. Waller, M. Tsang, S. Ponda, S. Y. Yang, G. Barbastathis, Z. Wang, L. Millet, M. Mir, H. Ding, S. Unarunotai, J. Rogers, M. U. Gillette, G. Popescu, D. L. Marks, P. S. Carney, L. J. Millet, A. Mihi, P. V. Braun, Z. Shen, and S. G. Prasanth, *Opt. Express* **20**, 3129 (2012).
- M. Sanz, M. Trusiak, J. García, and V. Micó, *Opt. Lasers Eng.* **127**, 105939 (2020).
- G. Ackermann and J. Eichler, *Holography: a Practical Approach* (Wiley-VCH, 2007).
- J. W. Goodman, *Introduction to Fourier Optics* (Roberst & Company Publishers, 2005).
- Diffraction Optical Elements Market Trends & Forecast by 2027 (Transparency Market Research, 2021).
- H. Kim, J. K. Hwang, M. Jung, J. Choi, and H. W. Kang, *Biomed. Opt. Express* **11**, 7286 (2020).
- Litiholo, *Litiholo 2.0 C-RT20 Film Data Sheet* (n.d.), <https://litiholo.com/>.
- C. Trujillo, P. Piedrahita-Quintero, and J. Garcia-Sucerquia, *Appl. Opt.* **59**, 5788 (2020).
- H. Tobon, C. Trujillo, and J. Garcia-Sucerquia, *Appl. Opt.* **60**, A215 (2021).

MANUSCRIPTS TO BE SUBMITTED



Freeform lens-based illumination source for digital lensless holographic microscopy

MARIA J. LOPERA,^{1,A} YUNFENG NIE,² CARLOS TRUJILLO,^{1,B} AND HEIDI OTTEVAERE^{2,C}

¹*Applied Optics Group, School of Applied Science and Engineering, Universidad EAFIT, Medellin, Colombia.*

²*Brussels Photonics, Department of Applied Physics and Photonics, Vrije Universiteit Brussel and Flanders Make, Pleinlaan 2, B-1050 Brussels, Belgium.*

^Amloper23@eafit.edu.co

^Bcatrujilla@eafit.edu.co

^Cheidi.ottevaere@vub.be

Abstract: Digital Lensless Holographic Microscopy (DLHM) is the simplest and most affordable method to recover 3D information from microscopic samples. However, new approaches involving mechanically highly stable setups and miniaturized implementations in up-to-date portable applications are still needed. In this work, we report the design and fabrication of a freeform (FF) lens used to obtain spatially coherent illumination as required by DLHM (FF-DLHM). The design has been validated regarding the achievable lateral resolution of the system employing two different setups. The assembled FF-DLHM setup achieves imaging performance similar to the conventional methods, avoiding complicated pinhole-based implementations and using only a compact and small element after the illumination source. In addition, a direct comparison of the achieved amplitude and phase imaging results on biological and non-biological samples against conventional DLHM and a high-performance DHM system is provided.

© 2022 Optica Publishing Group under the terms of the [Optica Publishing Group Open Access Publishing Agreement](#)

1. Introduction

Digital Lensless Holographic Microscopy (DLHM) is the simplest imaging method to recover information from microscopic samples [1]–[3], avoiding bulky, expensive hardware [3]–[5]. This technique allows the numerical retrieval of the complete optical complex wavefield scattered by the specimens, thus providing numerical refocusing of individual objects [6]–[8] and phase information of transparent samples [9]. As a result, numerous applications of DLHM in medicine and biology have been reported [10]–[13]. For instance, the underwater observations of biological processes [14], applications to point-of-care diagnostics [15], [16], the observation of intricate biological samples [17], blood cell analysis on a chip [18], analyzing sperm motility [19], early detection of diseases [15], [20] and parasites [21], and characterization and detection of birefringent components via linear diattenuation measurements [22], among many others [23]–[27].

As with any other digital holography implementation, DLHM is a two-step technique: holograms of the studied sample are first recorded in a digital camera, and then further numerical processing allows the retrieval of its information in a plane-by-plane fashion [3]. A simple instrument comprising merely a digital sensor and an illumination point source is required in the recording stage. Notwithstanding its simplicity, significant efforts to enhance the technology in various aspects are continuously reported [28]. For instance, to achieve polarization sensitivity, proposals involving the insertion of polarizing elements in the typical DLHM setup with additional numerical procedures have been reported [22], [29]. To facilitate the portable application of DLHM, proposals involving miniaturized implementations [30], cellphone-based adaptations [31], [32], and conventional LED illumination [33] have been

reported. Also, to reduce DLHM costs, reports on 3D-printed setups utilizing off-the-shelf materials [34], lens-free microscopes on a chip [35], and multi-illumination single-holographic-exposure lensless Fresnel microscopy [36] are accounted.

The modality of DLHM in which large magnifications are desired requires spherical illumination sources with high divergence and spatial coherence [3]. The magnification in the DLHM technique is performed by the sole propagation of the light scattered by the specimens to the camera sensor. The conventional single-shot DLHM proposal employs microscope objectives to focus a collimated light beam from the light source into micrometrical pinholes [3], [34]. The illumination cone divergence, in this case, depends on the focal length of the microscope objective [3]. Implementing this system implies a rigorous alignment process and expensive optical elements. Proposals have emerged to overcome pinhole-based system drawbacks such as the use of LED [32] and SLED [37] sources, pulsed laser radiation [10], illumination through GRIN lenses [38] or fiber optics [39], the use of an electrically tunable lens [40], and holographic optical elements [41]. Although these proposals provide good performance, they still have significant drawbacks: they involve bulky, expensive, unstable hardware, and they are not meant for miniaturized DLHM. Proposals involving point sources that provide larger numerical apertures, shorter source-to-sample distances, and increased mechanical stability without adding complexity to the technique are still needed.

The freeform-based design has introduced new possibilities for compact packaging and high performance, thanks to the rapid advance in precise fabrication and replication of optical components with almost any shape [42]. Freeform surfaces aim to efficiently control the redistribution of light from a particular source to a target irradiance [43]. By offering more degrees of design freedom compared to common spherical/conic surfaces, freeform optics helps to develop more compact and better-performing optical systems [44], such as spectrometers [45], [46], tailored illumination [47], and augmented reality [48].

In this work, we report a freeform lens-based illumination source for DLHM to overcome the current limitations of the technique, in particular, the need to avoid pinhole-based setups and to provide compact miniaturized solutions. In the following section, we present the design and fabrication of the freeform lens-based proposal, considering the conditions for optimal DLHM illumination. The description of the FF-DLHM setup and its reconstruction procedure are described in section 3. Section 4 includes a complete validation of the proposal involving lateral resolution performance, a comparison with the conventional DLHM method and an expensive high-performance DHM system. Finally, conclusions and future work are given.

2. Freeform lens-based point source design and implementation

To derive the requirements for proper illumination, we present the principle of DLHM and the main factors that limit the lateral resolution of the technique. After that, the optical design of a freeform lens-based point source has been proposed to meet the illumination requirements, and the fabrication of this optical element was performed.

2.1. DLHM spherical wavefront requirements

In a typical DLHM setup, the sample is placed in between the illumination source and the camera sensor to produce and record a magnified diffraction pattern of the specimen, as can be observed in Fig. 1. This acquisition, called DLHM hologram, is numerically processed in a computer to recover the sample's amplitude and phase information. Further details on the numerical reconstruction stage in DLHM are provided in section 3.

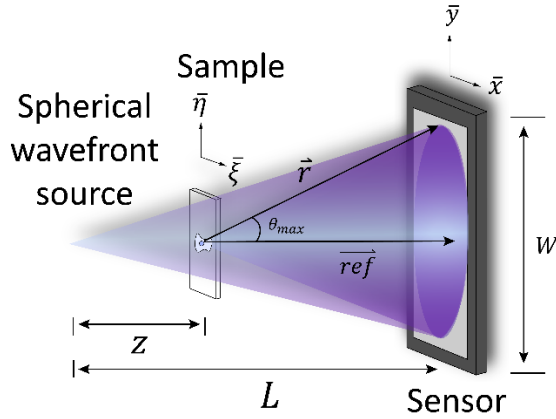


Fig. 1. Scheme of a Digital Lensless Holographic Microscopy setup.

According to the DLHM scheme in Fig. 1, the system's numerical aperture is defined by the cone of light which divergence is determined by θ_{max} [11], [49].

$$NA = n \sin \theta_{max} = n_2 \frac{W}{2 \sqrt{\left(\frac{W}{2}\right)^2 + (L-z)^2}}. \quad (1)$$

According to Abbe's diffraction limit of microscopy, the lateral resolution of a microscope is defined as,

$$\Delta x \sim \frac{\lambda}{2NA}. \quad (2)$$

This expression establishes the maximum achievable resolution in a DLHM configuration. However, several factors limit the amount of information that can be recorded and reconstructed with the DLHM technique. The main factors limiting the resolution of the technique are:

- The signal-to-noise ratio and sample-to-background contrast depend on the sample's size, the diffracted intensity, and the contrast of the diffraction pattern at the detector plane [50], [51].
- Spatial aliasing is present when the sensor undersamples the fringes, which produces distortions and fake features of the object [51].
- The limited temporal or spatial coherence limits the maximum observable fringe frequency.

The first two limitations can be minimized by properly selecting the samples and sensor features. The third limitation is mainly imposed by the illumination source's features and the spherical wavefront construction [3]. The highest resolvable spatial frequency that can be encoded into a diffraction pattern depends on the coherence degree of the illumination source [4]. To encode higher spatial frequencies, sources with a high degree of temporal or spatial coherence must be used. When continuous-wave (CW) lasers are used as light sources, high temporal coherence is achieved, and the diffraction pattern is limited by the coherence length of the source [4]. Nevertheless, as lensless microscopy is a technique seeking affordable, simple implementations, broadband light sources are preferred [34] at the expense of losing spatial resolution [52]. Likewise, the spatial coherence of the source also limits the sample's information encoded in the recorded diffraction pattern. The spatial coherence of the imaging

system is given by the diameter of the light source aperture (D) and the distance between the aperture and the sample (z) [53]. The light scattered by the object (\vec{r}) will diffract within a coherent cone whose vertex is located at the sample plane and its circular basis at the sensor plane. The circular basis diameter of the coherent cone is established by the first zeroth order of the coherence of the light source [4], [52], [53].

$$d_0 = 1.22 \frac{\lambda z}{D}. \quad (3)$$

The maximum spatially coherent scattering angle is defined then by the angle θ_{max} [4],

$$\theta_{max} = \arctan\left(\frac{d_0}{2[L-z]}\right). \quad (4)$$

Furthermore, the numerical aperture of the spatially coherent cone immersed in a medium with refractive index n can be found as follows.

$$NA = n \sin \theta_{max} = n \sin\left(\arctan\left(\frac{d_0}{2[L-z]}\right)\right). \quad (5)$$

Following Eq. (2), one must increase the numerical aperture to enhance the system's lateral resolution, which can be achieved by increasing the maximum spatially coherent scattering angle of the DLHM setup [Eq. (4) and Eq. (5)]. Moreover, high spatial coherence must be attained, i.e., the source aperture's diameter must be as small as possible, ideally, a point source [Eq. (3)]. Consequently, an illumination producing large divergent cones from point sources will provide DLHM setups with better imaging performance.

2.2. Optical design of the freeform lens-based point source

2.2.1 Illumination source

A laser diode has been selected as the illumination device for the freeform lens-based point source design. Laser diodes are semiconductor-based devices in which an electrically pumped media creates lasing conditions at the diode's junction. As the gain media is a thin intrinsic layer, when single mode light is generated in this optical cavity, different gaussian distributions are emitted along the x- and y-axis. As a result, the irradiance pattern of such devices is astigmatic [54]. The spectrum and the x/y divergences of the selected laser diode have been experimentally measured using a spectrometer (Avantes AvaSpec 2048) and a beam profiler (Gentec Beamage). The results are characterized and shown in Table 1. As we can see, the laser diode spectral bandwidth (in full width half maximum, FWHM) is 8nm with 20.0 mW power, while there is a big difference in X and Y divergence. These parameters are then simulated as an elliptical, divergent laser source.

Table 1. Parameters of the laser diode used for the development of the FF-DLHM proposal.

Central Wavelength (nm)	Spectral FWHM (nm)	X divergence (deg)	Y divergence (deg)	Power (mW)
407	8	12.5 ± 0.2	23.7 ± 0.3	20.0 ± 0.1

2.2.2 Freeform lens

A freeform lens is an optical element that includes surfaces lacking transitional or rotational symmetry. With more degrees of design freedom, this type of optical surfaces can bring up many potential advantages, including system miniaturization, reduced number of optical surfaces/components, and new optical functionality [44]. For this design, the freeform surface is mathematically represented by a spherical basis and the freeform departure portion as follows:

$$z(x, y) = \frac{c(x^2 + y^2)}{1 + \sqrt{1 - c^2(x^2 + y^2)}} + \sum_{m=0}^M \sum_{n=0}^N A_{mn} x^m y^n \quad (6)$$

Where, c is the spherical curvature, A_{mn} are the corresponding coefficients of the extended freeform polynomial terms. The first term is rotationally symmetric for focusing light, and the difference of x - and y - polynomial coefficients can well compensate the astigmatism originated from a real laser diode.

We perform the raytracing process and subsequent optimization in OpticStudio [55]. An extended polynomial lens is inserted at a distance d from the laser diode (an elliptical source). The front surface is freeform; the rear surface is set to be flat for easier assembly. We define the even-terms of the freeform surface as variables, given that the design has plan symmetries. The merit function has been set to minimize the spot radius on the rear surface and to maximize the flux irradiance on the sensor located at a distance L from the rear facet. The optical raytracing process of the design is shown in Fig. 2.

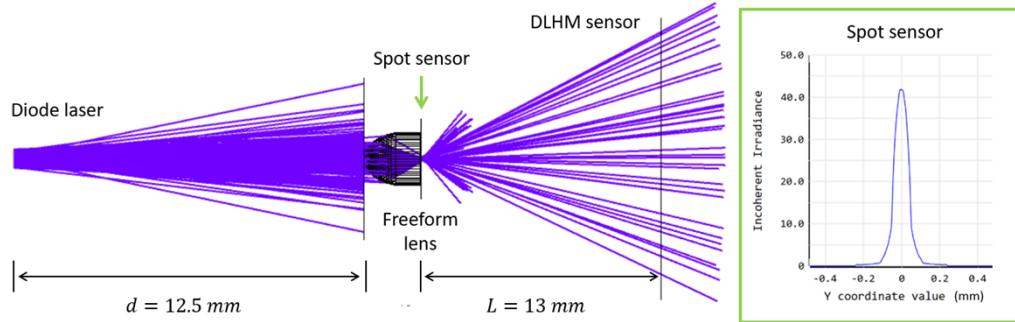


Fig. 2. The optical layout of the freeform-based source design

The irradiances at the rear surface of the lens and the DLHM sensor location after the optimization are shown in Fig. 3(a) and 3(b) respectively. The resultant spot has an FWHM of $80\mu\text{m}$ at the rear face of the lens (as can be visualized in the crossed section shown in Fig. 2). In this design, a virtual 14×14 mm detector located at $L=13\text{mm}$ from the source is used to measure the beam diameter. The sensor is 67% illuminated at this location, resulting in a spot with a $1/e^2$ beam diameter of 8.1 mm. This illumination cone has a numerical aperture of 0.297.

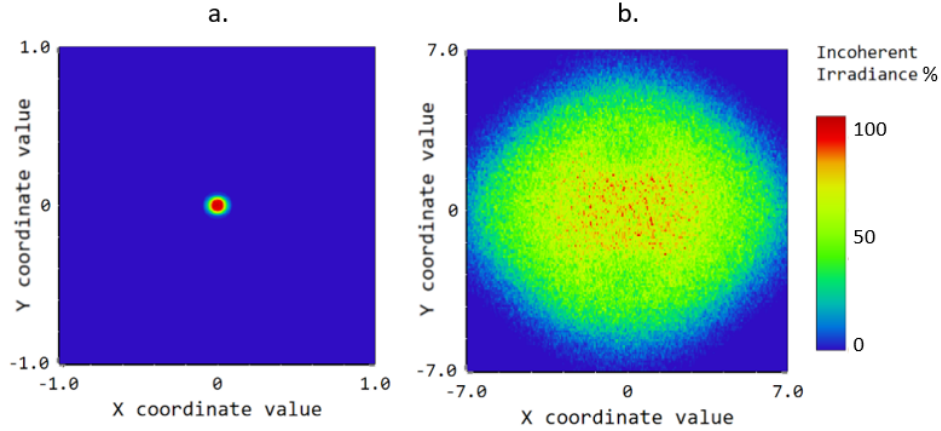


Fig. 3. (left) Irradiance distribution at the rear surface of the lens and (right) irradiance distribution at the virtual sensor.

2.3. Tolerance analysis and fabrication of the freeform lens

As we know that perturbations from lens fabrication and the system assembly could happen on top of the nominal design, a tolerance analysis was performed to quantify the influences. The resulted tolerance values are displayed in Table 2, which are determined as the ranges that causes less than 3% reduction in irradiance. These values are also used to guide the fabrication and select assembly holders.

The proposed freeform lens has been fabricated using a blank of PMMA polymer material. Ultraprecision Diamond Tooling (UDT, Nanotech 350FG) has been used to fabricate this lens accurately via the Slow Slide Servo process. In this cutting strategy, the C-axis (workpiece) is indexed and rotated synchronously with the position of the Z-axis (optical axis) on which the diamond tool is mounted. The settings for this tool are respectively: 0.461mm radius, 100° window, 10° flank angle, and 0.1μm waviness, with 40-degree rotation to be able to cut the entire surface of the freeform lens. A picture of a simulation of the manufacturing process is presented in Fig. 4 (a).

Table 2. Tolerance analysis parameters for the freeform lens fabrication and assembly

(mm)	Source-lens position	Radial height	Thickness	Front surface Radius	Freeform sag
Value	17.5	1.3	2.8	3.9	N/A
Tolerance	±0.1	±0.1	±0.1	±0.1	±0.05

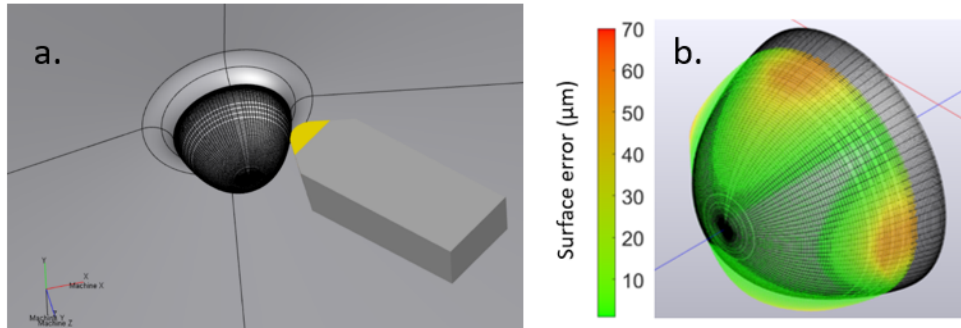


Fig. 4. (a) Image of the Slow Slide Servo process simulation to fabricate the freeform lens. (b) Surface error measurements of the fabricated freeform lens.

The final dimensions of the freeform surface have been measured using a Coordinate Measurement Machine (CMM, Werth UA400 3D); the result is presented in Fig. 4 (b). The dimension error is, on average, $12\ \mu\text{m}$ over the entire surface. The error obtained from the fabrication process is under the allowed tolerance (Table 2) of the design, thus having minimal effect on the resulting irradiance.

2.4. Divergence of the spherical wavefront source

The divergence cone of the spherical wavefront illumination generated by the fabricated freeform lens defines the maximum numerical aperture of the illumination, thus the minimum resolution achievable in DLHM. According to the optical simulation results of the lens, the $1/e^2$ beam width obtained on a plane located at a distance $L = 13\ \text{mm}$ is $8.1\ \text{mm}$. A beam profiler has been placed at a distance $L = 13\ \text{mm}$ from the rear face of the lens to measure the beam width experimentally. The measurement was repeated five times to mitigate the positioning error. The beam width obtained experimentally is $7.9 \pm 0.2\ \text{mm}$. According to simulation values, the expected beam divergence is 32.8 degrees, and the result obtained experimentally is 32.6 ± 0.6 degrees. Based on the obtained divergence of the beam, both simulated and experimentally determined, the numerical aperture of this cone of light is 0.29 ± 0.09 , which is within the range of numerical apertures to achieve state-of-the-art lateral resolutions in DLHM.

3. Freeform lens-based Digital Lensless Holographic Microscopy (FF-DLHM)

The designed and fabricated freeform lens provides the spherical wavefront source that meets the coherent requirements needed for DLHM. To acquire DLHM holograms with this element, the laser diode must be placed at a distance $f = 17.5\ \text{mm}$ from the front face of the lens, as designed; the tolerance for this positioning is up to $0.1\ \text{mm}$ according to the simulations. As diode lasers are astigmatic sources, their alignment is crucial. In this case, the minor axis of the source must be aligned with the x-axis of the DLHM configuration. The sample and the sensor are located as shown in Fig. 5. The reconstruction distance z and the distance between the point source and the sensor L could be modified to achieve the desired magnification M ($M = L/z$) and numerical aperture (Eq. (1)) [56].

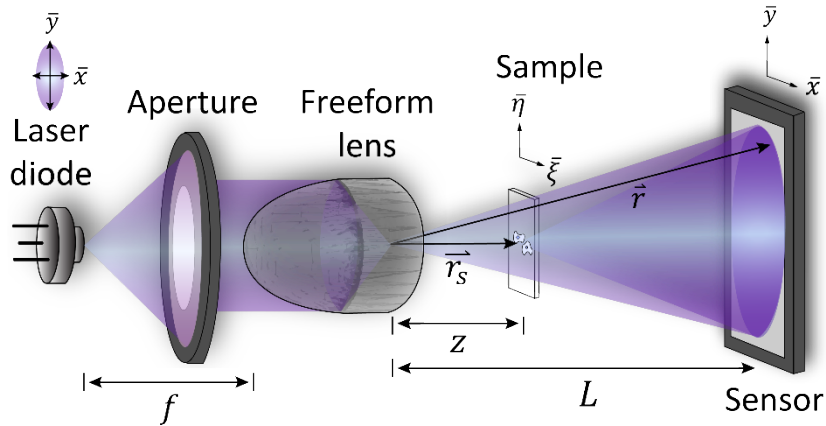


Fig. 5. Scheme of the Freeform lens-based Digital Lensless Holographic Microscopy (FF-DLHM).

A numerical reconstruction process is mandatory to recover the sample's optical information from its digitally acquired FF-DLHM hologram. A converging spherical wavefront source $\frac{\exp[-i\vec{k} \cdot \vec{r}]}{|\vec{r}|}$ is numerically diffracted through the hologram and it reproduces the complex-valued diffracted wavefield of the sample. In DLHM, this diffraction process can be numerically described through a scalar diffraction formula [57]. The optical field of the sample $S(\vec{r}_s)$ at the position $\vec{r}_s = (\xi, \eta, z)$ can be found by retro-propagating a spherical wavefront as expressed in Eq. (7)

$$S(\vec{r}_s) = \frac{z}{i\lambda} \int I(\vec{r}) \frac{\exp[-i\vec{k} \cdot \vec{r}]}{|\vec{r}|} \frac{\exp[-i\vec{k} \cdot (\vec{r} - \vec{r}_s)]}{|\vec{r} - \vec{r}_s|} d\vec{r} \quad (7)$$

Where, \vec{r} is the vector denoting the position on the sensor plane (x, y, L) , and $I(\vec{r})$ is the DLHM hologram [22], [58]. From Eq. (7), one can compute the intensity $I = S(\vec{r}_s) * S^*(\vec{r}_s)$ or phase $\phi = \arctan(\frac{\text{Im}\{S(\vec{r}_s)\}}{\text{Re}\{S(\vec{r}_s)\}})$ of the sample, with Im and Re the imaginary and real parts, respectively.

4. Results and discussion

To fully validate the proposed FF-DLHM, the achievable lateral resolution of the system is reported in this section. We also validate the system by analyzing some biological samples and performing quantitative phase imaging (QPI).

4.1. Experimental lateral resolution measurement.

Two setups with different NA have been implemented to measure the achievable lateral resolution by the proposed FF-DLHM. These NAs were set to experimentally measure the resolution by means of a USAF resolution target. For these experiments, the laser diode described in previous sections is the illumination source, a Thorlabs camera with a 3.7×3.7 mm² sensor size and a 3.6 μm pixel pitch records the holograms, and a USAF test target is the imaged sample. The L and z distances to attain two different NA setups are presented in Table 3.

Table 3. Parameters of the two implemented setups to measure the lateral resolution attained by the FF-DLHM.

Setup	L (mm)	z (mm)	NA	Expected resolution (μm)	Experimental resolution [group] (μm)
1	28	9	0.06423	3.17	[7-3] 3.105
2	19	4	0.0943	2.16	[7-6] 2.19

The intensity reconstruction of the sample for both setups is presented in Fig. 6. Panel (a) shows the reconstruction using setup 1, and panel (b) shows the result obtained with setup 2. As expected, the lateral resolution attained with setup 2 is the lowest on the resolution chart, which implies that a higher resolution of the USAF test could be resolved. With setup 1, the smallest resolvable element of the test target is 7-3; the crossed section of this group is shown in panel (c). The fringes present a contrast of 0.31 ± 0.05 , yielding an experimental lateral resolution of 3.1 μm . As for setup 2, the smallest resolvable element is 7-6, with a contrast of 0.44 ± 0.03 ; a 2.19 μm experimental lateral resolution is achieved, panel (d). The experimental lateral resolutions for both setups attained by the FF-DLHM are in remarkable agreement with the

theoretical expectation, thus confirming that the required spatial resolution of the DLHM illumination is met by the proposed FF-based method.

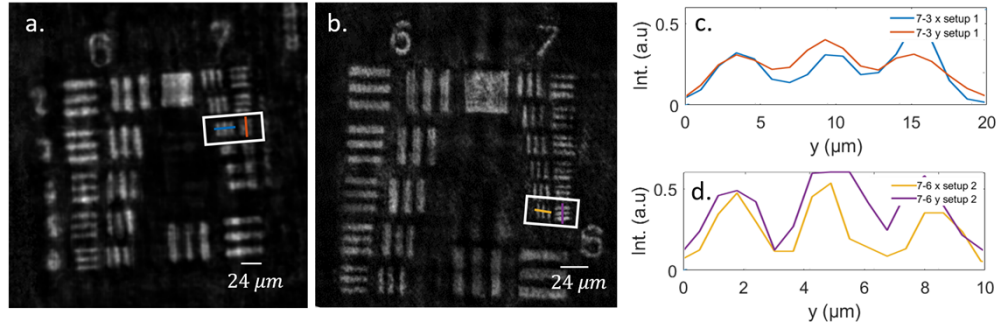


Fig. 6. Intensity reconstructions of USAF test target using two proposed FF-DLHM setups with (a) 3.1 μm (a) and (b) 2.2 μm lateral resolution. (c) and (d) are the cross-section intensity profiles of the two line-pair groups on the USAF chart for extracting lateral resolutions

4.2. Validation of the setup with biological samples

To validate the capability of our proposal to reconstruct amplitude and phase information correctly, a hologram of a sample containing mouth fluid (saliva) has been imaged with the FF-DLHM technique and with the conventional pinhole-based DLHM [3], [22], using a 3 μm pinhole. For both techniques, the same geometrical parameters have been applied. A 1024×1024 pixels camera from Thorlabs is used as a digital sensor, this sensor has a width of $W = 3.7$ mm, and the distances L and z have been set to 12 mm and 4 mm, respectively. The latter setup yields an optical magnification of 3×, a numerical aperture and lateral resolution of 0.2195 and 0.93 μm, and a field of view of 1.2 mm x 1.2 mm. The results provided by both techniques are compared and presented in Fig. 7 and Fig. 8.

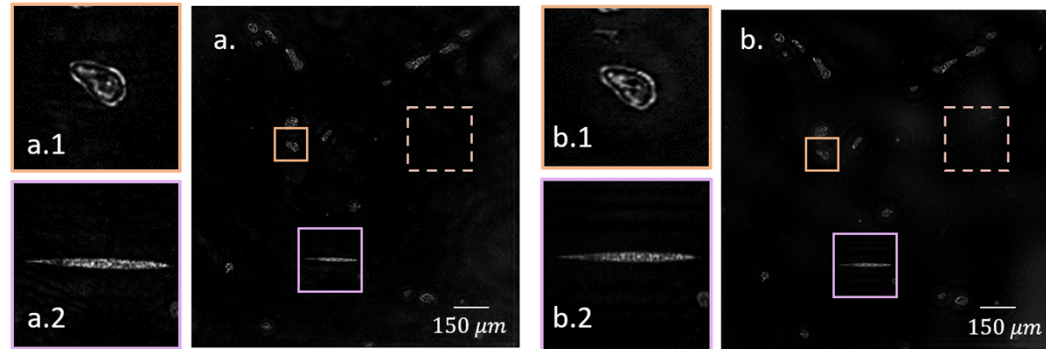


Fig. 7. Intensity reconstruction of a sample containing epithelial cheek cells (saliva) with (a) the proposed FF-DLHM and (b) with a conventional pinhole-based DLHM.

The results show that the sample mainly comprises epithelial cheek cells and leukocytes. Panel (a) presents the intensity information recovered using the FF-DLHM, and panel (b) the intensity reconstruction with the pinhole-based DLHM. The intensity information of the sample is properly recovered with both techniques. Insets a.1 and b.1 show a zoomed-in area containing a single epithelial cell; the sample-to-background contrast inside this area is computed. Inside

the same area, the sharpness of the sample has been evaluated using the maximum of the bidimensional gradient. The background noise is measured with the standard deviation of the background. All the latter measurements are presented in Table 4. Moreover, panels a.2 and b.2 present a zoomed-in area containing a sharper element. In this case, the maximum gradient for the FF-DLHM is 0.3588 and for the pinhole is 0.1588.

Table 4. Parameters of the two implemented setups to measure the lateral resolution attained by the FF-DLHM.

Result with	Sample-background contrast	Sharpness	Background noise
FF-DLHM	0.87	0.3137	0.003 ± 0.001
PH-DLHM	0.79	0.1347	0.003 ± 0.001

According to the results in Table 3, the FF-DLHM intensity reconstructions present higher sample-to-background contrast and sharpness, producing statistically the same background noise than the $3\mu\text{m}$ pinhole-based conventional DLHM method. The phase maps in the same field of views are also presented as in Fig. 8. The background phase value obtained with the FF-DLHM is -0.804 ± 0.02 radians and with the pinhole-based DLHM -0.865 ± 0.01 radians. The FF-DLHM phase reconstruction strongly agrees with the conventional method providing similar phase measurements of the studied sample.

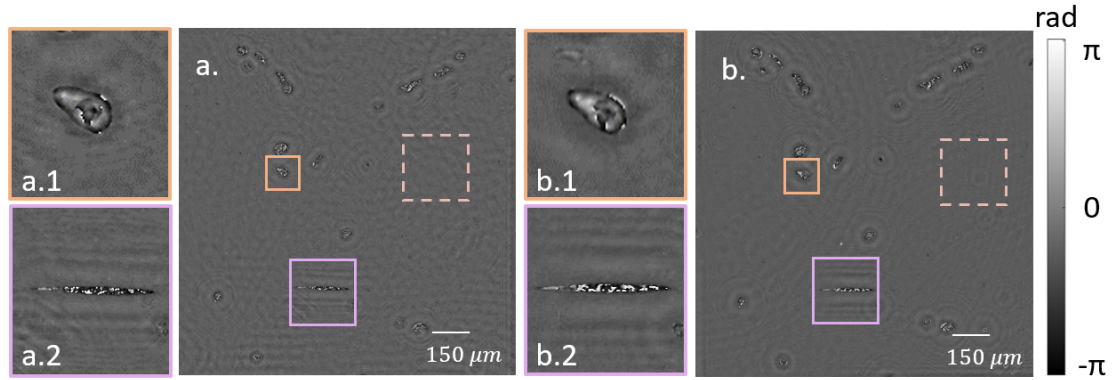


Fig. 8. Phase map reconstruction of a sample containing epithelial cheek cells with (a) the proposed FF-DLHM and (b) a conventional pinhole-based DLHM.

4.3. QPI performance of the FF-DLHM

A phase USAF test target has been imaged to validate the QPI performance of the proposed setup. The values have been compared with a high-performance telecentric image-plane DHM [59], [60]. In the object arm of the DHM, an infinity-corrected Olympus $10\times$ microscope objective with 0.25 NA and a 20mm tube lens comprise the imaging system. This system works in image-plane configuration, and the lenses are fixed in a tight telecentric regime for spherical aberration compensation. As for the FF-DLHM, the same digital sensor as the results presented in section 4.1 has been used with $L = 20$ mm and $z = 3$ mm. The wrapped phase maps obtained are presented in Fig. 9. The groups 6-5 (for the FF-DLHM result) and 6-6 (for the DHM result) have been unwrapped using the puma algorithm [61], and the results are presented in the zoomed areas of Fig. 9. For the element 6-5, the phase value difference between the element and the background via the FF-DLHM is 12.1 ± 0.2 radians. As for the DHM system, this measurement for the element 6-6 obtained is 11.66 ± 0.05 radians. Beyond increased background noise in the obtained phase map of the proposal, these results confirm that the QPI

measurement obtained with the FF-DLHM is highly concordant with that of the high-performance DHM.

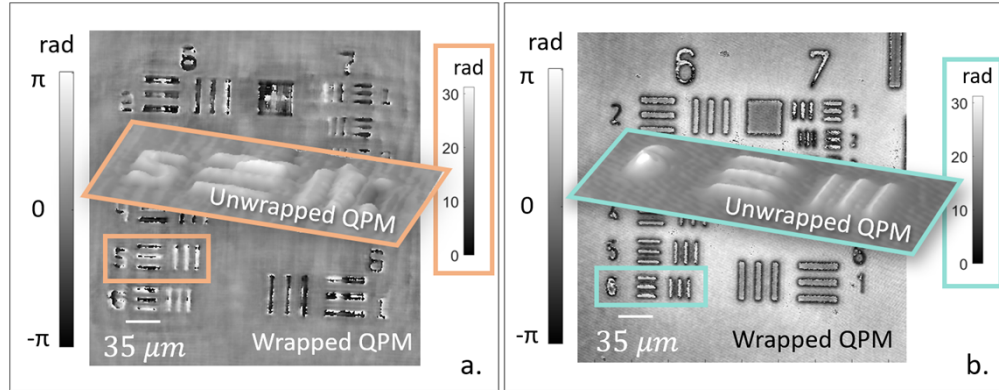


Fig. 9. Quantitative phase maps (QPM) of a phase USAF target recovered using the FF-DLHM (a) and the described DHM (b).

5. Conclusions

This paper presents the design, fabrication, and experimental validation of a freeform lens-based illumination system for digital lensless holographic microscopy (FF-DLHM). The freeform lens consists of an extended polynomial surface carefully optimized to focus the incoming wavefront of a diode laser onto its rear surface. Optical raytracing simulations are provided to guarantee proper imaging performance in DLHM. The lens has been fabricated with PMMA using ultraprecision diamond tooling, also suitable for mass production by molding and replication if needed. Although the lens has been engineered to provide divergent spherical wavefront illumination with NA 0.29 as a specific design, it is still possible to increase the output beam's divergence by changing the lens's design parameters to achieve higher resolutions. To record FF-DLHM holograms, the sample is located after the freeform lens and before the digital sensor, which registers its diffraction pattern. The numerical reconstruction stage remains the same as for conventional DLHM. The proposal is validated by measuring the experimental lateral resolution using a positive USAF resolution test target in two different setups, fulfilling the theoretical expectations. As a second validation, *epithelial cheek cells* are imaged with the FF-DLHM, yielding the same results as conventional pinhole-based DLHM. Finally, an evaluation of the QPI performance of the FF-DLHM is performed by imaging a pure phase USAF test target. For this experiment, the measured phase map with the FF-DLHM agrees with the one obtained via a high-performance DHM system.

To summarize, the experimental resolutions are in good agreement with the theoretical values. The proposed freeform lens-based method allows the proper retrieval of intensity and phase information of micrometrical samples in DLHM achieving comparable results with the pinhole-based DLHM while requiring a much simpler setup and fewer alignments with merely one single optical component. Moreover, this element is highly efficient to enable the usage of cost-effective laser diodes for illuminating the sample. With the simulations and experimental validations, the proposed FF-DLHM setup paves the way for portable miniaturized devices, suitable for various fieldwork applications. In future, we will further investigate the freeform lens-based illumination systems to allow multiple wavelength illumination with higher numerical apertures and to boost the DLHM implementations and their applications.

Acknowledgments.

The authors would like to thank the technological experts at the VUB B-PHOT Photonics Innovation Center who were involved in the development and manufacturing of the freeform lens. M. J. Lopera and C. Trujillo acknowledge the support provided by Vicerrectoría de Ciencia, Tecnología e Innovación from Universidad EAFIT.

Funding.

The authors acknowledge the Flemish Fund for Scientific Research (FWO) for supporting their research (G044516N) and the EU for funding within the Horizon 2020 Program, under the FET-OPEN Project “SensApp”, Grant Agreement n.829104. This research was also supported by the Methusalem and Hercules foundations and the OZR of the Vrije Universiteit Brussel (VUB). Y. Nie acknowledges FWO for her post-doctoral fellowship (No. 1252722N).

Data availability.

The authors confirm that the data supporting the findings of this study are available within the article, and also can be obtained upon reasonable request.

Disclosures.

The authors declare no conflicts of interest.

- [1] E. McLeod and A. Ozcan, "Unconventional methods of imaging: Computational microscopy and compact implementations," *Reports Prog. Phys.*, vol. 79, no. 7, May 2016.
- [2] H. J. Kreuzer, N. Pomerleau, K. Blagrove, and M. H. Jericho, "Digital in-line holography with numerical reconstruction," *SPIE Interferom. '99 Tech. Technol.*, vol. 3744, pp. 65–74, Aug. 1999.
- [3] J. Garcia-Sucerquia, W. Xu, S. K. Jericho, P. Klages, M. H. Jericho, and H. J. Kreuzer, "Digital in-line holographic microscopy," *Appl. Opt.*, vol. 45, no. 5, pp. 836–850, 2006.
- [4] E. McLeod and A. Ozcan, "Unconventional methods of imaging: Computational microscopy and compact implementations," *Reports Prog. Phys.*, vol. 79, no. 7, 2016.
- [5] Y. Wu and A. Ozcan, "Lensless digital holographic microscopy and its applications in biomedicine and environmental monitoring," *Methods*, vol. 136, pp. 4–16, 2018.
- [6] M. Rogalski, J. A. Picazo-Bueno, J. Winnik, P. Zdańkowski, V. Micó, and M. Trusiak, "Accurate automatic object 4D tracking in digital in-line holographic microscopy based on computationally rendered dark fields," *Sci. Reports* 2022 121, vol. 12, no. 1, pp. 1–7, Jul. 2022.
- [7] F. Merola, L. Miccio, P. Memmolo, M. Paturzo, S. Grilli, and P. Ferraro, "Simultaneous optical manipulation, 3-D tracking, and imaging of micro-objects by digital holography in microfluidics," *IEEE Photonics J.*, vol. 4, no. 2, pp. 451–454, 2012.
- [8] G. Coppola *et al.*, "Recent advances in holographic 3D particle tracking," *Adv. Opt. Photonics*, Vol. 7, Issue 4, pp. 713–755, vol. 7, no. 4, pp. 713–755, Dec. 2015.
- [9] Y. Rivenson, Y. Zhang, H. Günaydin, D. Teng, and A. Ozcan, "Phase recovery and holographic image reconstruction using deep learning in neural networks," *Nat. Publ. Gr.*, vol. 7, 2018.
- [10] A. Calabuig, E. Tajahuerce, J. Lancis, J. Garcia-Sucerquia, O. Mendoza-Yero, and P. Andrés, "Femtosecond digital lensless holographic microscopy to image biological samples," *Opt. Lett. Vol. 38*, Issue 17, pp. 3205–3207, vol. 38, no. 17, pp. 3205–3207, Sep. 2013.
- [11] C. A. Trujillo and J. Garcia-Sucerquia, "Automatic method for focusing biological specimens in digital lensless holographic microscopy," *Opt. Lett. Vol. 39*, Issue 9, pp. 2569–2572, vol. 39, no. 9, pp. 2569–2572, May 2014.
- [12] S. O. Isikman, W. Bishara, O. Mudanyali, T.-W. Su, D. Tseng, and A. Ozcan, "Lensfree Computational Microscopy Tools for On-Chip Imaging of Biochips," 2013, pp. 71–96.
- [13] W. Xu, M. H. Jericho, I. A. Meinertzhagen, and H. J. Kreuzer, "Digital in-line holography for biological applications," *Proc. Natl. Acad. Sci. U. S. A.*, vol. 98, no. 20, pp. 11301–11305, 2001.
- [14] S. K. K. Jericho, J. Garcia-Sucerquia, W. Xu, M. H. H. Jericho, and H. J. J. Kreuzer, "Submersible digital in-line holographic microscope," *Rev. Sci. Instrum.*, vol. 77, no. 4, pp. 43706–43710, 2006.
- [15] B. Bai, H. Wang, T. Liu, Y. Rivenson, J. FitzGerald, and A. Ozcan, "Pathological crystal imaging with single-shot computational polarized light microscopy," *Journal of Biophotonics*. 2020.
- [16] H. Zhu, S. O. Isikman, O. Mudanyali, A. Greenbaum, and A. Ozcan, "Optical imaging techniques for point-of-care diagnostics," *Lab Chip*, vol. 13, no. 1, pp. 51–67, Jan. 2013.
- [17] W. Xu, M. H. Jericho, I. A. Meinertzhagen, and H. J. Kreuzer, "Digital in-line holography for biological applications," *Proc. Natl. Acad. Sci. U. S. A.*, vol. 98, no. 20, p. 11301, Sep. 2001.
- [18] S. Seo *et al.*, "High-throughput lens-free blood analysis on a chip," *Anal. Chem.*, vol. 82, no. 11, pp. 4621–4627, Jun. 2010.
- [19] T. W. Su, I. Choi, J. Feng, K. Huang, E. McLeod, and A. Ozcan, "Sperm Trajectories Form Chiral Ribbons," *Sci. Reports* 2013 31, vol. 3, no. 1, pp. 1–8, Apr. 2013.
- [20] B. Sunarko, Djuniadi, M. Bottema, N. Iksan, K. A. N. Hudaya, and M. S. Hanif, "Red blood cell classification on thin blood smear images for malaria diagnosis," in *Journal of Physics: Conference Series*, 2020, vol. 1444, no. 1.
- [21] O. Mudanyali, C. Oztoprak, D. Tseng, A. Erlinger, and A. Ozcan, "Detection of waterborne parasites using field-portable and cost-effective lensfree microscopy," *Lab Chip*, vol. 10, no. 18, pp. 2419–2423, Aug. 2010.
- [22] M. J. Lopera and C. Trujillo, "Linear diattenuation imaging of biological samples with digital lensless holographic microscopy," *Appl. Opt.*, vol. 61, no. 5, p. B77, Feb. 2022.
- [23] V. Micó and Z. Zalevsky, "Superresolved digital in-line holographic microscopy for high-resolution lensless biological imaging," <https://doi.org/10.1117/1.3481142>, vol. 15, no. 4, p. 046027, Jul. 2010.
- [24] B. Khademhosseini, G. Biener, I. Sencan, and A. Ozcan, "Lensless on-chip color imaging using nano-structured surfaces and compressive decoding," in *2011 Conference on Lasers and Electro-Optics: Laser Science to Photonic Applications, CLEO 2011*, 2011, p. CTuM1.
- [25] F. Perraut, M. Doménès, H. Grateau, and Q. Josso, "Achieving magnification smaller than 1 in lensless microscopy by illumination with a convergent wavefront," *Opt. Lett.*, vol. 41, no. 22, p. 5326, Nov. 2016.
- [26] S. O. Isikman, I. Sencan, O. Mudanyali, W. Bishara, C. Oztoprak, and A. Ozcan, "Wide field-of-view lensless imaging of *Caenorhabditis Elegans* on a chip," in *Optics InfoBase Conference Papers*, 2010, p. AMC5.
- [27] G. Huang, H. Jiang, K. Matthews, and P. Wilford, "Lensless imaging by compressive sensing," *2013 IEEE Int. Conf. Image Process. ICIP 2013 - Proc.*, pp. 2101–2105, 2013.
- [28] A. Ozcan and E. McLeod, "Lensless Imaging and Sensing," *Annu. Rev. Biomed. Eng.*, vol. 18, pp. 77–102,

2016.

[29] Y. Zhang *et al.*, “Wide-field imaging of birefringent synovial fluid crystals using lens-free polarized microscopy for gout diagnosis OPEN,” *Nat. Publ. Gr.*, 2016.

[30] U. A. Gurkan *et al.*, “Miniaturized lensless imaging systems for cell and microorganism visualization in point-of-care testing,” *Biotechnol. J.*, vol. 6, no. 2, pp. 138–149, Feb. 2011.

[31] D. Tseng *et al.*, “Lensfree microscopy on a cellphone,” *Lab Chip*, vol. 10, no. 14, pp. 1787–1792, 2010.

[32] C. Trujillo and M. J. Lopera, “Portable cellphone-based digital lensless holographic microscope,” *Front. Opt. + Laser Sci. 2021 (2021), Pap. JTh5A.14*, p. JTh5A.14, Nov. 2021.

[33] L. Repetto, E. Piano, and C. Pontiggia, “Lensless digital holographic microscope with light-emitting diode illumination,” *Opt. Lett.*, vol. 29, no. 10, p. 100, 2004.

[34] C. Buitrago-Duque, E. Zora-Guzmán, H. Tobon-Maya, J. Garcia-Sucerquia, and S. Zapata-Valencia, “Open-source, cost-effective, portable, 3D-printed digital lensless holographic microscope,” *Appl. Opt. Vol. 60, Issue 4, pp. A205-A214*, vol. 60, no. 4, pp. A205–A214, Feb. 2021.

[35] O. Mudanyali *et al.*, “Compact, light-weight and cost-effective microscope based on lensless incoherent holography for telemedicine applications,” *Lab Chip*, vol. 10, no. 11, pp. 1417–1428, May 2010.

[36] T.-W. Su, S. O. Isikman, W. Bishara, D. Tseng, A. Erlinger, and A. Ozcan, “Multi-angle lensless digital holography for depth resolved imaging on a chip,” *Opt. Express*, vol. 18, no. 9, p. 9690, Apr. 2010.

[37] B. Perucho and V. Micó, “Wavefront holoscopy: application of digital in-line holography for the inspection of engraved marks in progressive addition lenses,” *J. Biomed. Opt.*, vol. 19, no. 1, p. 016017, Jan. 2014.

[38] Z. Frenzt, S. Kuehn, and D. Hekstra, “Microbial population dynamics by digital in-line holographic microscopy ARTICLES YOU MAY BE INTERESTED IN,” *Rev. Sci. Instrum.*, vol. 81, p. 84301, 2010.

[39] B. Patiño-Jurado, J. Garcia-Sucerquia, and J. F. Botero-Cadavid, “Cone-shaped optical fiber tip for cost-effective digital lensless holographic microscopy,” *Appl. Opt. Vol. 59, Issue 10, pp. 2969-2975*, vol. 59, no. 10, pp. 2969–2975, Apr. 2020.

[40] M. Sanz, M. Trusiak, J. García, and V. Micó, “Variable zoom digital in-line holographic microscopy,” *Opt. Lasers Eng.*, vol. 127, p. 105939, Apr. 2020.

[41] M. J. Lopera and C. Trujillo, “Holographic point source for digital lensless holographic microscopy,” *Opt. Lett.*, vol. 47, no. 11, p. 2862, 2022.

[42] D. R. Shafer, F. Duerr, H. Ottevaere, H. Thienpont, and Y. Nie, “Automated freeform imaging system design with generalized ray tracing and simultaneous multi-surface analytic calculation,” *Opt. Express, Vol. 29, Issue 11, pp. 17227-17245*, vol. 29, no. 11, pp. 17227–17245, May 2021.

[43] T. Blachowicz, G. Ehrmann, and A. Ehrmann, “Optical elements from 3D printed polymers,” *E-Polymers*, vol. 21, no. 1, pp. 549–565, Jan. 2021.

[44] F. Duerr, Y. Nie, and H. Thienpont, “Potential Benefits of Freeform Optics in On-Axis Imaging Applications,” 2015.

[45] L. Feng *et al.*, “Design of a compact spectrometer with large field of view based on freeform surface,” *Opt. Commun.*, vol. 444, pp. 81–86, Aug. 2019.

[46] J. Reimers, A. Bauer, K. P. Thompson, and J. P. Rolland, “Freeform spectrometer enabling increased compactness,” *Light Sci. Appl. 2017 67*, vol. 6, no. 7, pp. e17026–e17026, Feb. 2017.

[47] A. Madrid-Sánchez, F. Duerr, Y. Nie, H. Thienpont, and H. Ottevaere, “Freeform optics design method for illumination and laser beam shaping enabled by least squares and surface optimization,” *Optik (Stuttg.)*, p. 169941, Sep. 2022.

[48] D. Cheng *et al.*, “Design and manufacture AR head-mounted displays: A review and outlook,” *Light Adv. Manuf.*, vol. 2, no. 3, pp. 350–369, Sep. 2021.

[49] P. Langehanenberg, G. von Bally, and B. Kemper, “Autofocusing in digital holographic microscopy,” *3D Res. 2011 21*, vol. 2, no. 1, pp. 1–11, Nov. 2011.

[50] C. S. Vikram and M. L. Billet, “Optimizing image-to-background irradiance ratio in far-field in-line holography,” *Appl. Opt. Vol. 23, Issue 12, pp. 1995-1998*, vol. 23, no. 12, pp. 1995–1998, Jun. 1984.

[51] A. S. Amoah, G. Vdovin, H. Gong, M. Verhaegen, T. E. Agbana, and V. Bezzubik, “Aliasing, coherence, and resolution in a lensless holographic microscope,” *Opt. Lett. Vol. 42, Issue 12, pp. 2271-2274*, vol. 42, no. 12, pp. 2271–2274, Jun. 2017.

[52] J. Garcia-Sucerquia, “RGB digital lensless holographic microscopy,” *8th Iberoam. Opt. Meet. 11th Lat. Am. Meet. Opt. Lasers, Appl.*, vol. 8785, p. 878572, Nov. 2013.

[53] J. W. Goodman, “Wiley: Statistical Optics,” p. 544, 2015.

[54] O. Svelto *et al.*, “Lasers and coherent light sources,” in *Springer Handbook of Lasers and Optics*, Springer Berlin Heidelberg, 2012, pp. 641–1046.

[55] Z. LLC, “Zemax manual.” 2022.

[56] M. J. Lopera and C. Trujillo, “Holographic optical element for digital lensless holographic microscopy’s illumination,” 2022.

[57] J. W. Goodman, *Introduction to Fourier Optics*. Greenwood Village: Roberst & Company Publishers, 2005.

[58] C. Trujillo, P. Piedrahita-Quintero, and J. Garcia-Sucerquia, “Digital lensless holographic microscopy: numerical simulation and reconstruction with ImageJ,” *Appl. Opt.*, vol. 59, no. 19, p. 5788, Jul. 2020.

[59] S. Obando-Vásquez and C. Trujillo, “Computationally efficient phase aberration compensation method for digital holographic microscopy of biological samples,” *Biophotonics Congr. 2021 (2021), Pap. JW1A.19*,

526
527
528
529
530
531
532
533

- p. JW1A.19, Apr. 2021.
- [60] C. Trujillo, R. Castañeda, P. Piedrahita-Quintero, and J. Garcia-Sucerquia, "Automatic full compensation of quantitative phase imaging in off-axis digital holographic microscopy," *Appl. Opt.*, vol. 55, no. 36, p. 10299, Dec. 2016.
- [61] J. M. Bioucas-Dias and G. Valadão, "Phase unwrapping via graph cuts," in *Lecture Notes in Computer Science*, 2005, vol. 3522, no. I, pp. 360–367.

September 27th, 2022

Medellín, Colombia

James Leger,
Editor-in-Chief, Optics Express,
University of Minnesota, USA

Dear Prof. Dr. James Leger,

We express our enthusiasm in submitting to Optics Express our manuscript "**Freeform lens-based illumination source for digital lensless holographic microscopy**". This article meets all the requirements of the instructions for authors of the Optics Express Journal.

We certify the originality of this work and the exclusivity of its submission to this journal. The main contribution of this work is that we propose a cost-effective illumination system for digital lensless holographic microscopy (DLHM) by using freeform optics. Experimental and simulation results show that our system surpasses conventional drawbacks, such as mechanical instability and the need for bulky illumination setups, thus easing the path for robust and miniaturized DLHM implementations. Our system will be beneficial for fieldwork applications which is one of the primary purposes of DLHM. We believe this work is of particular interest to the audience of Optics Express as a top-ranking journal in this area.

Finally, to facilitate the review process, we kindly suggest the following list of potential reviewers:

Prof. Dr. Maciej Trusiak, Warsaw University of Technology, Poland.
(maciej.trusiak@pw.edu.pl)

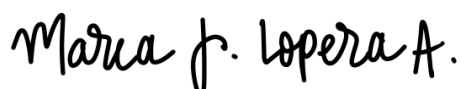
Prof. Dr. Euan McLeod, University of Arizona, USA, (euamc@optics.arizona.edu)

Dr. Maria Antonietta Ferrara, Institute for Microelectronic and Microsystems, Italy,
(antonella.ferrara@na.isasi.cnr.it)

Prof. Dr. Allen Yi, The Ohio State University, USA, (yi.71@osu.edu)

Prof. Dr. Daewook Kim, College of Optical Sciences, University of Arizona, USA,
(dkim@optics.arizona.edu)

Sincerely,



Maria Josef Lopera-Acosta

MSc. candidate in Applied Physics at Universidad EAFIT.
EAFIT research assistant.

FocusNET: An autofocusing learning-based model for digital lensless holographic microscopy

Manuel Montoya^{a,*}, Maria J. Lopera^a, Alejandra Gómez-Ramírez^b, Carlos Buitrago-Duque^b, Jorge García-Sucerquia^b and Carlos Trujillo^a

^aApplied optics group, School of Applied Science and Engineering, Universidad EAFIT, Medellín, Colombia

^bUniversidad Nacional de Colombia sede Medellín, School of Physics, A.A: 3840-Medellín-050034, Colombia

*mmonto95@eafit.edu.co

Abstract

This paper reports a convolutional neural network (CNN) – based regression model, called FocusNET, to predict the precise reconstruction distance of raw holograms in Digital Lensless Holographic Microscopy (DLHM). This proposal provides a physical-mathematical formulation to extend its use to different DLHM setups independently of the training dataset recording optical and geometrical conditions. The proposal results for holograms of different samples recorded with different setups are reported. Additionally, a comparison between FocusNET and conventional autofocusing methods in terms of processing times and accuracy is provided. Although the proposed method predicts reconstruction distances with a $\sim 60\mu\text{m}$ error, accurate information about the samples is still retrieved, reducing processing times of conventional stack reconstruction methods by ~ 600 times for single hologram processing and ~ 1200 times for holograms batches. The training and validation datasets, and the code implementations, are hosted on a public GitHub repository that can be freely accessed using the following link: <https://github.com/mmonto95/focusnet> [1].

© 2017 Elsevier Inc. All rights reserved.

Keywords: Machine Learning, Autofocusing; Lensfree microscopy, DLHM

1. Introduction

Digital Lensless Holographic Microscopy (DLHM) is a simple imaging technique that uses computational methods to retrieve the complex wavefield information of light scattered by micrometer samples[2]. DLHM is based upon in-line Gabor holography with spherical illumination[3,4]. Therefore, its simplicity can be summarized in its requirements: a digital sensor, the sample to be studied, and a divergent spherical wavefront source. This microscopy technique allows the retrieval of amplitude and phase information of the object by numerically backpropagating the recorded hologram to an accurate reconstruction distance[5]. DLHM allows non-invasive and label-free imaging, which has propelled its study and research around biomedical applications, providing polarization sensitivity[6], *in vivo* analysis [4,7], and disease diagnosing [7,8], among others.

A significant DLHM challenge is determining the samples' exact location within the inspection volume without any extended procedure[9]. Although a DLHM hologram provides plane-by-plane information of the said volume, there is no straightforward way to establish the in-focus reconstruction plane of the studied object[10]. Autofocusing methods have been proposed mainly in Digital Holography (DH) and conventional Digital Holographic Microscopy (DHM) to overcome this issue [9,11,12]. The Dubois metric is one of the most referenced methods in this regard, consisting of a pixel-wise summation of the amplitude module of each reconstructed hologram in the inspection volume[13]. As this one, many other proposals can be encountered in the literature to address this issue in DHM [9,10,14]. The application of these proposals has allowed flow analysis [15], tracking of living cells [16], and living cell analysis [17], among other high-impact applications [18]. Although highly effective, all these methods require

hundreds, and sometimes thousands, of sequential numerical reconstructions to provide accurate in-focus reconstruction distances. Thus, conventional methods are computationally demanding and time-consuming[19].

Beyond being computationally demanding, conventional autofocusing proposals fail for DLHM holograms since they do not consider this technique's illumination source wavefront sphericity[10,20]. In [14,20], the authors developed an autofocusing method based on finding the reconstruction plane in which the smallest area around the object to be focused encloses a given amount of irradiance. For each reconstruction plane, the enclosed irradiance is weighted by the inverse of the spherical illumination radius at that plane. The proposal successfully autofocuses intricate inner-structure samples at the expense of requiring high computational complexity preventing its implementation for *in vivo* applications [14].

Deep learning-based methods are powerful tools for solving computer vision problems and for image analysis [21,22]. These methods provide promising strategies to obtain the in-focus reconstruction distance directly from the hologram without requiring several back-propagation operations. Some learning-based proposals can be encountered in holographic imaging to solve the autofocusing problem. For instance, T. Shimobaba *et. al.*[23] proposed a CNN-based regression to automatically focus DH holograms with millimeter precision directly from the power spectrum of the holograms. Rembo et al. reported an autofocusing proposal for DH using a CNN-based classification model by splitting the reconstruction distances into categories [24]. The same authors later reported a CNN-based regression to directly predict the reconstruction distance from the hologram [19]. These deep learning-based models have been implemented and tested only for digital holograms of macroscopic objects, and, up to the authors' best knowledge, these methods have not been applied yet to DLHM.

This paper proposes a convolutional neural network (CNN) model called FocusNET to autofocus raw DLHM holograms. Directly from the hologram, the model uses a regression strategy to predict the in-focus reconstruction distance, thus the object's location within the inspection volume. After describing the DLHM fundamentals and the proposed method in detail, a validation of its accuracy after proper training is presented. This validation evaluates the FocusNET-yielded intensity/phase reconstructions for holograms in the test dataset, and another acquired with different geometrical and optical parameters. For the latter case, a physical-mathematical formulation is provided using the scalar diffraction integral that describes the reconstruction procedure in DLHM to extend the use of FocusNet to DLHM holograms with arbitrary recording conditions. Finally, the method performance is contrasted against conventional methods considering the computation times to reach accurate in-focus reconstruction distances[8]. Experimental results show that FocusNET predicts the object's in-focus reconstruction distance directly from DLHM holograms without any numerical reconstructions at remarkably reduced processing times.

2. Digital Lensless Holographic Microscopy

As previously mentioned, DLHM only requires a spherical wavefront source, a sample, and a digital sensor [4]. The sample is placed after the illumination source to produce a magnified diffraction pattern of the specimen at the sensor plane. Fig. 1 shows a basic DLHM setup.

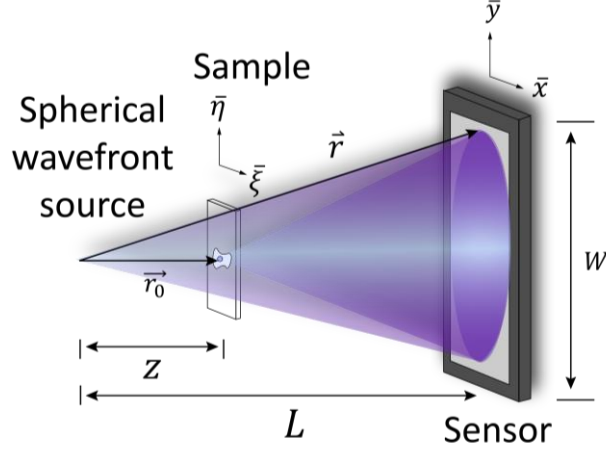


Fig. 1. Digital Lensless Holographic Microscopy (DLHM) setup.

To mathematically describe the DLHM hologram, consider that the sample transmittance $S(\vec{r}_0)$, placed at a distance z from the point source, is illuminated by a diverging spherical wavefront $\exp[ik\vec{r}] / |\vec{r}|$. The diffracted wavefield is magnified by free-space propagation until it reaches the digital sensor at a distance L from the point source. Vectors $\vec{r}_0 = (\xi, \eta, z)$ and $\vec{r} = (x, y, L)$ denote locations at the sensor and camera planes, respectively. The description of the complex-valued intensity that reaches the sensor is given by the Rayleigh-Sommerfeld diffraction formula given by Eq. (1) [25,26].

$$U(\vec{r}) = \int_{sample} S(\vec{r}_0) \frac{\exp[ik\vec{r}_0]}{|\vec{r}_0|} \frac{\exp[ik(\vec{r} - \vec{r}_0)]}{|\vec{r} - \vec{r}_0|} d\vec{r}_0 . \quad (1)$$

Then, the intensity distribution recorded at the digital plane, known as the DLHM hologram, is described by Eq. (2),

$$I(\vec{r}) = U(\vec{r}) U^*(\vec{r}). \quad (2)$$

The information of the sample $S(\vec{r}_0)$ is later retrieved by backpropagating the hologram with a converging spherical wavefront $\exp[ik\vec{r}] / |\vec{r}|$, which is the complex conjugate of the illumination wavefront used during recording. This diffraction process can be numerically described through a scalar diffraction formula; the sample's information is found via Eq. (3).

$$S(\vec{r}_0) = \int_{sample} I(\vec{r}) \frac{\exp[-ik\vec{r}]}{|\vec{r}|} \frac{\exp[-ik(\vec{r} - \vec{r}_0)]}{|\vec{r} - \vec{r}_0|} d\vec{r} . \quad (3)$$

From Eq. (3), the complex-valued optical field of the sample $S(\vec{r}_0)$ is recovered, and its amplitude $|S(\vec{r}_0)|$, intensity $S(\vec{r}_0)S^*(\vec{r}_0)$ or phase $\phi(\vec{r}_0) = \arctan(\text{Im}[S(\vec{r}_0)]/\text{Re}[S(\vec{r}_0)])$ can be retrieved [27,28]. The resolution of the system is defined by its numerical aperture (NA), which is limited by several factors [29]. If the illumination source degree of coherence and sampling conditions are fulfilled, the numerical aperture of the DLHM technique is limited by the

divergence of the wavefront illumination; therefore, the NA for DLHM is defined as follows [30],

$$NA = n \frac{W}{2\sqrt{\left(\frac{W}{2}\right)^2 + (L-z)^2}}. \quad (4)$$

Eq. (4) is valid as long as the sensor is fully illuminated. The lateral δx and axial δz resolutions can be approximated with the given expression for the numerical apertures as shown in equations (5) and (6) [2,28].

$$\delta x \geq \frac{\lambda}{2NA}. \quad (5)$$

$$\delta z \cong \frac{\lambda}{2NA^2}. \quad (6)$$

3. FocusNET

3.1. DLHM training dataset

A setup like the one presented in Fig. 1 has been implemented to record the DLHM dataset to train and test FocusNET. A laser source illumination (632.8 nm He-Ne) is expanded and later focused by an aspheric lens with a diameter of 6.33 mm and a numerical aperture of 0.67. A Panasonic MN34230 camera is used to record the holograms; the sensor width is 13.3 mm with a native pixel pitch of 3.8 μm . The holograms are rescaled, changing the effective pixel pitch to 12.99 μm . The source-to-sample distance L is fixed to 18.8129 mm. The number of recorded holograms for each reconstruction distance z is presented in Fig. 2. Number of DLHM recorded holograms for each reconstruction distance z in the experimental dataset. These experimentally measured distances range from 0.3 mm to 4.1 mm.

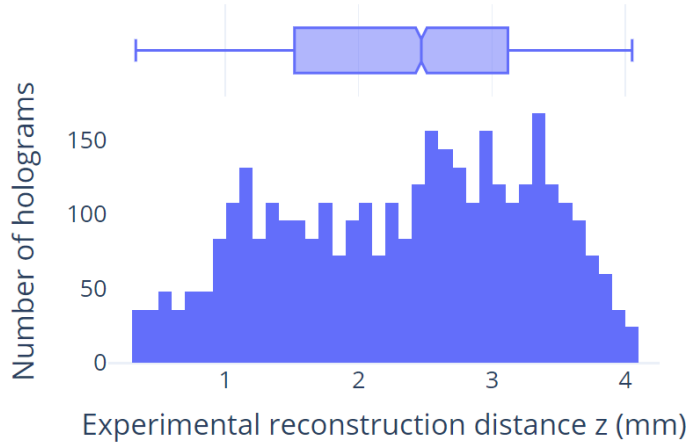


Fig. 2. Number of DLHM recorded holograms for each reconstruction distance z in the experimental dataset.

DLHM holograms with numerical apertures ranging from 0.34 to 0.41 have been recorded. Thus, lateral resolutions from 0.77 μm to 0.93 μm and axial resolutions between 3.8 μm and 5.5 μm are attained. A total of 3540 holograms have been acquired at different locations of the sample. A Vernier micrometer screw is used to allocate the sample; the uncertainty of the given measurement is $\pm 1 \mu\text{m}$. The position given by the screw is used as the ground truth reconstruction distance in this dataset. Nevertheless, these values do not always yield fully in-focus reconstructions: the difference between the experimental and numerical reconstruction distances can be increased by the inaccurate measurement of the other geometrical parameters during recording and by the fact that the numerical propagator

assumes ideal conditions not perfectly met in experimental conditions [31]. The samples used to record the dataset holograms include an optical fiber, plastic circles, a fly's leg, a leaf, a skeletal muscle, a spirogyra, a honeybee wing, epithelial cheek cells, volvox algae, and worm eggs. Fig. 3 shows four examples of holograms in the DLHM dataset.

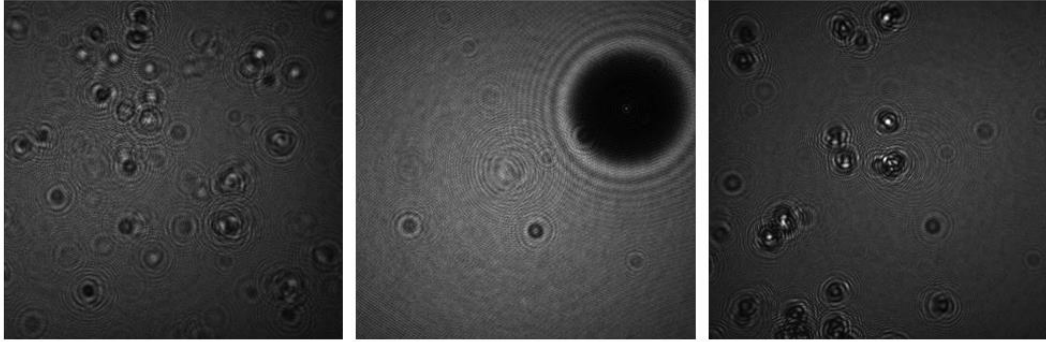


Fig. 3. Four hologram examples in the DLHM dataset.

3.2. FocusNET architecture

Convolutional Neural Networks (CNN) have played a major role in the development of computer vision and image processing [32] due to their ability to subtract features and learn abstract representations from a given set of images. These models have shown their capabilities in various recognition, classification, and segmentation tasks [21,22]. CNNs are an extension of the multilayer neural network [33], thus, their structure is typically a sequence of convolutional layers and filters, followed by one or more fully connected layers [22]. This architecture has the advantages of being shift, scale, and distortion invariant: these properties make CNNs suitable for image processing solutions [34].

Following [19,24], the proposed learning-based model has the architecture presented in Fig. 5. The input layer is composed of a single channel representing the raw DLHM hologram with 8-bit intensity values. After this, a resizing layer is added. The best model's accuracy is obtained when the images are resized to 256x256 due to the available training data: models with more parameters are expected to be more data-hungry[34]. This matter will be analyzed in section 3.3. After this step, a data augmentation layer is added; this layer randomly rotates the hologram by 0°, 90°, 180°, or 270°, helping reduce overfitting. The following preprocessing layer adds a second channel, which represents the amplitude of the Fourier transform of the resized hologram. This layer plays a critical role in increasing the model's generalization, thus further reducing overfitting, as demonstrated by [23] and validated during the experiments in this proposal. Then, the two-channel layer is fed to the convolutional backbone, composed of five convolutional blocks, which is the feature extractor of the model. In this backbone, the model learns the underlying characteristics of the holograms, which will then be used to perform the autofocus estimation. This convolutional backbone is critical as a minimal change in its structure will significantly diminish the model's performance. Each convolutional block includes a convolutional layer, followed by batch normalization and max pooling layers. As the network goes forward inside the convolutional backbone, the number of filters increases while the transformed image size decreases. Specifically, the first convolutional layer starts with eight neurons multiplied by a size factor that controls the final size of the model in terms of trainable parameters, and each subsequent layer doubles the neurons until reaching the regression head. The transformed data is fed to the regression head after being processed by a dropout layer and the flatten layer. The regression head includes two fully connected layers and an output layer with only one neuron. The *swish* activation function, an improvement of the very popular ReLU activation function [35], is used in all the network layers except for the output layer, which has a linear activation function. The Adam optimizer is used as the optimization algorithm with a variable learning rate. For the best performance models, the training took 500 epochs, with the learning rate

starting at a value of 0.001, decreasing by a factor of 2 every 100 epochs, and then decreasing exponentially after epoch 450. Fig. 4 shows the variation in the learning rate as the number of epochs increases. This variation of the learning rate proved to be very effective in improving both the model's flexibility and generalization.

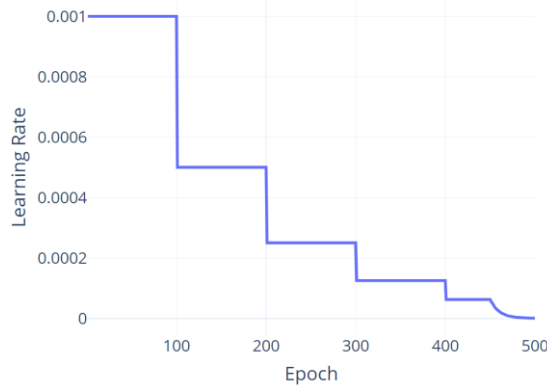


Fig. 4. Variation in the learning rate vs. epochs.

To train FocusNET, the previously described DLHM dataset has been used. The loss function used for optimization is the *mean squared error (MSE)*, which is given by the average of squared errors in the estimation. This error is the difference between the predicted reconstruction distance z_{FN} and the corresponding ground truth value z ; the loss function is given by Eq. (7).

$$MSE(z, z_{FN}) = \frac{1}{N} \sum_{i=1}^N (z - z_{FN})^2. \quad (7)$$

In Eq. (5), N is the total number of holograms processed in each batch. In this proposal, a batch size $N = 64$ has been set for training.

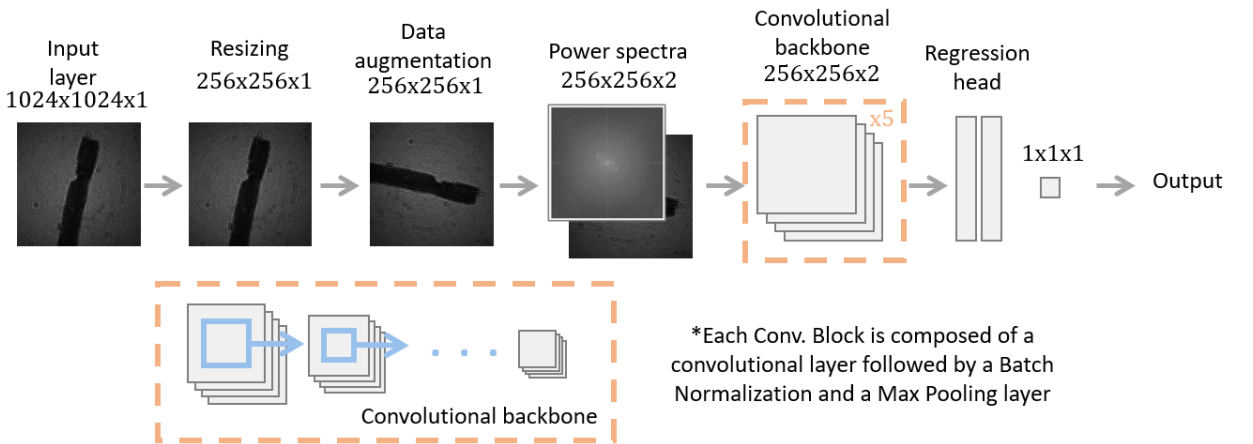


Fig. 5. FocusNET architecture.

3.3. Evaluation metrics and training details

Two metrics have been used to evaluate the model's performance: the mean squared error (MSE) and the mean absolute error (MAE). The MAE reports the distance error between the model estimation and the ground truth reconstruction distances, providing a physical measurement of the estimation error, in this case, in millimeters.

$$MAE(z, z_{FZ}) = \frac{1}{N} \sum_{i=1}^N |z - z_{FN}|. \quad (8)$$

The model has been evaluated using the typical train-validation approach. The dataset is randomly split into two subsets with a ratio of 80:20 for training and validation. The best performing model is achieved using the hyperparameters presented in Table 1. Except for the resizing, all those hyperparameter values are adjusted empirically by evaluating the model performance with the MAE and MSE metrics on an epoch-by-epoch basis. The implemented method consists of a grid search with variations in the hyperparameter values, starting with the less-complex (fewer parameters) combinations and choosing the parameters to tune for the next iteration based on some characteristics of the training process, such as convergence rate, stability, overfitting, and best and final values found for the metrics in the training and validation datasets. See Supplementary 1 for further details. The best values for the model hyperparameters are presented in Table 1. "Changing Epoch" refers to the epoch when the exponential decay of the learning rate starts, and "Unchanging Period" refers to the number of epochs where the learning rate remains unaltered before halving its value.

Table 1. Best values found for the model hyperparameters

Hyperparameter	Value
Training Epochs	500
Batch Size	64
Initial Learning Rate	0.001
Changing Epoch	450
Unchanging Period	100
Decay	0.1
Size Factor	4
Dropout Rate	0.2
Distance Unit	mm
Resizing	256x256
Fourier Transform Feature	Amplitude

Since the purpose of FocusNET is to predict the accurate in-focus reconstruction distance without high inference times, the resizing layer is very important. As the size of the trained model affects this inference time, it becomes an important factor to consider when selecting the final best performance model. Fig. 6, panel (a) presents the model's prediction time as its size increases on a batch of 50 holograms. The variation of the MAE metric as a function of different model sizes is presented in Fig. 6, panel (b). For smaller models, overfitting is more likely to occur. Conversely, no significant improvement of the metric is achieved for larger models. From these results, choosing the 256x256 model (third from left to right) is adequate, as it has the lowest combination of training and validation MAE values. The model using this resizing presents a better generalization while reducing inference time.

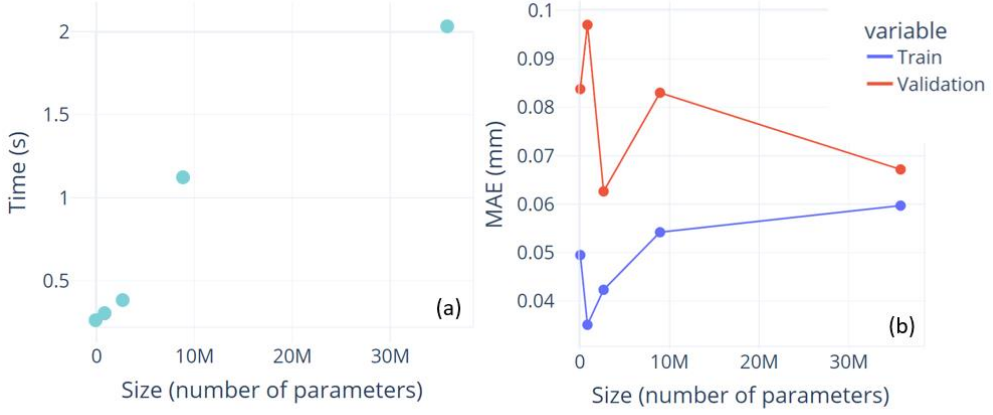


Fig. 6. Inference times and errors (MAE) of FocusNet at different model sizes.

All the models have been trained using the Apollo high-performance computer provided by Universidad EAFIT [35]. The acceleration node is powered by three NVIDIA V100 GPUs of 32GB each [36]. The training time varied from 2 hours for the less-complex models with fewer epochs to 16 hours for the largest models. FocusNET has been trained with the hyperparameters presented in Table 1; the training history displayed in Fig. 7. Panel (a) presents the training history from 0 to 100 epochs, and panel (b) from 100 to 500 epochs. This history shows a healthy training process that presents a higher variance at the beginning and then progressively stabilizes with each iteration. After 100 epochs, the metrics for training continue decreasing, but the ones for validation stop decreasing, causing the series to diverge. At that point, the training process is stopped to avoid overfitting. The final results for MSE and MAE metrics are presented in Table 2.

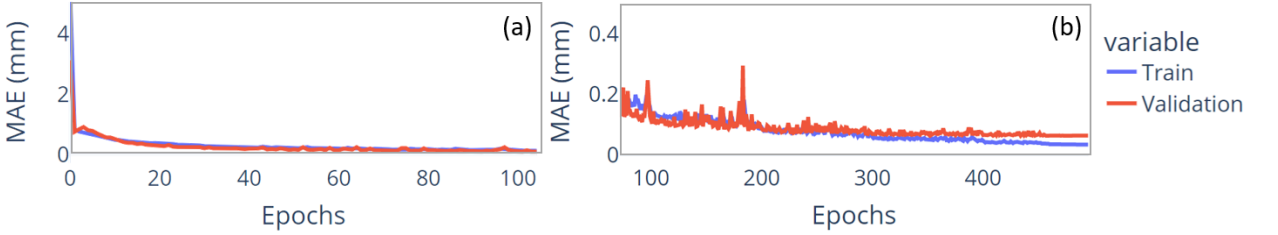


Fig. 7. Training history for the best FocusNET model.

Table 2. Quality metrics of FocusNET.

Metric	Training	Validation
MSE	0.0019	0.0070
MAE (mm)	0.034	0.064

4. Results

4.1. Validation: test dataset

Four random images are initially selected from the validation dataset and then reconstructed based on the FocusNET predicted reconstruction distances. The intensity information of these samples is presented in Fig. 8. On average, the reconstruction distance error for these holograms is $64\mu\text{m}$. This error value is expected from the obtained training MAE. The error represents around ten times the axial resolution of the system. Although this error is relatively high, the predicted reconstruction distance allows the proper observation of details of the sample, as can be observed in the zoomed-in areas of Fig. 8.

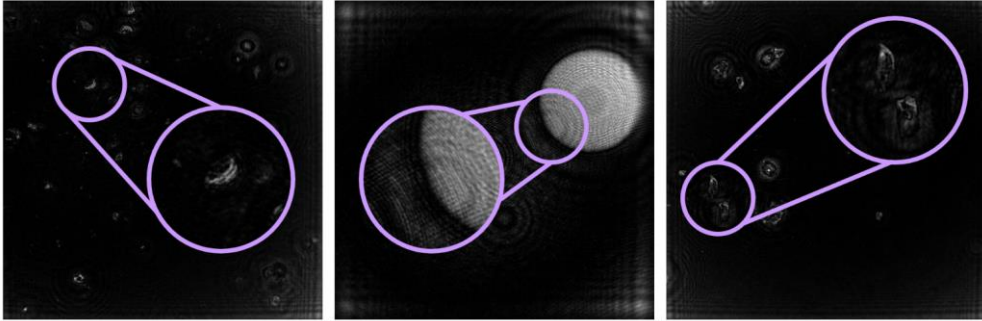


Fig. 8. Intensity reconstructions of four random holograms of the validation dataset with the FocusNET predicted reconstruction distances.

Two random holograms were picked from the validation dataset to study how the reconstruction distance error of FocusNet affects the quality of the retrieved images. Table 3, Fig.9 and Fig. 10 present the results.

Table 3. FocusNET prediction for two random holograms.

Sample	Prediction time (s)	FocusNET distance (mm)	Ground truth distance (mm)	Error (μm)
Optical fiber	0.1	2.0554	2.1000	44.6
Fly's leg	0.1	2.308	2.38	72

Fig. 9 shows the intensity reconstruction for the optical fiber sample with the reconstruction distance predicted by FocusNET [panel (a)] and using the ground truth reconstruction distance [panel (b)]. In the zoomed-in area of the FocusNET prediction, one can observe diffraction effects in the edge of the sample due to the focusing distance error (observe the green arrow). These effects are not present in the reconstruction presented in panel (b). For a better comparison, panels (c) and (d) present horizontal (c) and vertical (d) intensity profiles of the optical fiber denoted by the orange for the FocusNET reconstruction and blue for the ground truth reconstruction lines. The FocusNET-yielded reconstruction presents more diffraction effects resulting in a narrower fiber profile. Nevertheless, the measured width of the fiber only differs by six pixels, corresponding to approximately $6\mu\text{m}$ (panel (d)). Also, the background (BG) noise is approximately the same for both reconstructions, and the normalized gradient in the fiber's edge is higher in the ground truth as the edge is sharper than the FocusNET reconstruction.

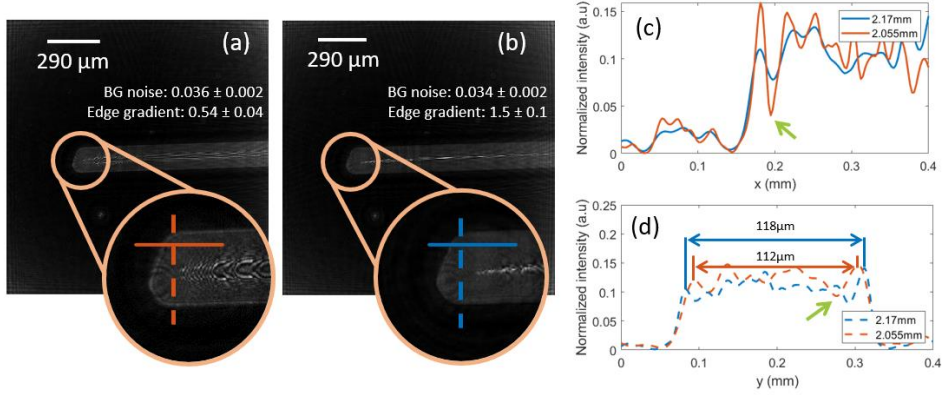


Fig. 10. Intensity reconstruction of the fiber hologram at the FocusNET predicted distance (a) and ground truth reconstruction distance (b). Crossed sections of the fiber reconstruction with the ground truth distance (blue) and the FocusNET distance (red) at x axis (c) and y axis (d).

Fig. 10 presents the intensity reconstruction of a fly's leg hologram with FocusNET reconstruction distance [panel (a)] and with the ground truth distance [panel (b)]. One interesting effect can be observed in this reconstruction: several in-focus planes can be found. The ground truth distance is relative depending on which part of the sample is observed. If the purple area is analyzed, more details of the sample's hairs can be detailed at the FocusNET distance than at the considered ground truth distance (observe orange arrows). The opposite occurs for the green area. More details are observed with the ground truth distance than with the FocusNET-based reconstruction. This result is in concordance with what is stated in [31], the positioning error in autofocusing models is relative to the sample.

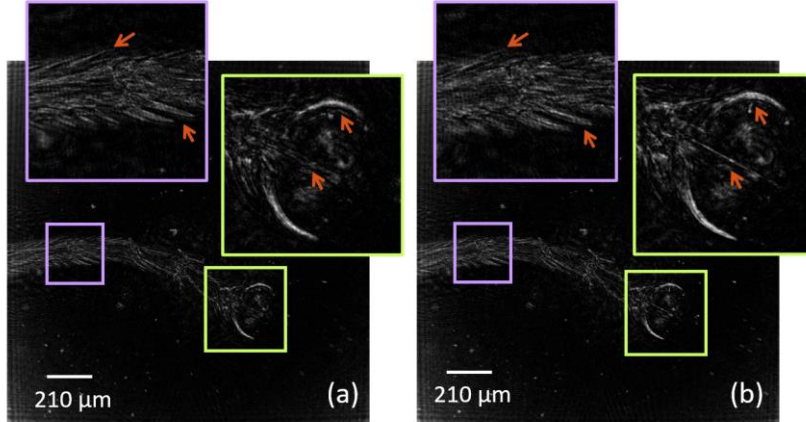


Fig. 9. Intensity reconstruction of the fly's leg hologram at the FocusNET predicted distance (a) and ground truth reconstruction distance (b).

4.2. Validation with holograms acquired with different DLHM setups

FocusNET has been trained with a dataset containing holograms acquired with a single DLHM geometry ($L_{FN} = 18.81 \text{ mm}$, $W_{FN} = 13.3 \text{ mm}$, $k_{FN} = 2\pi/\lambda_{FN} = 9.9 \mu\text{m}^{-1}$). Therefore, the predicted distance z_{FN} corresponds to holograms registered with those geometrical parameters. For instance, considering a hologram I registered with a different DLHM geometry (L, W, k), the recovered information of the sample is given by Eq. (3). But, if the spherical wavefront used for FocusNET is used to reconstruct this hologram, the information of the sample can be found through Eq. (9).

$$S(\vec{r}_{0FN}) = \int_{\text{sample}} I \frac{\exp[-ik_{FN}\vec{r}_{FN}]}{|\vec{r}_{FN}|} \frac{\exp[-ik_{FN}(\vec{r}_{FN} - \vec{r}_{0FN})]}{|\vec{r}_{FN} - \vec{r}_{0FN}|} d\vec{r} . \quad (9)$$

Let us impose that the information of the sample retrieved with the original geometrical recording parameters (\vec{r} and \vec{r}_0) is the same as the one recovered with the FocusNET parameters (\vec{r}_{FN} and \vec{r}_{0FN}). This implies that the magnification of the sample in both geometries is the same.

$$M_{FN} = \frac{L_{FN}}{z_{FN}} = M = \frac{L}{z_i}. \quad (10)$$

From Eq. (10), the reconstruction distance with the actual geometrical DLHM parameters (without considering the illumination wavelength λ) can be found from the FocusNET reconstruction distance.

$$z_i = \frac{L}{L_{FN}} z_{FN}. \quad (11)$$

Moreover, to retrieve the full same sample information, including λ , Eq. (12) must be fulfilled.

$$\frac{\exp[-ik_{FN}\vec{r}_{FN}]}{|\vec{r}_{FN}|} \frac{\exp[-ik_{FN}(\vec{r}_{FN} - \vec{r}_{0FN})]}{|\vec{r}_{FN} - \vec{r}_{0FN}|} = \frac{\exp[-ik\vec{r}]}{|\vec{r}|} \frac{\exp[-ik(\vec{r} - \vec{r}_0)]}{|\vec{r} - \vec{r}_0|}. \quad (12)$$

Since the real and imaginary components of (12) are equal on both sides of the equation, then z of the actual DLHM setup is found, Eq. (13).

$$z = 2L - \frac{\lambda}{\lambda_{FN}} (2L_{FN} - z_i). \quad (13)$$

From this analysis, the following procedure must be followed to obtain the reconstruction distance of a DLHM hologram, regardless of its physical recording parameters.

- i). FocusNET predicts the reconstruction distance z_{FN} .
- ii). To fulfill the magnification assumption, Eq. (11) is applied over the distance found in i), and z_i is computed.
- iii). Then, Eq. (13) must be applied. If the wavelength, $\lambda = \lambda_{FN}$, then this step can be avoided.

A hologram acquired with a different DLHM setup and with a different sample has been studied to validate the latter analysis. The sample contains red blood cells (RBC). The DLHM setup and the reconstruction distance result are displayed in Table 4.

Table 4. FocusNET prediction values for an experimental hologram with different DLHM optical parameters.

Sample	$L(\text{mm})$	$W(\text{mm})$	$\lambda(\text{nm})$	Ground truth z (mm)	NA	FocusNET raw z_{FN} (mm)	FocusNET corrected z (mm)	Error (μm)
Red blood cells	8	4.71	532	0.730	0.31	1.3732	0.7135	16.5

The amplitude and phase reconstructions of the sample are presented in Fig. 11. The error obtained with the corrected FocusNET prediction is $16.5\mu\text{m}$; this error is considerably high compared to the depth of the sample, which is on average $2.5\mu\text{m}$ [8], but it is smaller than the error range reported for FocusNET. Despite the error, the amplitude reconstruction, panel (b) in Fig. 11, allows the identification of the cells and could allow further analysis, such as cell counting [8]. For this sample, the phase map obtained with the FocusNET predicted reconstruction distance also allows the proper visualization of the cells; the phase changes inside the cells allow observing the typical donut-like shape of these specimens, as can be observed in the 3D phase maps of panels (c) and (d).

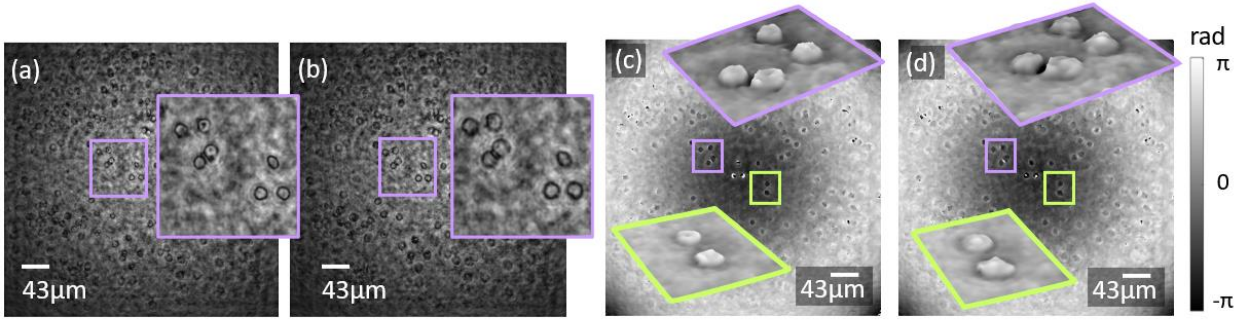


Fig. 11. Amplitude reconstruction of a DLHM hologram. (a) with the ground truth reconstruction distance. (b) With the corrected FocusNET reconstruction distance. Phase map reconstruction of the RBC sample with (c) ground truth distance and (d) corrected FocusNET distance.

4.3. Comparison with conventional autofocusing algorithms

The main advantage of FocusNET is the computing time required to retrieve the proper reconstruction distance, as no numerical reconstructions are needed—changing plane-by-plane reconstruction methods for a one-time kernel-image multiplication significantly reduces computational complexity. Dubois, Gradient-based, Power spectra and variance are the conventional methods to validate the latter assumption. The hologram of the optical fiber presented in Fig. 9 is used for this experiment; the performance of the conventional techniques is presented in Fig. 11.

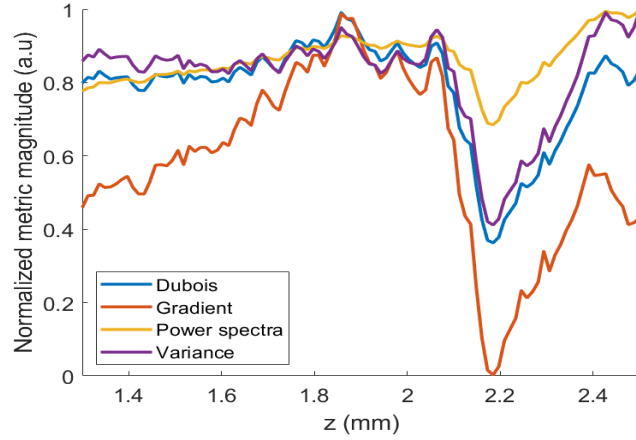


Fig. 12. Performance of the conventional autofocus metrics for the optical fiber DLHM hologram.

The errors and prediction times obtained for the four conventional techniques and FocusNET are presented in Table 5. The step for the stack reconstruction methods is $2\mu\text{m}$. All algorithms run on an intel core i7, 8th gen with 4 CPU cores. As can be observed, the prediction time of FocusNET is about 600 times faster than the average time of the classical metrics, but their accuracy is compared to the axial resolution of the system, providing high-quality reconstructions; meanwhile, the FocusNET error is $44.6\mu\text{m}$.

Table 5. Conventional autofocusing methods and FocusNET computing time and error for the optical fiber hologram.

Method	Error (μm)	Time (s)
Dubois	$4\mu\text{m}$	57.1
Gradient	$6\mu\text{m}$	60.7
Power spectra	$4\mu\text{m}$	69.1
Variance	$10\mu\text{m}$	64.4
FocusNET	$44.6\mu\text{m}$	0.1

If we dive into the video-rate domain, where a series of holograms needs to be processed sequentially in a minimal amount of time, the difference becomes even more prominent. A deep learning-based autofocusing approach can handle batch inference and is highly parallelizable, so the computation time does not increase linearly with the number of inputs, as opposed to the conventional techniques, in which it would be much harder to implement the same level of parallelism. To prove the later, a batch of 10 validation holograms have been tested with FocusNET and with the Dubois metric. To test the Dubois metric with the batch of holograms, a parallelized loop is implemented in MATLAB; each hologram is independently reconstructed for each reconstruction distance. As these processes are not sequential, the computing tasks can be easily split into each CPU core. Both algorithms run in a 4 CPU intel core i7 computer. Table 6 presents the average error obtained and the prediction time required by the methods. The prediction time with FocusNET for a batch of 10 holograms is about 1.200 times faster than the Dubois-based method in a machine without GPU. These values open the possibility of accurately reconstructing in-focus DLHM holograms at video rates. The latter is confirmed when FocusNET is tested using a Mac's M1 chip powered by a GPU unit. In this case, the prediction time for a single hologram decreases to 58 milliseconds, and for a batch of 50 holograms, the prediction time goes down to 0.42 seconds [8.4 milliseconds per single hologram].

Table 6. FocusNET and Dubois autofocusing methods for a batch of ten holograms

Method	Average error (μm)	Total prediction time (s)
Batch Dubois	4 μm	541
Batch FocusNET	60 μm	0.44

5. Conclusions

This paper reports a regression learning-based autofocusing model, FocusNET, to attain the in-focus reconstruction distances of DLHM holograms. The model is built using resizing layers, data augmentation stages, a two-channel input including the spectrum of the raw DLHM holograms, and a convolutional backbone composed of convolutional layers ending in a conventional regression head. The model is trained with DLHM holograms recorded with a specific geometrical setup in which the sample location ranges from 0.3mm to 4.8mm, yielding numerical apertures from 0.34 to 0.41. FocusNET predicts reconstruction distances leading to focused phase and amplitude images of the samples with an error of 60 μm for DLHM holograms of the validation dataset, this error is relative, as some samples may present diverse in-focus planes, as the presented fly’s leg. In general, the errors obtained with the proposed model are significant compared to the axial resolution attained in DLHM; this is partly due to the difference between the measurement provided by the mechanical device used to locate the sample, which is the ground truth to fit the model, and the actual reconstruction distance of the specimens. In future work, we will determine the ground truth reconstruction distance by employing a robust autofocusing technique for DLHM, such as the modified enclosed energy (MEE) method[37]. A physical-mathematical model is also provided to correct the predicted FocusNET reconstruction distance of DLHM holograms acquired at different recording conditions. This strategy is validated with a hologram of a biological sample yielding successful results at the autofocusing task, demonstrating the proposed learning-based method’s generalization to different samples and setups. Compared to conventional autofocusing methods - Dubois, spectrum-based, variance-based, gradient-based - FocusNet is 600 times faster predicting the correct reconstruction distance of single holograms and 1200 times faster for hologram batches without any stack numerical reconstructions. Therefore, FocusNET paves the way to autofocusing video-rate applications of DLHM, facilitating the usability of the technique in motility analysis for microorganism tracking and cell counting, among others.

Acknowledgments

The authors acknowledge supercomputing resources made available by the *Centro de Computación Científica Apolo* at Universidad EAFIT (<http://www.eafit.edu.co/apolo>) to conduct the research reported in this scientific product. M. Montoya, M. J. Lopera, and C. Trujillo acknowledge the support provided by Vicerrectoría de Ciencia, Tecnología e Innovación from Universidad EAFIT.

Funding

Universidad EAFIT under grants: “*Beca de reconocimiento a la investigacion*”, “*Beca de reconocimiento a la excelencia académica*”, and the G8 Medellin Metropolitan Area universities funding.

Data availability

The code implementation, documentation, and holograms used are publicly available on GitHub [1]. The GitHub repository also includes troubleshooting guidelines for the correct use of FocusNET.

Disclosures

The authors declare no conflicts of interest.

References

- [1] Montoya Zuluaga M, Lopera MJ, Trujillo C. FocusNET repository. 2022 n.d. <https://github.com/mmonto95/focusnet> (accessed September 26, 2022).
- [2] Garcia-Sucerquia J, Xu W, Jericho SK, Klages P, Jericho MH, Kreuzer HJ. Digital in-line holographic microscopy. *Appl Opt* 2006;45:836–50. <https://doi.org/10.1364/AO.45.000836>.
- [3] Leith EN, Upatnieks J. Reconstructed Wavefronts and Communication Theory*. *JOSA*, Vol 52, Issue 10, Pp 1123–1130 1962;52:1123–30. <https://doi.org/10.1364/JOSA.52.001123>.
- [4] Kreuzer HJ, Meinertzhagen IA, Jericho MH, Xu W. Digital in-line holography of microspheres. *Appl Opt* Vol 41, Issue 25, Pp 5367–5375 2002;41:5367–75. <https://doi.org/10.1364/AO.41.005367>.
- [5] Ozcan A, McLeod E. Lensless Imaging and Sensing. *Annu Rev Biomed Eng* 2016;18:77–102. <https://doi.org/10.1146/annurev-bioeng-092515-010849>.
- [6] Lopera MJ, Trujillo C. Linear diattenuation imaging of biological samples with digital lensless holographic microscopy. *Appl Opt* 2022;61:B77. <https://doi.org/10.1364/AO.440376>.
- [7] Seo S, Su TW, Tseng DK, Erlinger A, Ozcan A. Lensfree holographic imaging for on-chip cytometry and diagnostics. *Lab Chip* 2009;9:777–87. <https://doi.org/10.1039/b813943a>.
- [8] Seo S, Isikman SO, Sencan I, Mudanyali O, Su TW, Bishara W, et al. High-throughput lens-free blood analysis on a chip. *Anal Chem* 2010;82:4621–7. https://doi.org/10.1021/AC1007915/SUPPL_FILE/AC1007915_SI_001.PDF.
- [9] Langehanenberg P, von Bally G, Kemper B. Autofocusing in digital holographic microscopy. *3D Res* 2011 21 2011;2:1–11. [https://doi.org/10.1007/3DRES.01\(2011\)4](https://doi.org/10.1007/3DRES.01(2011)4).
- [10] Trujillo Anaya CA. Improved-performance digital holographic microscopy 2018.
- [11] Lyu M, Yuan C, Li D, Situ G. Fast autofocusing in digital holography using the magnitude differential. *Appl Opt* 2017;56:F152. <https://doi.org/10.1364/ao.56.00f152>.
- [12] Huang L, Liu T, Yang X, Luo YI, Rivenson Y, Ozcan A. Holographic image reconstruction with phase recovery and autofocusing using recurrent neural networks 2021.
- [13] Yourassowsky C, Schockaert C, Dubois F, Callens N. Focus plane detection criteria in digital holography microscopy by amplitude analysis. *Opt Express*, Vol 14, Issue 13, Pp 5895–5908 2006;14:5895–908. <https://doi.org/10.1364/OE.14.005895>.
- [14] Trujillo C, Garcia-Sucerquia J. Cooperative execution of auto-focusing metrics in digital lensless holographic microscopy for internal-structured samples. *Appl Opt* Vol 56, Issue 21, Pp 5877–5882 2017;56:5877–82. <https://doi.org/10.1364/AO.56.005877>.
- [15] Yourassowsky C, Dubois F, Campbell L, Olson RJ, Sosik HM, Abraham A, et al. High throughput holographic imaging-in-flow for the analysis of a wide plankton size range. *Opt Express*, Vol 22, Issue 6, Pp 6661–6673 2014;22:6661–73. <https://doi.org/10.1364/OE.22.006661>.
- [16] Langehanenberg P, Ivanova L, Bernhardt I, Ketelhut S, Vollmer A, Dirksen D, et al. Automated three-dimensional tracking of living cells by digital holographic microscopy. *J Biomed Opt* 2009;14:014018. <https://doi.org/10.1117/1.3080133>.
- [17] Dirksen D, Droste H, Kemper B, Deleré H, Deiwick M, Scheld HH, et al. Lensless Fourier holography for digital holographic interferometry on biological samples. *Opt Lasers Eng* 2001;36:241–9. [https://doi.org/10.1016/S0143-8166\(01\)00053-7](https://doi.org/10.1016/S0143-8166(01)00053-7).
- [18] Finizio A, Pierattini G, Coppola G, Ferraro P, Nicola S De. Digital holographic microscope with automatic focus tracking by detecting sample displacement in real time. *Opt Lett* Vol 28, Issue 14, Pp 1257–1259 2003;28:1257–9. <https://doi.org/10.1364/OL.28.001257>.
- [19] Lam EY, Ren Z, Xu Z. Learning-based nonparametric autofocusing for digital holography. *Opt* Vol 5, Issue 4, Pp 337–344 2018;5:337–44. <https://doi.org/10.1364/OPTICA.5.000337>.
- [20] Trujillo C, Garcia-Sucerquia J. Comparative analysis of the modified enclosed energy metric for self-focusing holograms from digital lensless holographic microscopy. *Appl Opt* 2015;54:5102.

- <https://doi.org/10.1364/ao.54.005102>.
- [21] Lecun Y, Bengio Y, Hinton G. Deep learning. *Nat* 2015 5217553 2015;521:436–44.
<https://doi.org/10.1038/nature14539>.
 - [22] Krizhevsky A, Sutskever I, Hinton GE. ImageNet Classification with Deep Convolutional Neural Networks n.d.
 - [23] Shimobaba T, Kakue T, Ito T. Convolutional Neural Network-Based Regression for Depth Prediction in Digital Holography. *IEEE Int Symp Ind Electron* 2018;2018-June:1323–6.
<https://doi.org/10.1109/ISIE.2018.8433651>.
 - [24] Xu Z, Ren Z, Lam EYM. Autofocusing in digital holography using deep learning 2018:56.
<https://doi.org/10.1117/12.2289282>.
 - [25] Goodman JW. Introduction to Fourier optics 1968.
 - [26] Trujillo C, Piedrahita-Quintero P, Garcia-Sucerquia J. Digital lensless holographic microscopy: numerical simulation and reconstruction with ImageJ. *Appl Opt* 2020;59:5788. <https://doi.org/10.1364/ao.395672>.
 - [27] Piedrahita-Quintero P, Trujillo C, García-Sucerquia J. Digital Lensless Holographic Microscopy plugin for ImageJ n.d. <https://unal-optodigital.github.io/DLHM/>.
 - [28] Kreuzer HJ, Pomerleau N, Blagrove K, Jericho MH. Digital in-line holography with numerical reconstruction. *SPIE Interferom '99 Tech Technol* 1999;3744:65–74. <https://doi.org/10.1117/12.357756>.
 - [29] Amoah AS, Vdovin G, Gong H, Verhaegen M, Agbana TE, Bezzubik V. Aliasing, coherence, and resolution in a lensless holographic microscope. *Opt Lett Vol 42, Issue 12, Pp 2271-2274* 2017;42:2271–4.
<https://doi.org/10.1364/OL.42.002271>.
 - [30] Lopera MJ, Trujillo C. Holographic point source for digital lensless holographic microscopy. *Opt Lett* 2022;47:2862. <https://doi.org/10.1364/ol.459146>.
 - [31] Buitrago-Duque C, Garcia-Sucerquia J. Sizing calibration in digital lensless holographic microscopy via iterative Talbot self-imaging. *Opt Lasers Eng* 2020;134:106176.
<https://doi.org/10.1016/J.OPTLASENG.2020.106176>.
 - [32] Aloysius N, Geetha M. A review on deep convolutional neural networks. *Proc 2017 IEEE Int Conf Commun Signal Process ICCSP 2017* 2018;2018-January:588–92.
<https://doi.org/10.1109/ICCSP.2017.8286426>.
 - [33] Cun Y Le, Denker JS, Henderson D, Howard RE, Hubbard W, Jackel LD. Handwritten Digit Recognition with a Back-Propagation Network n.d.
 - [34] Ian Goodfellow, Yoshua Bengio and AC. Deep ILearning. *Genet Program Evolvable Mach* 2017;19:305–7.
 - [35] EAFIT U. Home - Apolo - Universidad EAFIT n.d. <https://www.eafit.edu.co/apolo> (accessed September 19, 2022).
 - [36] EAFIT U. Apolo Scientific Computing Center's Documentation — apolo-docs 0.1 documentation n.d.
<https://apolo-docs.readthedocs.io/en/latest/index.html> (accessed September 19, 2022).
 - [37] Trujillo CA, Garcia-Sucerquia J. Automatic method for focusing biological specimens in digital lensless holographic microscopy. *Opt Lett Vol 39, Issue 9, Pp 2569-2572* 2014;39:2569–72.
<https://doi.org/10.1364/OL.39.002569>.

CONFERENCE PROCEEDINGS



Single-shot dual-wavelength Polarized Microscope to detect Malaria-infected Erythrocytes via birefringence response

Maria Josef Lopera¹, Adriana Pabón² and Carlos A. Trujillo^{1*}

¹Applied Optics Group, Physical Sciences Department, School of Science, Universidad EAFIT, Medellín, Colombia.

²Malaria Group, Universidad de Antioquia, Medellín, Colombia.
catrujilla@eafit.edu.co

Abstract: The implementation of a dual-wavelength polarized microscope to obtain the birefringence response of Malaria-infected Erythrocytes is presented. By retrieving the dichroism images of blood samples, those containing the Plasmodium parasite can be detected. © 2021 The Author(s)

1. Introduction

Polarization of light is an optical property that reveals inner structures and optical activity of a sample without the need of contrast agents[1] giving access to intrinsic information about the morphology and composition of its structures and dynamics. Thanks to this feature, polarized techniques applied to microscopy are largely used in biomedical applications to study the nature of tissues and the structural information of different biological specimens. Among other uses, polarization measurements are widely employed in biomedicine to potentiate the diagnose of different human diseases[2][3]; one of those diseases is Malaria. Malaria is produced by the Plasmodium parasite and is transmitted by the infected female Anopheles mosquitoes[4]. The estimated number of malaria deaths stood at 405.000 in 2018[4][5]. Early diagnosis and treatment of Malaria reduces the potential negative effects of the disease and contributes to reduce its transmission. In this contribution, we propose a dual-wavelength polarized microscope to study blood samples with infected and non-infected red blood cells (RBC). This implementation allows detecting the presence of the parasite in the studied samples acquiring a single shot by a color camera for the 632.8nm and 533nm responses of the samples to cross polarized illuminations.

2. Single-shot dual-wavelength Polarized Microscope

The dual-wavelength polarized microscope setup is shown in Figure 1. The coherent illumination is generated by the superposition of a 632.8 nm JDSU He-Ne gas laser and a 533 nm Cobolt Solid State laser. The images are acquired by a Thorlabs CMOS color camera sensor, with 1024x1280 square pixels, each of 3.6 µm pitch. This configuration also allows the implementation of a bright field microscope, by employing a Fiber-Coupled illuminator. A beam splitter cube is used to integrate both the coherent and incoherent light sources. The collimated beam passes through a first polarizer (P1) which has a vertical polarization, then the polarized light illuminates the sample and a 40X/0.65 microscope objective (MO) produces the intermediate image at a conjugated plane of the camera sensor plane by means of a 300mm focal length tube lens; this configuration provides a 66X total magnification. An analyzer (P2) is placed between the tube lens and the camera sensor.

To build the birefringence response images two acquisitions are required. Also, since a color camera is used, both the red and green responses of the sample are retrieved from the corresponding RGB components of the recorded images. The first acquisition is performed with both polarizers parallel and the second one with the polarizers perpendicular i.e., crossed polarizers. The birefringence response image for every wavelength is obtained via equation (1) [6][1],

$$I_D(\lambda) = \frac{I_{\parallel}(\lambda) - I_{\perp}(\lambda)}{I_{\parallel}(\lambda) + I_{\perp}(\lambda)} \quad (1)$$

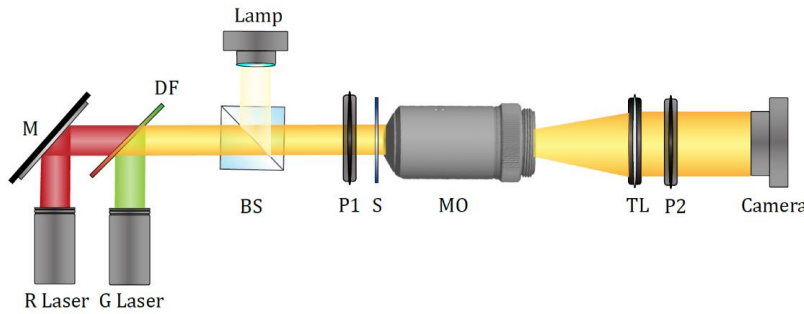


Figure 1. Scheme of the implemented dual-wavelength polarized microscope.

For this proposal, blood samples from continuous cultures of *Plasmodium falciparum* (strain FCR-3) maintained in RPMI 1640 culture medium, 5% hematocrit and 4% parasitemia were spread on slides and fixed with pure methanol. Figure 2 shows the birefringence response for malaria-infected (2(b) and 2(c)) and healthy (2(e) and 2(f)) RBCs. The birefringence response images for each wavelength are displayed with a colormap scale distributed between blue and red shades; the redder zones refer to positive dichroism and the bluer zones refer to negative dichroism. As can be checked in the zoomed-in area in 2(c), the RBCs develop a higher birefringence response to the green wavelength for the malaria-infected cells, particularly for the zone in which the parasite is located. The parasite presents negative dichroism for green light but not for red light, as can be seen in 2(b). The healthy RBCs do not present a strong birefringence response change throughout the cell, as can be seen in 2(e) and 2(f). As validated by the results in Figure 2, the detection of RBCs infected with the *Plasmodium* parasite is properly achieved with our proposal.

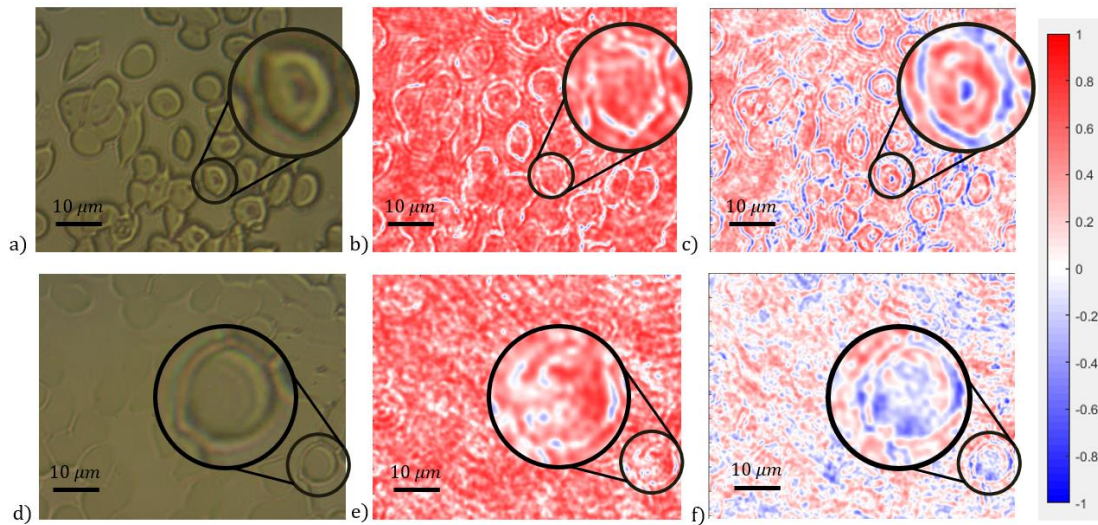


Figure 2. Visualization of birefringence response in *Erythrocytes*. (a) and (d) show the intensity images obtained with the white light source for malaria-infected and healthy cells, respectively. (b) and (e) show the reconstructed birefringence response images for $\lambda_1 = 632.8\text{nm}$ for malaria-infected and healthy cells, respectively. (c) and (f) show the reconstructed birefringence response images for $\lambda_2 = 533\text{nm}$ for malaria-infected and healthy cells, respectively.

3. References

- [1] I et al., "Phase and Polarization Contrast Methods by Use of Digital Holographic Microscopy: Applications to Different Types of Biological Samples," *Intech*, vol. i, no. tourism, p. 13, 2012.
- [2] W. Bishara et al., "Handheld, lensless microscope identifies malaria parasites,"
- [3] C. W. Pirnstill and G. L. Coté, "Malaria Diagnosis Using a Mobile Phone Polarized Microscope," *Sci. Rep.*, vol. 5, pp. 1–13, 2015.
- [4] "WHO | World Health Organization," WHO, 2019.
- [5] M. Poostchi, K. Silamut, R. J. Maude, S. Jaeger, and G. Thoma, "Image analysis and machine learning for detecting malaria," *Transl. Res.*, vol. 194, pp. 36–55, 2018.
- [6] E. Hecht, *Optics*. Addison-Wesley, 2002.



Bright Field Polarimetric Microscope Web Application

Maria J. Lopera ^{1*} and Carlos Trujillo¹

¹Applied Optics Research Group, Physical Science Department, School of Science,
Universidad EAFIT, Medellín, Colombia.

[*mloper23@eafit.edu.co](mailto:mloper23@eafit.edu.co)

RESUMEN:

Polarization is an optical property that allows samples' structural information retrieval, such as their molecular arrangement [1]. The detection of various components in biological samples, like calcium oxalate crystals [2] [3], is enabled through polarization measurements. Thanks to the latter, polarimetric microscopes are used in biomedical applications including the characterization of transparent bacteria, the examination of tissues as the eye cornea [2], the detection of malaria in red blood cells [3] [4], the early diagnosis of gout disease [5] and other urinary diseases [6] [7].

On the other hand, numerical simulations are essential tools when developing an optical system [8]. These computer-based approaches complement the experimental setup by validating and predicting their behavior, helping to solve setbacks efficiently, and reducing development times and costs. Nonetheless, implementing numerical simulations of optical devices requires deep knowledge of optics fundamentals, which in many cases inhibits their applicability. Web applications have been developed to cope with this limitation by facilitating access to simulations in optics concerning ray tracing [9], optical coherence tomography [10], and interferometry [11]. Among the many advantages of web applications are: i) their quick and easy access, ii) no local installations or updates are required, and iii) their compatibility with any internet-enabled device, such as cell phones.

This contribution reports a bright-field polarimetric microscope's numerical simulation in a web application. In the main interface of this software, the user can interact with the elements that compose the polarimetric microscope, such as the polarization-states analyzer and the polarization states generator, the Jones matrices that make up the sample, the magnification, the numerical aperture of the instrument, and the wavelength of the illumination source. The web application includes two more interfaces for experimental or synthetic data post-processing. In the first interface, the computing of the dichroic response of a microscopic sample can be performed. The second interface allows computing the Stokes parameters of a light beam as long as its general, linear, and circular degree of polarization. This web application can be accessed freely via [12].

Palabras claves: Polarimetry, polarization, polarized, polarimetry, microscopy, web app, user interface, software, modeling, simulation.

Tópico del Trabajo: OFP: Óptica de Fourier y procesamiento óptico

Modalidad que preferiría:

Ponencia Oral (X)

Póster: ()

Presentará manuscrito para evaluación y posible publicación: Sí: (X) No: ()

Correo electrónico de contacto: mloper23@eafit.edu.co

Referencias:

1. E. Collett, *Field Guide to Polarization* (2009).
2. L. P. Maksimova, I.L. Tuchin, V.V. Shubochkin, "Polarization features of eye's cornea," USSR (1986).
3. M. J. Lopera and C. Trujillo, *Polarimetric Microscope for Malaria Infected Red Blood Cells Analysis* .CLEO (2021).
4. C. W. Pirnstill and G. L. Coté, "Malaria Diagnosis Using a Mobile Phone Polarized Microscope," Sci. Rep. **5**, 1–13 (2015).
5. B. Bai, H. Wang, T. Liu, Y. Rivenson, J. FitzGerald, and A. Ozcan, "Pathological crystal imaging with single-shot computational polarized light microscopy," J. Biophotonics (2020).
6. E. Mahoney, J. Kun, M. Smieja, and Q. Fang, "Review—Point-of-Care Urinalysis with Emerging Sensing and Imaging Technologies," J. Electrochem. Soc. **167**, 037518 (2020).
7. M. Asselman, A. Verhulst, M. E. De Broe, and C. F. Verkoelen, "Calcium Oxalate Crystal Adherence to Hyaluronan-, Osteopontin-, and CD44-Expressing Injured/Regenerating Tubular Epithelial Cells in Rat Kidneys," J. Am. Soc. Nephrol. **14**, 3155–3166 (2003).
8. J. W. Goodman, *Introduction to Fourier Optics* (Roberst & Company Publishers, 2005).
9. J. Rick Tu, "Ray Optics Simulation ," <https://ricktu288.github.io/ray-optics/>.
10. R. Mehta, D. Nankivil, D. J. Zielinski, G. Waterman, B. Keller, A. T. Limkakeng, R. Kopper, J. A. Izatt, and A. N. Kuo, "Wireless, Web-Based Interactive Control of Optical Coherence Tomography with Mobile Devices," Transl. Vis. Sci. Technol. **6**, 5–5 (2017).
11. V. Singh, R. Dubey, P. K. Panigrahi, and K. Muralidhar, "An educational website on interferometry," Proc. - 2012 IEEE Int. Conf. Technol. Enhanc. Educ. ICTEE 2012 (2012).
12. M. J. Lopera Acosta and C. A. Trujillo, "Bright Field Polarimetric Microscope Respository," https://github.com/mloper23/BF_Polarimeter_Microscope.

Holographic optical element for digital lensless holographic microscopy's illumination

Maria J. Lopera^{1,*} and Carlos Trujillo¹

¹Applied Optics Group, Physical Sciences Department, School of Applied Sciences and Engineering, Universidad EAFIT, Medellín, Colombia

*Corresponding author: mloper23@eafit.edu.co

Abstract: We present the development of a holographic optical element that creates a micrometrical point source producing the divergent spherical illumination needed for Digital Lensless Holographic Microscopy. Our proposal has been validated with biological samples. © 2022 The Author(s)

1. Introduction

Holographic optical elements (HOEs) are holographically recorded planar surfaces that base their optical function on efficiently diffracting an illumination wavefront into microstructure profiles [1,2]. HOEs are thinner, lighter, and more cost-effective compared to refractive optical elements. Light transmitted by a HOE can be modified to almost any desired distribution, achieving wavefront shapes otherwise impossible with conventional refractive elements or only attainable with complicated optical systems. In this contribution, we present the development of a HOE, recorded in a photopolymer film, that creates the required spherical wavefront illumination for digital lensless holographic microscopy (DLHM). DLHM is a computational imaging technique that removes the need for bulky interferometers and lenses of conventional holographic microscopy [3,4]. The hardware of this microscopy technique comprises a divergent spherical wavefront source, usually a point source, and a digital camera sensor. Although DLHM has been successfully applied to different applications in biology and medicine [5,6], its lateral resolution is restricted by the numerical aperture of the optical system, which in turn depends on the sensor's size and the divergence of the cone of light generated by the point source. The conventional approach to generating the point source involves micrometer pinholes [4]: these systems' main drawbacks are their unstable alignment, bulky mounts, and high cost. Although further developments in DLHM illumination have been reported [7–9], a proposal involving HOEs for this task has not yet been explored. Our proposed holographic point source (HPS) alleviates the aforementioned drawbacks of pinhole-based configurations by providing accurate spherical divergent wavefronts without using pinholes or lenses. Our HPS-DLHM has been demonstrated by properly imaging potato starch grains and epithelial cheek cell samples. Our proposal provides the demanded features for in-field applications of DLHM, such as easier optical alignment, higher mechanical stability, and cost-effectiveness.

2. Holographic point source in a DLHM setup

The setup implemented to register the HPS is presented in Fig. 1 panel (a). A 532 nm Cobolt laser is the illumination source of the system. The holographic film used is a C-RT20 photopolymer from Litholo [10]. A non-polarizing beam splitter cube divides the incident beam into the object and reference wavefronts. The reference wavefront spot is expanded and then impinges over the holographic film at a tilted angle θ . The object wavefront is focused by a 60x 0.85 Newport® microscope objective into an aluminum foil pinhole of $3\mu\text{m}$ diameter assuring the highly spatial coherent spherical illumination required in conventional DLHM [4]. The reference and object wavefronts interfere at the holographic film to record the interferogram that encodes the information of the experimental point source. To produce a real image of the point source, the film must be illuminated in the opposite direction to which it was recorded, as illustrated in Fig 1 panel (b). The point source can be reconstructed using non-planar coherent wavefronts or with different wavelengths to increase or decrease the size of the generated spot. To acquire HPS-DLHM holograms, the sample and sensor must be located in the optical axis of the reconstructed point source, as can be appreciated in Fig 1 (b). In that illustration, z is the reconstruction distance, i.e., the distance between the real image of the pinhole (the point source) and the sample plane; L is the distance between the point source and the camera sensor plane. The digital holograms are numerically reconstructed to obtain the sample's optical information; for further details on this numerical reconstruction process, refer to [11].

3. Validation

To validate the performance of our proposal, a sample containing potato starch grain has been imaged. The intensity reconstruction of this sample with the proposed HPS is displayed in Fig. 2 (a) and compared to the conventional DLHM intensity reconstruction in panel (b). For this sample, the digital holograms have been acquired using a 533nm wavelength laser illumination, a reconstruction distance z of 5mm, and a source-to-camera distance L of 10mm; the latter reconstruction parameters yield a magnification of 2x and lateral resolution of $1.7\mu\text{m}$. Via the conventional DLHM, the standard deviation as a measure of noise is 0.009 ± 0.0005 a.u with respect to the mean normalized intensity, and the sample to background

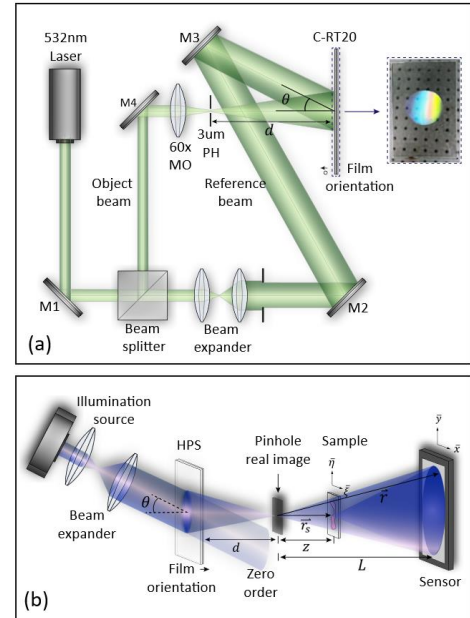


Fig. 1. (a) Illustration of the setup implemented to record the HPS. (b) Illustration of the HPS-DLHM setup.

contrast is 0.62. On the other hand, the background noise level obtained with our proposal is slightly lower for the same region ($\sigma=0.008\pm0.0005$ for the rectangular region enclosed by the orange dotted line) and the contrast slightly higher (0.64). The improvement in the sample's contrast against its background has been previously addressed in DLHM via preprocessing methods [12]. Overall, the smallest details of this sample are successfully recovered by our method (see the zoomed-in areas), thus validating the imaging capabilities of the HPS-DLHM. Finally, we demonstrate our proposal's quantitative phase imaging (QPI) capability for a low-absorption sample. In this experiment, a cheek epithelial cells sample has been imaged, numerically reconstructed, and compared against its conventional DLHM phase reconstruction. For this sample, the digital holograms are acquired with a 473nm wavelength laser illumination and a geometrical setup that yields $1.3\mu\text{m}$ of lateral resolution. The resulting phase reconstructions are presented in Fig. 2: in panel (c), the retrieved phase map according to our HPS-DLHM proposal, and in panel (d), the reconstruction retrieved employing conventional DLHM. As can be seen in the zoomed-in areas, the details of the specimens are adequately imaged by our method as conventional DLHM. In fact, these cells' distinctive nuclei and cellular membranes are retrieved successfully, and the quantitative phase values attained by both techniques are in close agreement. The region enclosed by the black dotted line has been selected to evaluate the background noise achieved by our method. This region's average phase value μ and standard deviation σ for the HPS-DLHM reconstruction are 0.3475 ± 0.0017 rad and 0.0925 ± 0.017 rad, in that order. The latter implies a similar noise level to the DLHM reconstruction ($\mu=0.306\pm0.0016$ rad and $\sigma=0.1083\pm0.014$ rad). Therefore, our method has been demonstrated for QPI of low-absorption biological samples by obtaining similar measurements to conventional pinhole-based DLHM.

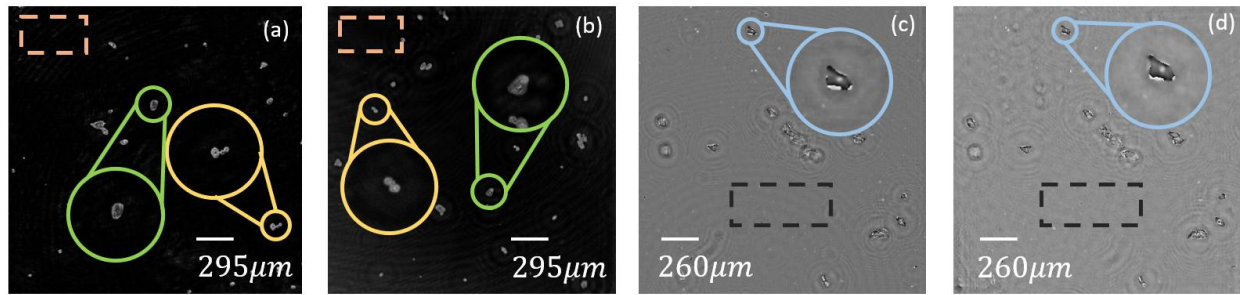


Fig. 2. Validation of the imaging performance of our HPS-DLHM proposal with potato starch grains (a) and (b) and epithelial cheek cells (c) and (d). (a) DLHM Intensity reconstruction by our proposal. (b) Conventional DLHM intensity reconstruction. (c) Phase reconstruction via our HPS-DLHM. (d) Phase reconstruction via conventional DLHM.

4. Conclusion

In this contribution, we reported the development of a holographic point source (HPS) for DLHM illumination. The HPS is a hologram of an experimental micrometer pinhole recorded in a photopolymer film that assures the required spatial coherence of DLHM. Our HPS-DLHM achieves similar performance compared to the conventional approach but with the advantages of being cost-effective, mechanically stable, and easier to align. The capability of our proposal to reconstruct the intensity and phase information of biological samples has been validated by direct comparison with conventional pinhole-based DLHM.

References

1. G. Saxby, *Practical Holography* (Institute of Physics Pub, 2004).
2. C. Delisle, L. N. Hazra, and Y. Han, "Stigmatic imaging by zone plates: a generalized treatment," *JOSA A*, Vol. 10, Issue 1, pp. 69-74 **10**, 69-74 (1993).
3. M. Roy, D. Seo, S. Oh, J. W. Yang, and S. Seo, "A review of recent progress in lens-free imaging and sensing," *Biosens. Bioelectron.* **88**, 130-143 (2017).
4. J. Garcia-Sucerquia, W. Xu, S. K. Jericho, P. Klages, M. H. Jericho, and H. J. Kreuzer, "Digital in-line holographic microscopy.," *Appl. Opt.* **45**, 836-50 (2006).
5. M. J. Lopera and C. Trujillo, "Linear diattenuation imaging of biological samples with digital lensless holographic microscopy.," *Appl. Opt.* **Accepted f**, (2021).
6. C. a Trujillo and J. Garcia-Sucerquia, "Automatic method for focusing biological specimens in digital lensless holographic microscopy.," *Opt. Lett.* **39**, 2569-72 (2014).
7. C. Trujillo and M. J. Lopera, "Portable cellphone-based digital lensless holographic microscope," *Front. Opt. + Laser Sci.* 2021 (2021), Pap. JTh5A.14 JTh5A.14 (2021).
8. H. Tobon-Maya, S. Zapata-Valencia, E. Zora-Guzmán, C. Buitrago-Duque, and J. Garcia-Sucerquia, "Open-source, cost-effective, portable, 3D-printed digital lensless holographic microscope," *Appl. Opt.* **60**, A205 (2021).
9. B. Patiño-Jurado, J. F. Botero-Cadavid, and J. Garcia-Sucerquia, "Cone-shaped optical fiber tip for cost-effective digital lensless holographic microscopy," *Appl. Opt.* **59**, 2969-2975 (2020).
10. Litiholo, *Litiholo 2.0 C-RT20 Film Data Sheet* (n.d.).
11. C. Trujillo, P. Piedrahita-Quintero, and J. Garcia-Sucerquia, "Digital lensless holographic microscopy: numerical simulation and reconstruction with ImageJ," *Appl. Opt.* **59**, 5788 (2020).
12. H. Tobon, C. Trujillo, and J. Garcia-Sucerquia, "Preprocessing in digital lensless holographic microscopy for intensity reconstructions with enhanced contrast," *Appl. Opt.* **60**, A215 (2021).

Portable cellphone-based digital lensless holographic microscope

Maria Josef Lopera^{1,*} and Carlos Trujillo¹

¹Applied Optics Group, Physical Science Department, School of Science, Universidad EAFIT, Medellín, Colombia
mloper23@eafit.edu.co

Abstract: The implementation of a compact and portable digital lensless holographic microscope (P-DLHM) attached to a cellphone is presented. This proposal offers a potential tool for telemedicine applications via the *in-situ* study of biological samples. © 2021 The Author(s)

1. Introduction

According to 2021 mobile user statistics[1], the total number of people owning a cellphone represents 62% of the world's population; 48% of these users are located in developing countries and 80% of these currently lives in locations vastly covered with wireless communication[2]. The latter has led to a reduction of the costs of the devices and a constant improvement of their robust hardware and software capabilities[3]. Among the features that are constantly improved are smartphone cameras, which has propelled the implementation of “smartphone-based” technologies for biomedical applications [4]. The use of smartphones along with portable optical instruments to image parasitic diseases is a trending topic concerning this common health problem particularly important in developing countries[4]. To address this important need for diagnosing diseases, several research has been conducted on miniaturizing the existing designs of medicine tools [4,5]. Lensless imaging has become an alternative technique, mainly owing to its low cost and high optical throughput [6] to detect and diagnose diseases [7–9]. Considering the need for inexpensive and autonomous technology to diagnose diseases, we propose a portable cellphone-based digital lensless holographic microscope (P-DLHM) that offers a potential tool for telemedicine applications. This proposal is validated by *in-situ* imaging biological samples of dry leaf venules and an insect antenna via a regular cellphone.

2. Portable digital lensless holographic microscope

The compact P-DLHM setup is shown in Fig. 1. The spatially coherent illumination is generated by the collimation and spatial filtering of a high-power LED powered with a recharger Li-ion battery of 3.8 V output. The collimation and focusing of the illuminating light are performed with a 4f-system and a homemade pinhole. L_1 is a +25mm plano-convex lens from Newport and L_2 is a 15mm plano-convex lens from Thorlabs. The pinhole is an aperture of $3\mu\text{m}$ of diameter. The camera of a Samsung S10+ acquires the holograms in this setup. This camera acquires images of 3024×3024 square pixels, each of $1\mu\text{m}$ pixel pitch. The sample is placed close ($\sim 1\text{mm}$) to the pinhole to obtain a total magnification of around 20X[10]. The cellphone camera sensor is located 20 mm from the pinhole thus yielding a numerical aperture of 0.076 and a lateral resolution of $3.5\mu\text{m}$ [10]. A mechanic coupling fixes all the previously described optical elements. This coupling was manufactured in a 3D printer. Fig. 1. shows the computer assisted design (CAD) in panel (b), and the final prototype in panel (c). Considering all the elements that compound the P-DLHM, the final volume of the prototype is $6 \times 4 \times 9 \text{ cm}^3$ and its weight is 120g. The total prototype's cost is 140 USD.

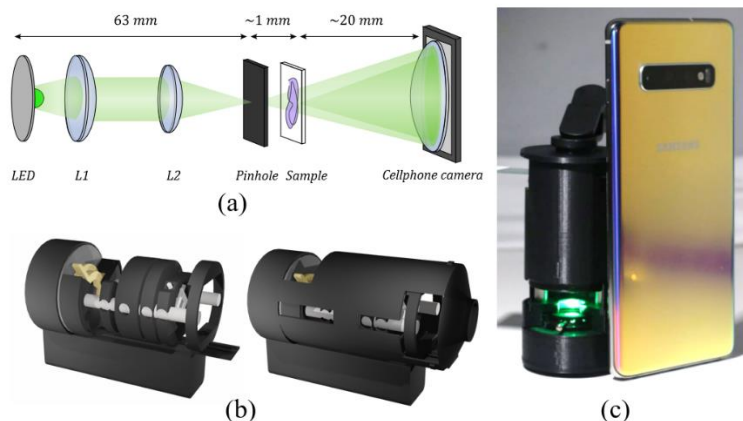


Fig. 1. (a) Scheme of the implemented P-DLHM. (b) CAD design of the mechanical coupling. (c) Photograph of the prototype accompanied by the cellphone used to register the holograms.

The numerical reconstruction of the registered holograms is performed via an ImageJ® plugin for DLHM[10]. For this proposal, *in-situ* samples of the venules of a dry leaf and a *coleoptera* antenna were imaged. For comparison, in Fig. 2 panel (c) and panel (f) are shown the bright field image of the biological samples. In panels (b) and (e) the intensity reconstructions of the samples using the proposed P-DLHM are presented. In panels (a) and (d) the registered holograms are presented. As can be seen in the intensity reconstructions, the information of the imaged biological samples is properly recovered when compared with a more robust non-portable bright field microscope. As the proposed device allows imaging samples whose size is larger than $3.5\mu\text{m}$, which is an ideal resolution for sampling biological objects such as cell colonies, parasites, or human tissues, the proposed P-DLHM offers a potential tool for portable applications such as those required in the diagnosis of diseases in telemedicine.

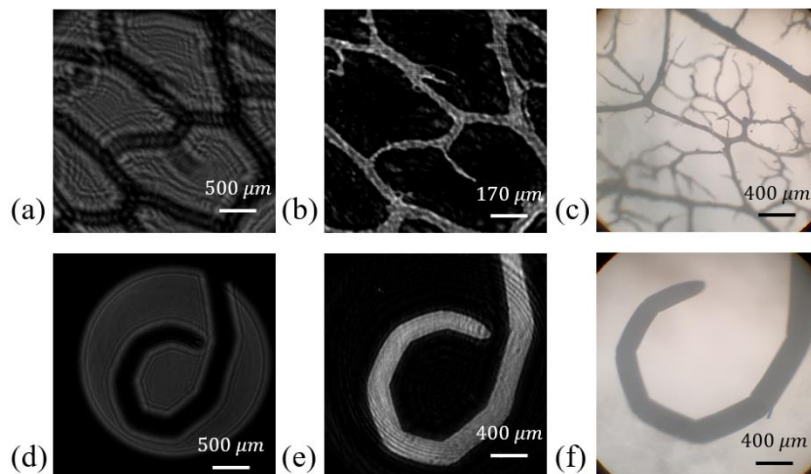


Fig. 2. (a) Bright field image of a dry leaf venules. (b) and (c) numerical reconstruction and hologram acquired by the LD-DLHM of sample (a). (d) Bright field image of an insect antenna. (e) and (f) numerical reconstruction and hologram acquired by the LD-DLHM of sample (d).

3. References

1. Ash Turner, "How Many People Have Smartphones Worldwide (Jun 2021)," URL "<https://www.bankmycell.com/blog/how-many-phones-are-in-the-world>".
2. D. Tseng, O. Mudanyali, C. Oztoprak, S. O. Isikman, I. Sencan, O. Yaglidere, and A. Ozcan, "Lensfree microscopy on a cellphone," *Lab Chip* **10**(14), 1787–1792 (2010).
3. J. C. Contreras-naranjo, Q. Wei, and A. Ozcan, "Mobile Phone-Based Microscopy , Sensing , and Diagnostics," **22**(3), (2016).
4. S. Banik, S. K. Melanthota, Arbaaz, J. M. Vaz, V. M. Kadambalithaya, I. Hussain, S. Dutta, and N. Mazumder, "Recent trends in smartphone-based detection for biomedical applications: a review," *Anal. Bioanal. Chem.* **413**(9), 2389–2406 (2021).
5. E. McLeod and A. Ozcan, "Unconventional methods of imaging: Computational microscopy and compact implementations," *Reports Prog. Phys.* **79**(7), (2016).
6. Y. Zhou, B. Xiong, X. Li, Q. Dai, and X. Cao, "Lensless imaging of plant samples using the cross-polarized light," *Opt. Express* **28**(21), 31611 (2020).
7. Y. Yoo, Y. J. Seo, M. Huh, J. H. Yoo, K. H. Yun, and S. J. Kim, "Gout and coexisting pseudogout in the knee joint," *Knee Surgery, Sport. Traumatol. Arthrosc.* **19**(4), 553–555 (2011).
8. M.-R. Antonelli, A. Pierangelo, T. Novikova, P. Validire, A. Benali, B. Gayet, and A. De Martino, "Mueller matrix imaging of human colon tissue for cancer diagnostics: how Monte Carlo modeling can help in the interpretation of experimental data," *Opt. Express* **18**(10), 10200 (2010).
9. G. Coppola and M. A. Ferrara, "Polarization-sensitive digital holographic imaging for characterization of microscopic samples: Recent advances and perspectives," *Appl. Sci.* (2020).
10. C. Trujillo, P. Piedrahita-Quintero, and J. Garcia-Sucerquia, "Digital lensless holographic microscopy: numerical simulation and reconstruction with ImageJ," *Appl. Opt.* **59**(19), 5788 (2020).

Portable cellphone-based digital lensless holographic microscope (P-DLHM)

Maria Josef Lopera^{*,1} and Carlos A. Trujillo¹

¹Applied Optics Group, Physical Science Department, School of Science, Universidad EAFIT, Medellín, Colombia

*mloper23@eafit.edu.co



Smartphone-based technology



89.9% of people own mobile phones today



48% located in developing countries



80% covered with wireless communication

Mainstreaming use of cellphones has diminished their **cost** and **improved** their **hardware** and **software**, which has led to the emergence of:

Smartphone-based technology used in **biomedical** applications

Lensless imaging has become a trend and an ideal technique for this topic, mainly owing to its low cost and high optical throughput to **detect** and **diagnose diseases**.

Low-income areas need **inexpensive** and **autonomous** technology to mitigate **public health problems**

We propose a **portable cellphone-based digital lensless holographic microscope** (P-DLHM) that offers a potential tool for telemedicine applications.

Portable digital lensless holographic microscope optical setup

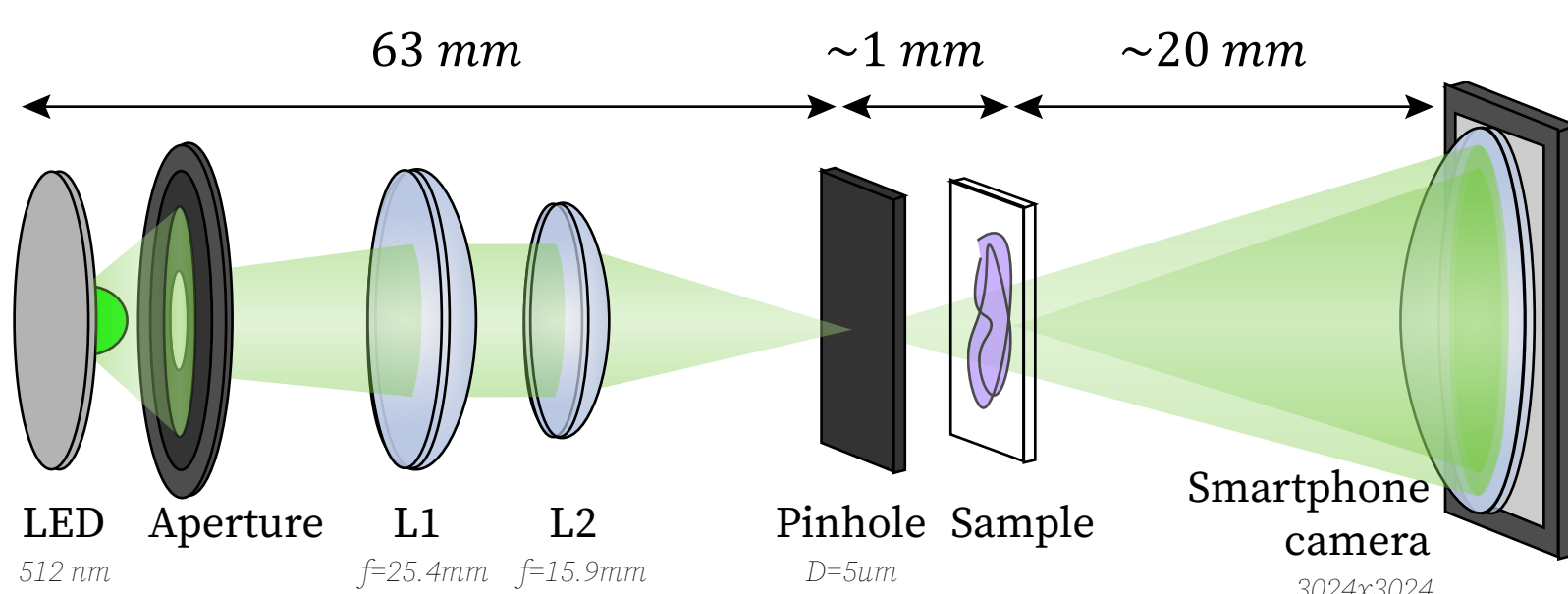


Fig. 1. Scheme of the implemented portable DLHM

The DLHM **spherical wavefront source** is generated by the collimation and spatial filtering made by a **4-f system** and a **homemade pinhole** of a high-power **LED** powered with a recharger Li-ion battery of 3.8 V output.

With the geometrical configuration presented in Fig. 1 the following properties can be achieved:

Smartphone	NA	Resolution	Magnification
Samsung S10+	0.076	3.5 μ m	20x

Mechanical coupling

A 3D-printed mechanical coupling fixes all the previously described optical elements. Fig. 2. shows the computer assisted design (CAD) and a picture of the final prototype attached to a cellphone.

Dimensions	Weight	Cost
6x4x9 cm ³	120 gr	140 USD

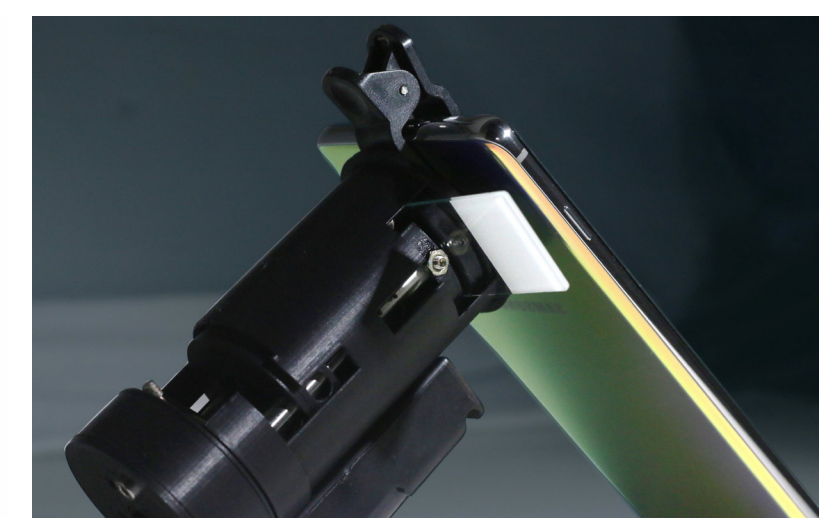
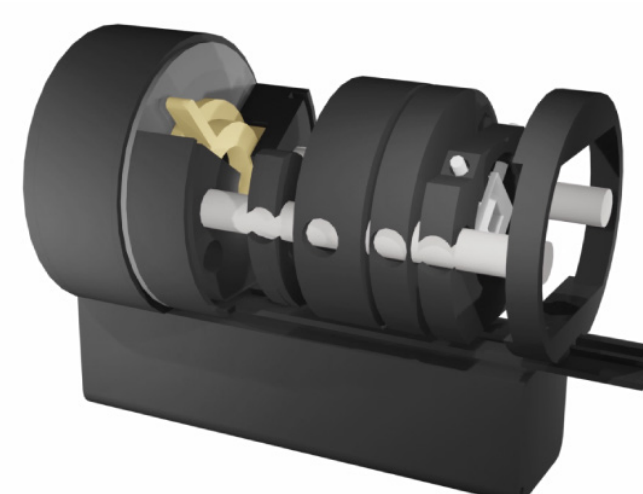


Fig. 2. Computer assisted design and picture of the portable DLHM

Results & discussion

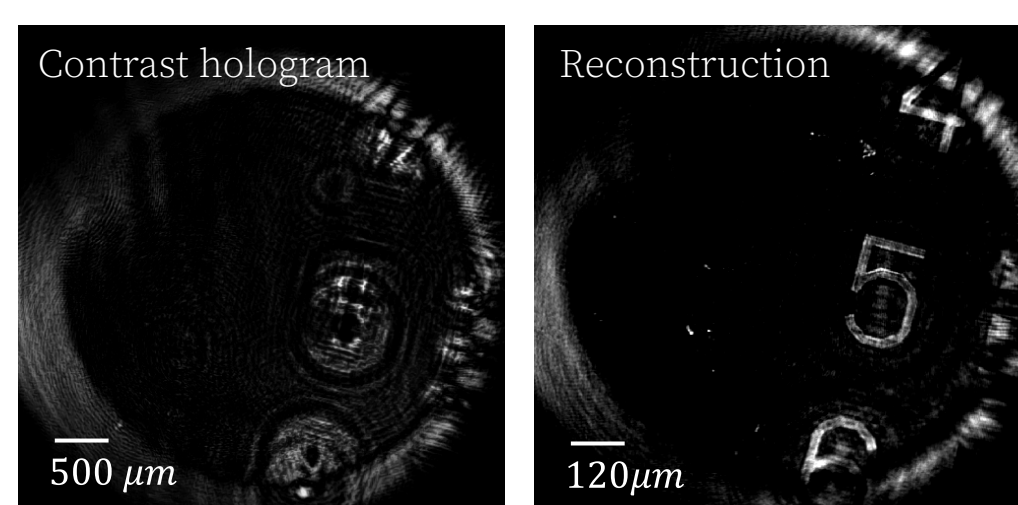


Fig. 3. Contrast hologram and reconstruction of a USAF test

Reference and hologram intensity images are captured with the cellphone in manual mode, with infinite focal distance and with low exposure time avoiding to overexpose the images. The intensities are numerically subtracted to find the contrast hologram. The numerical reconstruction is performed via an ImageJ[®] plugin for DLHM.

In-situ samples of the venules of a dry leaf and a coleoptera antenna were imaged. For comparison, in Fig. 4 are shown the bright field image and the intensity reconstructions of the samples using the proposed P-DLHM. The information of the imaged biological samples is properly recovered when compared with a more robust, more expensive, non-portable bright field microscope. The proposed device allows imaging samples whose size is larger than 3.5 μ m, which is an ideal resolution for sampling biological objects.

The proposed P-DLHM offers a potential tool for portable applications such as those required in the diagnosis of diseases in telemedicine.

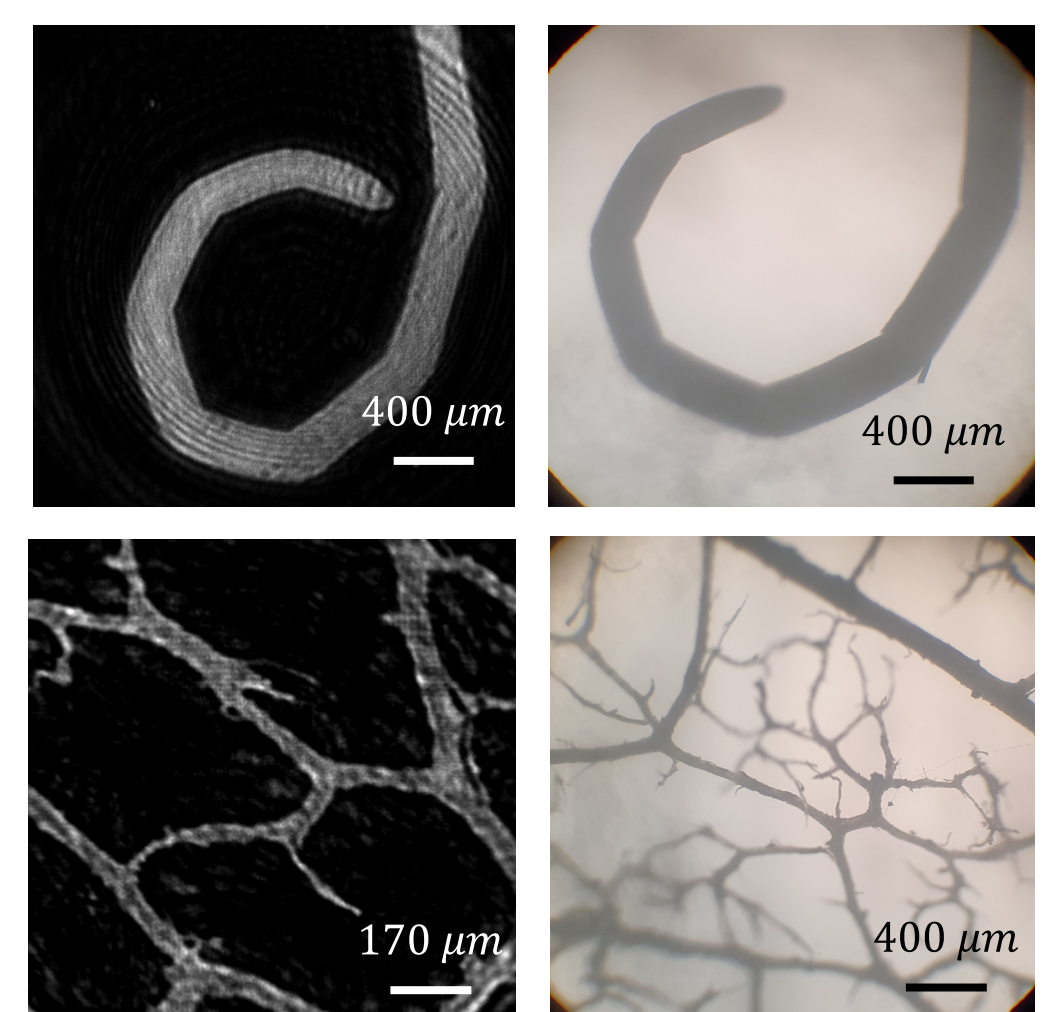


Fig. 4. P-DLHM intensity reconstructions (left) and bright field intensity images (right) of coleoptera antenna and dry leaf venules.

Autofocusing Convolutional Neural Network Regression Model for Digital Lensless Holographic Microscopy

Maria J. Lopera^{1,*}, Manuel Montoya^{1,*} and Carlos Trujillo¹

¹Applied Optics Group, Physical Sciences Department, School of Applied Sciences and Engineering, Universidad EAFIT, Medellín, Colombia

*Corresponding authors: mloper23@eafit.edu.co, mmonto95@eafit.edu.co

Abstract: We propose a convolutional neural network (CNN) - based regression model to predict the reconstruction distance of contrast lens-free digital holograms. The model predicts the depth position of the object with millimetric precision. © 2022 The Author(s)

1. Introduction

Digital lensless holographic microscopy (DLHM) is an interferometric based imaging technique which relies on computational methods to reconver information of samples, is one of the simplest imaging techniques. Its simplicity is synthesized in terms of the required elements: a divergent spatially coherent spherical wavefront and a sensor. It enables the reconstruction of both amplitude and phase of three and two-dimensional objects as the DLHM hologram could be thought of as the intensity distribution yielded from the superposition between the illumination source perturbed (object) and non-perturbed (reference) by the sample [2]. To retrieve the optical field $U(x, y, z)$ of an object, a numerical reconstruction consisting of applying a scalar diffraction formula must be performed [1,3]. The depth position of the object must be known precisely to properly reconstruct its optical field and most of the times, this value is not known [4]. Autofocusing methodologies have been proposed to overcome this drawback. They consist of reconstructing a stack of in-focus and out-of-focus images and using a metric to calculate the sharpness of each reconstructed image [4,5]. A number of focusing metrics in digital holography have been proposed [5–7]. Among these, a metric that presents good performance for DLHM is the power spectrum-based presented in Eq (1). Here $U(x, y, z)$ is the optical field for a defined z position and ft is the Fourier transform of the field [5]. With this metric, the focused plane is found when C_z reaches zero. This metric is going to be used to compare the performance of our proposed model.

$$C_z = 1 - N \left(\left| \sum_{x,y} \log_{10}(1 + ft\{|U(x, y, z)|\}) \right| \right) \quad (1)$$

The implementation of classical autofocusing methodologies is time-consuming and computationally demanding, limiting the on-field applications of lens-free microscopy. Deep Learning (DL) has shown to be one of the most effective and promising techniques in image processing related fields, such as computer vision and medical image analysis [4]. Convolutional Neural Networks (CNN) have played a major role in the development of this field, due to their ability to learn abstract representations from a given set of images. Few studies implementing DL models for autofocusing in digital lens-based holography have emerged in recent years. Z. Ren et. al [4] proposed to solve the problem by splitting the z space into categories and by implementing a classification CNN, in which the true distance is mapped to a label. For fine tuning of the final reconstruction distance, diffraction operations must be performed in the specific classification predicted range. Also, the same authors proposed a LeNet based regression model to predict the focal distance. They report an absolute error of 0.01 mm in the prediction for phase and amplitude objects. In another study, T. Shimobaba et. al. proposed a CNN regression model to directly predict the focus distance from the power spectrum of the hologram, they report a mean absolute error of 5mm. All the proposals include simulated and experimental digital holograms, but no studies have shown to be proved in DLHM techniques. We propose a regression model based on Convolutional Neural Networks to predict the reconstruction distance of contrast DLHM holograms.

2. Model architecture

Fig. 1. illustrates the architecture used to train the model. The input layer is composed of one channel, representing the contrast DLHM hologram, which can be found by directly subtracting the reference to the hologram intensity matrices. Then, a data augmentation layer is defined, which randomly rotates the hologram in 0°, 90°, 180° or 270°, helping reduce overfitting. The next preprocessing layer adds a second channel that is the intensity of the power spectra of the hologram in logarithmic scale and plays a very important role in increasing generalization, thus reducing overfitting further. This two-channel layer is then fed to the *convolutional backbone*, which is composed of 5 convolutional blocks and serves the purpose of feature extraction. Each convolutional block is composed of a convolutional layer, followed by a batch normalization layer,

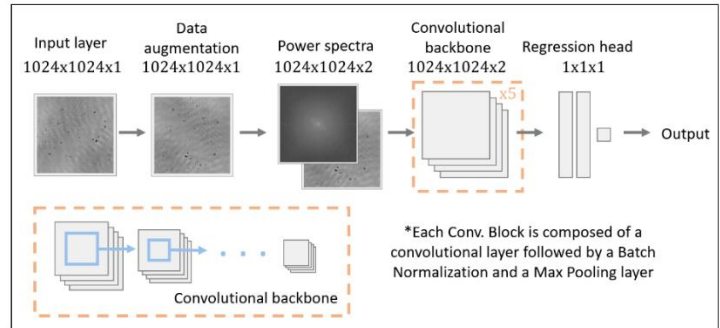


Fig. 1. Scheme of the implemented CNN model architecture.

followed by a max pooling layer. Note that as the network goes forward inside the *convolutional backbone*, the number of filters keeps increasing while the transformed image size keeps decreasing, as can be seen in Fig. 1. Finally, the transformed data is fed to the *regression head* after applying a dropout and a flatten layer. This *regression head* is composed of two fully connected layers and the output layer that contains only one neuron. *ReLU* activation function is used throughout the network, excepting for the output layer which has a linear activation function. Adam optimizer is used as the optimization algorithm and the learning rate starts at 0.001, decreasing by a factor of 2 every 15 epochs and then decreasing exponentially at each epoch after epoch 120. The loss function is defined as the *mean squared error (MSE)* and the training process was performed in a server with 3 *NVIDIA TESLA V100* GPUs, that allowed a training time of ~ 8 hours with a batch size of 64 images.

3. Results

The dataset for training consists of 3000 8-bit contrast holograms of five samples including red blood cells, epithelial cells, potato starch, among others. The holograms were acquired with a DLHM setup as the one presented in [2] with 473 nm wavelength, numerical aperture of 0.12 and lateral resolution of $4\mu\text{m}$. The samples were moved along the depth direction ranging from 1 to 20 mm. The depth value for each contrast hologram was retrieved using the power spectrum-based autofocusing metric previously described and using angular spectrum as diffraction formula. As the holograms were acquired with spherical wavefront and reconstructed with plane wavefront, the numerical depth position differs from the experimental one. The angular spectrum depth distances range from 5 to 60 mm. Fig. 2. Panel (a) depicts the loss function of the model. Values of 0.5 mm^2 were achieved and the average depth error of our model is 0.5 mm for the training dataset and 0.9 mm for the testing dataset. To verify the effectiveness of our CNN, a random hologram was used to measure quality intensity reconstruction metrics. This hologram is part of the validation sub-dataset. We performed the depth search using the power-spectrum-based metric previously described ranging from 5mm to 60mm, with depth step of 0.15 mm . The coefficient plot versus z is shown in Fig. 2. Panel (b). This plot shows the minimum coefficient at $z_c = 19.25\text{ mm}$. The computing time to obtain this value is $t_c = 10 \pm 1\text{ sec}$ on an *Intel Core i7 8th Gen* with *16 GB RAM* and no parallelization. Subsequently, the CNN was used to predict the depth value directly, obtaining $z_{\text{CNN}} = 21.03\text{ mm}$. The computing time needed to find the depth value is $t_{\text{CNN}} = 3 \pm 1\text{ sec}$. The difference between the actual depth and the predicted depth is 1.76 mm . Fig. 2. shows the intensity reconstruction with coefficient depth value (panel (c)) and with the proposed CNN (panel (d)). Differences between both reconstructions can be appreciated. The contrast for the coefficient-based reconstruction in the zoomed areas reaches 0.94 meanwhile the CNN is 0.71. In the same areas gradient as metric of sharpness was calculated. For the ground truth image, the sharpness of the cells is $0.63 \pm 0.01\text{ a.u.}$ and for the CNN reconstruction is $0.14 \pm 0.01\text{ a.u.}$ For both cases the background noise is almost zero (intensity mean of $1e^{-4}$). It is important to note that despite the differences in the metrics, the model allows a very close-to-ideal reconstruction, that could be further tuned by performing the metric-based autofocusing calculations if needed.

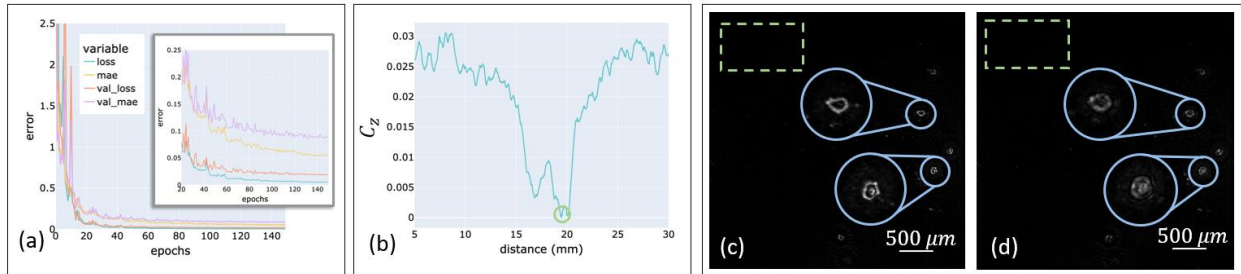


Fig. 2. CNN Training plot (a). Power spectrum-based autofocusing metric for a sample containing cat's cheek epithelial cells (b), ground truth depth value is highlighted with green circle. Intensity reconstruction with ground truth depth distance (c) and with the proposed CNN regression model (d).

4. Conclusion

We proposed a CNN-based regression model which enables the direct prediction of the depth value of contrast DLHM holograms with millimeter precision, reducing overall computation time up to three times. The power spectrum of the contrast hologram is calculated and together with the hologram itself is the input of the CNN backbone of the model. A data augmentation layer is included to prevent overfitting. Further improvements in the original dataset and the training process are likely to improve overall performance and are proposed as future work. By predicting the depth value, our model allows having reconstructions of the optical field of the samples with high contrast and focus as the error in the position is less than 4%. Our model represents an advance for the autonomy of the DLHM technique, enabling future applications and facilitating its use.

References

1. J. Garcia-Sucerquia, W. Xu, S. K. Jericho, P. Klages, M. H. Jericho, and H. J. Kreuzer, "Digital in-line holographic microscopy," *Appl. Opt.* **45**, 836–850 (2006).
2. M. J. Lopera and C. Trujillo, "Linear diattenuation imaging of biological samples with digital lensless holographic microscopy," *Appl. Opt.* **61**, B77 (2022).
3. J. W. Goodman, *Introduction to Fourier Optics* (Roberst & Company Publishers, 2005).
4. Z. Xu, Z. Ren, and E. Y. M. Lam, "Autofocusing in digital holography using deep learning," *56* (2018).
5. C. Trujillo and J. Garcia-Sucerquia, "Comparative analysis of the modified enclosed energy metric for self-focusing holograms from digital lensless holographic microscopy," *Appl. Opt.* **54**, 5102 (2015).
6. M. Lyu, C. Yuan, D. Li, and G. Situ, "Fast autofocusing in digital holography using the magnitude differential," *Appl. Opt.* **56**, F152 (2017).
7. C. Trujillo and J. Garcia-Sucerquia, "Two-stage autofocusing methodology for digital lensless holographic microscopy," *Imaging Appl. Opt.* **2018**

(3D, AO, AIO, COSI, DH, IS, LACSEA, LS&C, MATH, pcAOP) (2018), Pap. DTu2F.6 Part F100-, DTu2F.6 (2018).

Linear diattenuation sensitive lens-free holographic microscope

Maria J. Lopera^{1,*} and Carlos Trujillo¹

¹Applied Optics Group, Physical Sciences Department, School of Applied Sciences and Engineering, Universidad EAFIT, Medellín, Colombia

*Corresponding author: mloper23@eafit.edu.co

Abstract: We report the implementation of the simplest lens-free holographic microscope sensitive to linear diattenuation of biological samples using two linear polarizers. We validate our proposal by imaging calcium oxalate crystals and potato starch grains. © 2022 The Author(s)

1. Introduction

In the available state of the art of lens-free holographic microscopy (LHM) [1], the possibility to quantify polarization properties of samples has been reported using intricate optical implementations and computationally complex algorithms [2,3]. The need for proposals involving simple experimental setups with potential field-portability and straightforward numerical processing is still a research topic in LHM [4], particularly in its modality where the large sample-to-sensor distances are employed, i.e., digital lensless holographic microscopy [5]. In this contribution, we report a lensless holographic microscope sensitive to the linear diattenuation produced by biological samples. This proposal only requires the insertion of two linear polarizers in a conventional LHM setup and basic arithmetic point-wise operations between two intensity reconstructions. Up to the best knowledge of the authors, this is the simplest proposal for a linear diattenuation sensitive lens-free holographic microscope.

2. Linear Diattenuation sensitive LHM

The proposed linear diattenuation sensitive lens-free holographic microscope (LD-LHM) is presented in Fig. 1. The illumination source is a CW 473nm laser source. A linear polarizer is used as a polarization states generator (PSG) to ensure the incident beam's vertical polarization state. A divergent spherical wavefront that fulfills the degree of spatial coherence required to register DLHM holograms [5] impinges the sample. Then, a second linear polarizer, which serves as a polarization states analyzer (PSA), is placed close to the camera.

In this implementation, the sample and the camera sensor are placed at distances z and L from the point source, respectively. To produce digital images carrying point-wise information of linear diattenuation $D(r, \vec{s})$, the first and second Stokes parameters must be computed, as mathematically expressed in Eq. (1).

$$D(\vec{r}_s) = \frac{S_1}{S_0} = \frac{I_0 + I_{90}}{I_0 - I_{90}} \quad (1)$$

In Eq. (1), I_0 and I_{90} are the transmitted reconstructed intensities when the PSA transmission axis is set parallel and perpendicular to that of the PSG in a given location $\vec{r}_s = (\zeta, \eta, z)$; (ζ, η) are the coordinates at the sample plane. The complete process to compute Eq. (1) with our proposal can be summarized in three steps: i) The DLHM holograms from which I_0 and I_{90} are to be recovered must be accurately acquired. The transmission angle for the PSG is set to 0° , i.e., vertical axis. Then the PSA is fixed first at 0° and then at 90° to register the two required acquisitions. ii) To recover I_0 and I_{90} from the DLHM holograms acquired in i), a numerical reconstruction process is required [6]. iii) With the I_{90} and I_0 transmittances recovered in ii), the subsequent calculation of a sample's point-wise linear diattenuation response can be straightforwardly performed by using (1). The exact details of the LD-LDH numerical processing can be read in [7], the proposal from which this contribution has been derived.

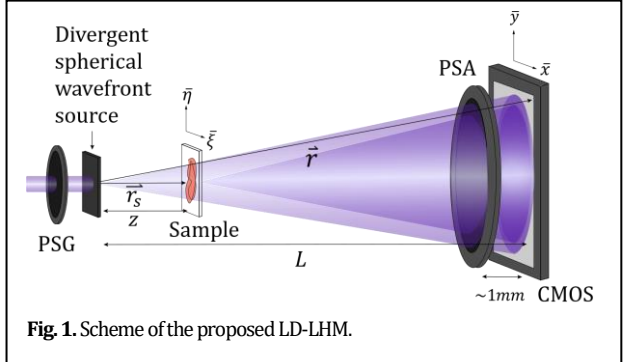


Fig. 1. Scheme of the proposed LD-LHM.

3. Proposal validation

We study two biological samples to validate our proposal experimentally. First, a sample containing calcium oxalate crystals has been imaged using the proposed LD-LHM. This sample was obtained from the maceration of the leaves of an *Agave Chiapensis* plant. For this sample, the brightfield intensity image and the intensity reconstruction via conventional LHM are depicted in Fig. 2 (a) and (b). The recovered linear diattenuation response with the proposed LD-LHM system is depicted in Fig. 2 (c). As can be appreciated in the zoom-in areas, this sample presents negative diattenuation according to our proposal, which agrees with other already reported works [8]. This measurement is unfeasible via conventional LHM or brightfield microscopy; therefore, the capability of our proposal to provide complementary information of samples with polarizing properties in LHM is demonstrated. The proper quantification of these properties represents a significant advantage that allows our proposal to be used in biomedical fields to detect and diagnose certain diseases: the detection of calcium oxalate crystals is critical in detecting renal stone formation [9] and the detection of monosodium urate crystals in synovial fluid allows diagnosis gout [10].

To further test our LD-LHM, a sample containing starch grains has been imaged. Potato tissues were crushed and then dried to prepare this sample. The resulting powder was later spread in a sample holder and fixed with pure ethanol. The results for the starch grains sample are shown in Fig. 2 panels (d) to (f). In panels (d) and (e), the intensity image recovered via conventional DLHM and the I_{90} intensity image obtained via the proposed LD-LHM are shown. When potato starch granules are imaged with polarized light, they exhibit different birefringent patterns in the form of lobes creating Maltese crosses [11]. These features cannot be retrieved in the intensity image obtained via conventional bright field microscopy or LHM. In contrast, the visualization of the Maltese crosses in panel (e) is achieved by our proposal. This result indicates that the starch grain has a high degree of aligned molecules or crystals [11]. Finally, the intensity image for the first Stoke parameters is presented in panel (f)

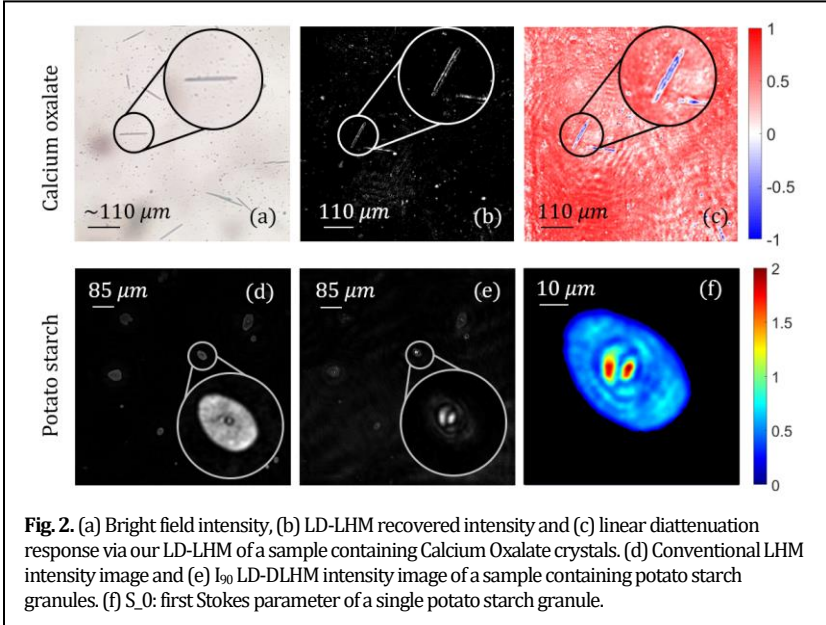


Fig. 2. (a) Bright field intensity, (b) LD-LHM recovered intensity and (c) linear diattenuation response via our LD-LHM of a sample containing Calcium Oxalate crystals. (d) Conventional LHM intensity image and (e) I_{90} LD-DLHM intensity image of a sample containing potato starch granules. (f) S_0 : first Stokes parameter of a single potato starch granule.

to compare the performance of our method against other related proposals to potato starch characterization. It can be observed in this image that the starch grains lobes present higher intensity which is due to the increase in the crystalline order of the starch granules in this section of the sample. Stokes parameters of starch granules demonstrated that an excitation pulse of linearly polarized light is transformed into right or left elliptically polarized light, which can be appreciated as a negative linear diattenuation [12].

4. Conclusion

The proposed linear diattenuation sensitive LHM consists of a two-shot procedure and the insertion of only two linear polarizers in a conventional LHM setup. The method has successfully recovered polarization information from samples extracted from biological environments, presenting a negative diattenuation response in both cases. In addition to the relevance of the extracted information, the proposed method has additional advantages of digital holography techniques such as the numerical refocusing of the holographic reconstructions and those of lensfree microscopy such as reduced and simplified setups. Consequently, our proposal will boost the application of this cost-effective field-portable technique in medicine and biology.

5. References

1. S. O. Isikman, A. Greenbaum, M. Lee, W. Bishara, O. Mudanyali, T.-W. Su, and A. Ozcan, "Lensfree computational microscopy tools for cell and tissue imaging at the point-of-care and in low-resource settings," *Anal. Cell. Pathol. (Amst)*, **35**, 229–247 (2012).
2. B. Bai, H. Wang, T. Liu, Y. Rivenson, J. FitzGerald, and A. Ozcan, "Pathological crystal imaging with single-shot computational polarized light microscopy," *J. Biophotonics* (2020).
3. M. J. Lopera and C. Trujillo, "Single-shot dual-wavelength Polarized Microscope to detect Malaria-infected Erythrocytes via birefringence response," in *Conference on Lasers and Electro-Optics* (Optical Society of America, 2021).
4. C. Trujillo and M. J. Lopera, "Portable cellphone-based digital lensless holographic microscope," *Front. Opt. + Laser Sci.* 2021 (2021), Pap. JTh5A.14 JTh5A.14 (2021).
5. W. Xu, M. H. Jericho, I. A. Meinertzhagen, and H. J. Kreuzer, "Digital in-line holography for biological applications," *Proc. Natl. Acad. Sci. U. S. A.* **98**, 11301–11305 (2001).
6. C. Trujillo, P. Piedrahita-Quintero, and J. Garcia-Sucerquia, "Digital lensless holographic microscopy: numerical simulation and reconstruction with ImageJ," *Appl. Opt.* **59**, 5788 (2020).
7. M. J. Lopera and C. Trujillo, "Linear diattenuation imaging of biological samples with digital lensless holographic microscopy," *Appl. Opt.* **61**, B77 (2022).
8. Y. Zhang, S. Y. C. Lee, Y. Zhang, D. Furst, J. Fitzgerald, and A. Ozcan, "Wide-field imaging of birefringent synovial fluid crystals using lens-free polarized microscopy for gout diagnosis," *Sci. Rep.* **6**, 28793 (2016).
9. M. Asselman, A. Verhulst, M. E. De Broe, and C. F. Verkoelen, "Calcium Oxalate Crystal Adherence to Hyaluronan-, Osteopontin-, and CD44-Expressing Injured/Regenerating Tubular Epithelial Cells in Rat Kidneys," *J. Am. Soc. Nephrol.* **14**, 3155–3166 (2003).
10. Y. Yoo, Y. J. Seo, M. Huh, J. H. Yoo, K. H. Yun, and S. J. Kim, "Gout and coexisting pseudogout in the knee joint," *Knee Surgery, Sport. Traumatol. Arthrosc.* **19**, 553–555 (2011).
11. X. Zhao, M. Andersson, and R. Andersson, "Resistant starch and other dietary fiber components in tubers from a high-amylose potato," *Food Chem.* **251**, 58–63 (2018).
12. C. M. Romero, F.-J. Kao, J. Qiu, M. R. Foreman, N. Mazumder, and P. Török, "Stokes vector based polarization resolved second harmonic microscopy of starch granules," *Biomed. Opt. Express*, Vol. 4, Issue 4, pp. 538–547, 538–547 (2013).

ANNEXES



In order to implement a solution targeting a simple, reliable and fast computer-aided diagnosis, we must first take different aspects into consideration. These aspects –such as the smartphone Operative System (OS), reconstruction algorithms and app portability between smartphones– will depict the design process of the app, and thus guide its development, from the conceptual design to the app realization.

2.1 General aspects

2.1.1 Portability and coverage

As mentioned before, more than 78% of the global population has smartphones. Moreover, Android phones have 89.47% of the smartphone market share in Latin America[18], since the phone manufacturers customize their models specifications to make them cheaper or to include more characteristics[19]. Thus, in order to cover most of the cases in Latin America, the targeted smartphones will be those based on Android.

Furthermore, the iOS app development requires a Mac computer to debug and build the app [20], so targeting Android phones removes also this restriction, as it's open-source and the developing tools are available on Windows, Linux and other OSs [21].

[18]: Kommandotech (2022), *The One OS to Rule Them All - 33 Android vs iOS Market Share Stats*

[19]: Dignited (2018), *Why are most Android phones cheaper than iPhones*

[20]: Apple Inc. (2022), *XCode Release Notes*

[21]: Google Developers (2022), *Download Android Studio & App Tools*

2.1.2 Simple mobile & web app developing

After defining the targeted OS, the next step is to try to minimize the time between adding features to the app and debugging them, as building the app after a feature addition, or testing the app itself on a device can take several minutes before one is able to fix or find the bugs. This is why frameworks like *React Native*[22] or *Flask*[23] do exist, both emphasizing into fast app prototyping and easy app complexity escalation. Consequently, we must use these type of frameworks during the app development in order to minimize the building time between changes in the code of the application.

[22]: Meta Platforms, Inc. (2022), *React Native*

[23]: The Pallets Projects (2022), *Flask*

2.1.3 Auto-focus in DH

On the other hand, as we are dealing with digital holograms, if we want to reconstruct them properly, we require the exact distance from the object to the camera. However, this is not possible in many cases[24], as we could be analyzing in real-time living cells or tracking them, or simply have acquired an hologram from another device or place. This is why an

[24]: İlhan et al. (2013), *Autofocusing in digital holography*

auto-focus method should be also implemented, such as methods based on *neural networks*, in case it's needed in a particular case. Moreover, this can lead to measuring depths and surface profiles of the samples[25], which could help the pathologist to identify the pathogen and diagnose the illness.

[25]: Lyu et al. (2017), *Fast autofocusing in digital holography using the magnitude differential*

2.2 Design Specification

Since the hardware specifications of the different Android smartphones may vary, a inexpensive, low-end Android phone with a basic camera, internet connection and minimal internal storage will be targeted. Consequently, we must assign the heavy duty of image processing and transforms done by the numerical wave propagation algorithms to a system which we will denote as the *server*. This system must be capable of performing this calculations in short time and, moreover, be able to communicate back and forward with the app in order to send the final reconstruction of the hologram.

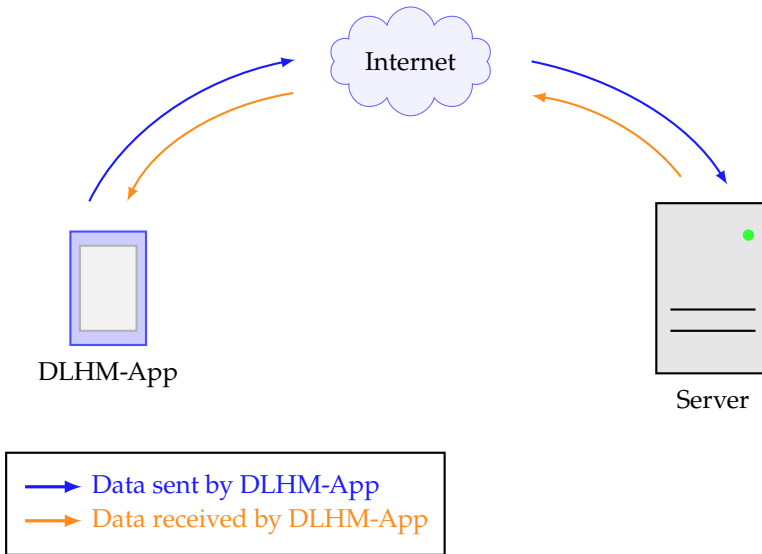


Figure 2.1: Communication scheme for DLHM-App.

In this vein, the function of the mobile app (known as the front-end) will be adding or capturing hologram images and their reference waves, storing these images in the internal storage, and send them to the server –the back-end– to further processing, waiting for the reconstructed hologram as a response. Taking all these specifications into account, the communication scheme between the front-end and the back-end can be formulated as in Figure 2.1.

2.2.1 Front-end

The front-end is responsible for storing, capturing, sending, receiving the data used by the user. It has a graphical interface that the user will

use to see and capture the desired holograms, as well as to configure the reconstruction parameters.

Moreover, the front-end was created in *JavaScript*¹ on the *React Native* platform.

1: A programming language.

Android Requirements

Once React Native creates an empty project, it selects the default minimum Android API and the API on which apps built with that specific React Native version were tested[26]. As DLHM-App uses React Native ver. 0.66.4, the minimum API level is 21 (i.e. Android 5.0) and the API level 30 (i.e. Android 11) as the targeted API. All of these requirements can be seen in the configuration files of the project.

[26]: StackOverflow (2014), *What is compileSdkVersion?*

Regarding the android permissions, the app requires the camera, internet, system alert, read/write external storage and download without notification permissions to capture, send, store and read the holograms and download the reconstruction from the server, respectively.

Graphical Interface

The graphical user interface (GUI) of DLHM-App has 5 screens: The main screen, the camera screen, the image preview screen, the reconstruction configuration screen and the reconstruction preview screen.

The Main Screen (Figure 2.2) lets the user add and select the hologram or the reference, and decide which reconstruction algorithm will the app use

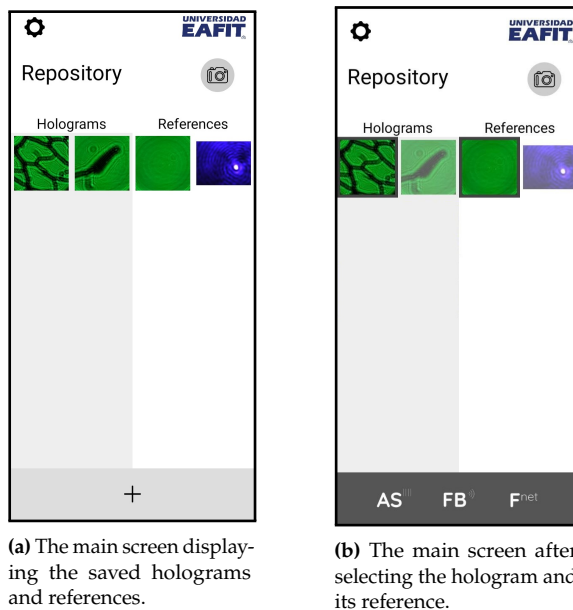


Figure 2.2: The main screen.

The Camera Screen (Figure 2.3a) lets the user capture holograms and references.

The Image Preview Screen (Figure 2.3b) allows the user to set the selected image as a hologram or a reference.

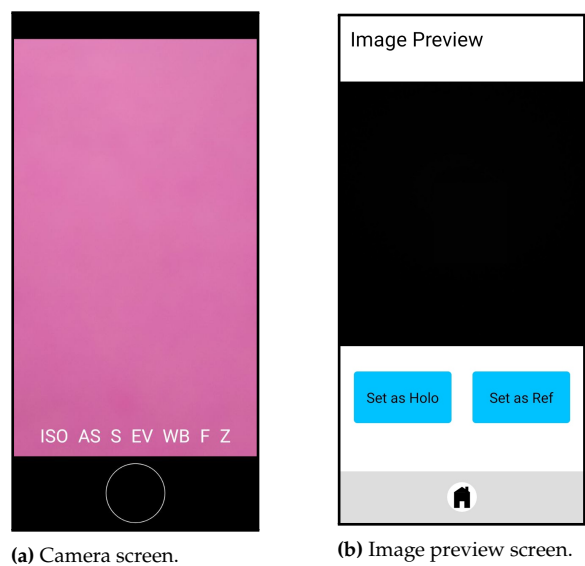


Figure 2.3: (a) The camera screen and (b) The image preview screen.

The Reconstruction Configuration Screen (Figure 2.4a) lets the user set the reconstruction algorithm’s parameters, such as the hologram type (phase, intensity or amplitude), the laser wavelength and the propagation distance.

The Reconstruction Preview Screen (Figure 2.4b) lets the user save or delete the obtained reconstruction.

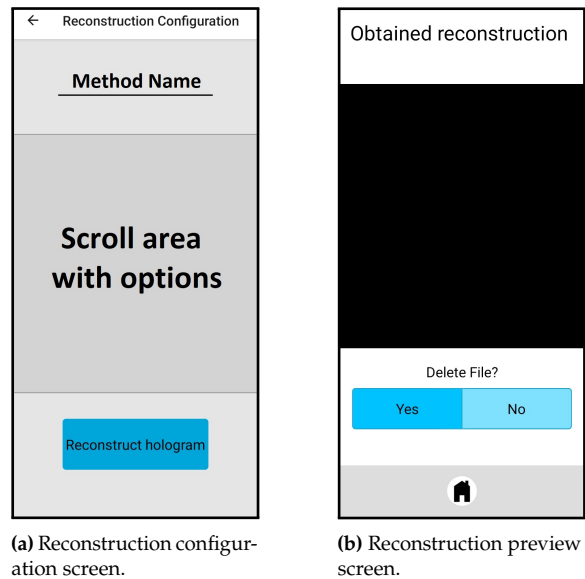


Figure 2.4: Reconstruction screens.

2.2.2 Back-end

On the other hand, the back-end accounts for receiving the images, creating the hologram reconstruction following the parameters given by the app, and sending it back to the user. In addition, it is in constant communication with the app during these steps. The back-end has also a *ping* function, which will notify the app (or whoever visits the specified link) if the server is running. In contrast with the front-end, which was developed with *React Native*, the back-end was built on the *Flask* platform using *Python*².

2: Another programming language

App Communication

The app can communicate with the back-end (i.e. send or receive information) via 5 paths: “dlhm/upload”, “dlhm/create-reconstruction”, “dlhm/get-reconstruction” and “ping”. These paths let the user upload the hologram and the reference (if any), create the reconstruction with the desired parameters, get the reconstructed hologram, and see if the server is running on the given IP, respectively.

Reconstruction Library

The reconstruction library consist of the Angular Spectrum (AS), the Fresnel-Bluestein propagation algorithms described in Chapter ??, plus a manager function:

reconstruct(holo_filepath, ref_filepath, options, outpath)

It is the manager function. It reads the hologram file, the reference file (if present), and calls the reconstruction function according to the options argument. If the selected algorithm is FocusNet [27] –which is a *Neural Network*–, then the hologram is reconstructed via AS with the best reconstruction distance FocusNet found. Moreover, the manager function saves the hologram reconstruction in the hard disk of the server as an PNG image file.

[27]: Lopera (2022), *Learning-Based Autofocusing Regression Model for Digital Lensless Holographic Microscopy*

fb_reconstruct2(holoC, z, L, dx, wavelength)

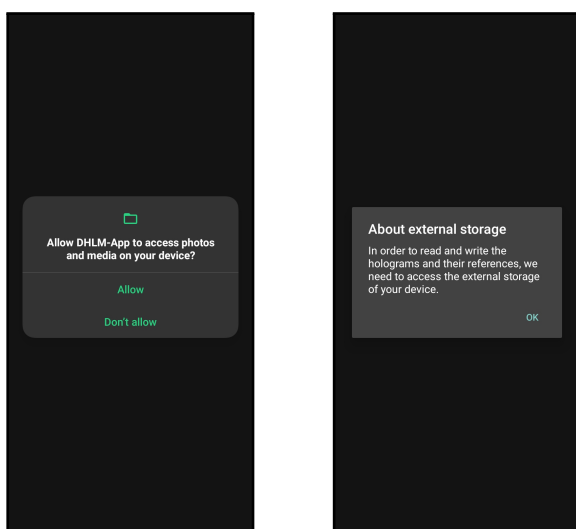
Reconstructs the contrast hologram *holoC* with the Fresnel-Bluestein transform (see ??). The parameters *z*, *L*, *dx* and *wavelength* are the object-to-camera distance, source-to-camera distance, camera’s pixel pitch and the laser wavelength, respectively. This function returns a matrix representing the reconstructed hologram.

as_reconstruct(holo, ref, dx, wavelength, z)

Reconstructs the hologram *holo* via AS (see ??). The parameters *ref*, *dx*, *wavelength* and *z* are a matrix representing the reference image, the camera’s pixel pitch, the laser wavelength and the object-to-camera distance, respectively. This function returns a matrix representing the reconstructed hologram.

3.1 First run

After installing and opening DLHM-App for the first time, the app will prompt a message requesting the read/write storage permission, as shown in Figure 3.1a. In case the app was already opened before but it does not have this permission, it will prompt a message explaining why is this permission needed (Figure 3.1b) in order to make use of the app.



(a) The read/write external storage permission prompt.

(b) The message explaining the read/write request.

Figure 3.1: Storage permission request prompts.

3.2 The Main Screen

If the app has the read/write permission, it will display the main screen (Figure 3.2). Here the app will display all the saved holograms and references that you have added (see Section 3.4). In this screen you can: Open the app configuration screen tapping the gear icon in the top left corner; navigate to the camera screen tapping the camera icon in the top right corner below the *Universidad EAFIT* logo to capture a new hologram (see 3.4.2); or add an existing image as a hologram or as a reference (see 3.4.1).

Note: It is highly recommended to change the server IP in the configuration screen before trying to reconstruct a hologram.

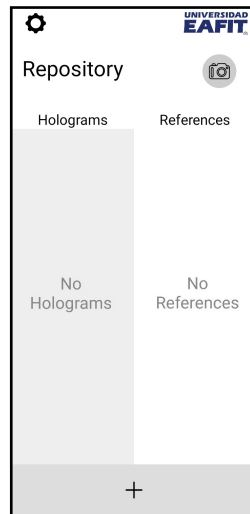


Figure 3.2: The main screen without any saved hologram or reference.

3.3 The Configuration Screen

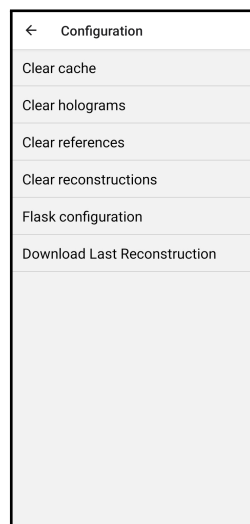


Figure 3.3: The app configuration screen.

The configuration screen lets you clean the image cache, the holograms, references and reconstructions, as well as change the server IP and download the last reconstruction (if available).

In order to change the default server IP, you must navigate to the server configuration screen (Figure 3.4a) tapping the "Flask configuration" option in the options list. After verifying the server connection, the app will notify you that the IP has been successfully changed and saved (Figure 3.4b). Otherwise, the app will notify you that it could not connect to the specified IP.

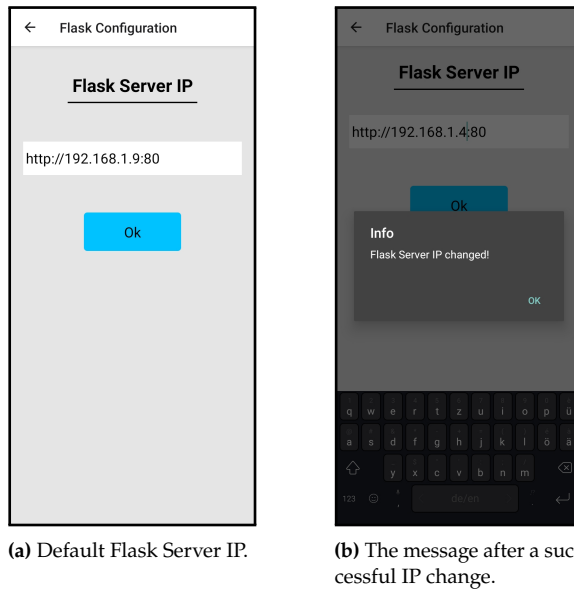


Figure 3.4: Flask IP configuration.

3.4 Adding an image to the repository

3.4.1 Gallery image

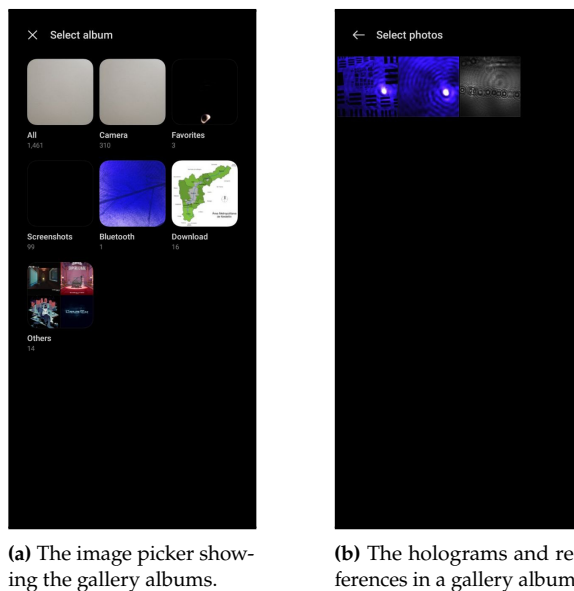


Figure 3.5: Image picker.

If you already have an image saved in your smartphone, you can add it pressing the plus (+) icon at the bottom of the main screen, which only appears if no hologram is selected. This will open to the image picker (Figure 3.5), where you can explore your albums and select the desired image. After selecting an image, the app will open it in the image preview screen in order to set it as an hologram or a reference (see 3.4.3).

3.4.2 Recording a hologram

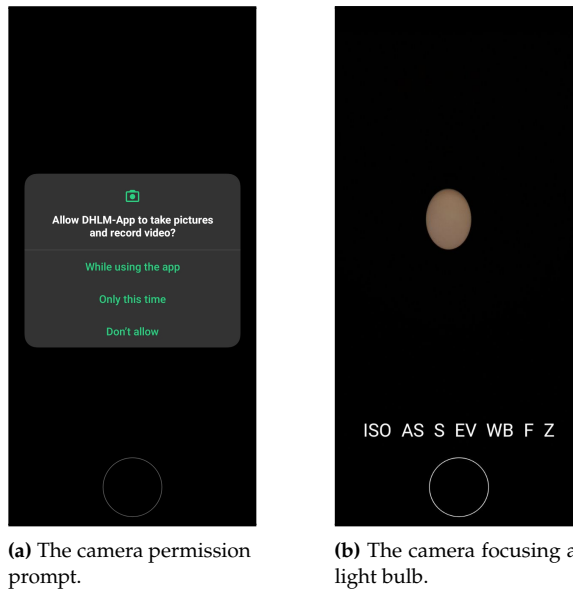


Figure 3.6: The Camera Screen.

On the other hand, if you want to capture a new hologram, you can tap the camera icon in the top right corner of the main screen. This will open the camera and now you will be able to capture a new hologram. If DLHM-App does not have the camera permission yet, it will prompt a message asking for this permission (Figure 3.6a). Then, the camera will start normally thereafter.

The camera screen has seven buttons named 'ISO', 'AS', 'S', 'EV', 'WB', 'F' and 'Z', as shown in Figure 3.6b. These buttons will let you change the ISO, activate or deactivate the automatic exposure, set the shutter speed, set the exposure compensation, white balance, focus depth and zoom, respectively. The ISO and the shutter speed settings will work only when the auto exposure (AS) is deactivated, which is its default setting.

Finally, to capture an image you should press the white circle in the bottom of the screen, as in most camera apps. Then the image will be opened in the image preview screen, explained in 3.4.3.

3.4.3 Adding the image

After selecting or capturing a new hologram or reference, the image will be displayed in the image preview screen, as shown in Figure 3.7. There you can set the image as an hologram or as an reference, by pressing the "Set as Holo" or "Set as Ref" buttons, respectively. Then, the image will be added to the repository, as shown in Figure 3.8.

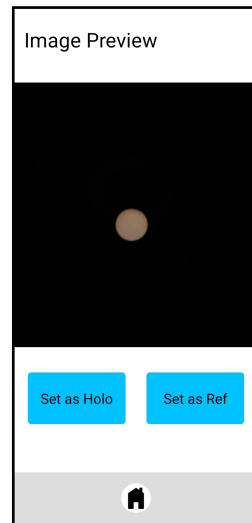
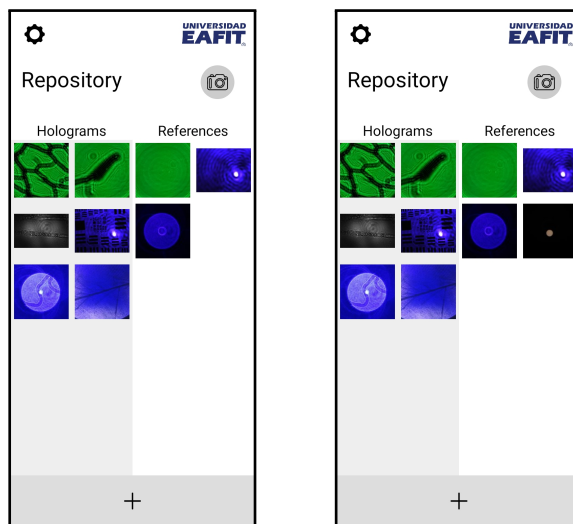


Figure 3.7: The image preview screen.



(a) Before the addition to the references list.

(b) After the addition to the references list.

Figure 3.8: The main screen before and after selecting the image as a reference.

3.5 Reconstructing an hologram

3.5.1 Selecting a hologram

Now that you have images in the repository, you can select or deselect them by tapping on them. In order to reconstruct the desired hologram you have to select it and its reference (if any), as shown in Figure 3.9. As soon as you select the hologram, the bottom panel will change its color and show three options, one per reconstruction algorithm: AS (**AS** button), Fresnel-Bluestein (**FB** button) or FocusNet (**F^{net}** button). Tapping on one of them will upload the images to the server and will lead you to the reconstruction configuration screen.

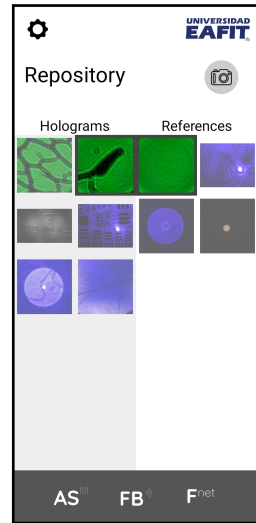
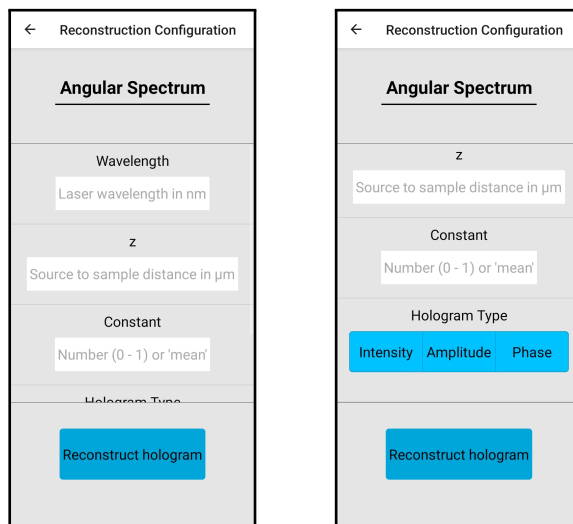


Figure 3.9: The main screen after selecting the hologram and reference.

3.5.2 The Reconstruction Configuration Screen



(a) The reconstruction configuration parameters before scrolling the screen.

(b) The reconstruction configuration parameters after scrolling the screen.

Figure 3.10: The reconstruction configuration screen.

The reconstruction configuration screen is shown in Figure 3.10. This screen displays the selected reconstruction algorithm and its obligatory parameters. In this case, the selected algorithm was AS, and, as no reference was selected, an additional input named '*Constant*' is shown (Figure 3.10b). This parameter accounts for the reference, and accepts a number between 0 and 1 (0 being black and 1 white) or the word '*mean*'. If *Constant* is a number, the reference will be a gray-scale image with the selected value; and if it is the word '*mean*', the reference will be the mean value of the selected hologram.

It is noteworthy to mention that if any parameter has an invalid or empty value the app will notify you with a message, such as the one shown in

Figure 3.11. This message will appear only after pressing the 'Reconstruct hologram' button, and before requesting the server the generation of the hologram reconstruction.

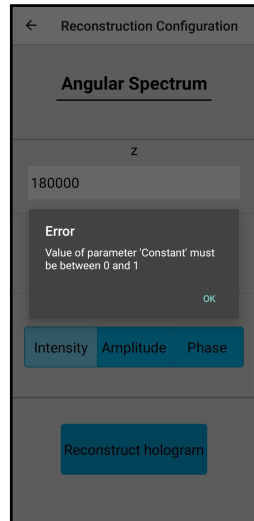


Figure 3.11: The main screen after selecting the hologram and reference.

3.5.3 The Reconstruction Preview Screen

Finally, and after getting the reconstruction, DLHM-App will display the received image in a preview screen, as shown in Figure 3.12. Here you can decide whether you want to keep or delete it from the smartphone's internal storage. The option selected by default is to keep the obtained reconstruction.



Figure 3.12: The main screen after selecting the hologram and reference.

Bibliography

Here are the references in citation order.

- [1] P.A. Pattanaik et al. 'Malaria detection using deep residual networks with mobile microscopy'. In: *Journal of King Saud University - Computer and Information Sciences* 34.5 (2022), pp. 1700–1705. doi: <https://doi.org/10.1016/j.jksuci.2020.07.003> (cit. on pp. 1–3).
- [2] Sumagna Dey et al. 'Malaria detection through digital microscopic imaging using Deep Greedy Network with transfer learning'. In: *Journal of Medical Imaging* 8.5 (2021), p. 054502. doi: [10.1117/1.JMI.8.5.054502](https://doi.org/10.1117/1.JMI.8.5.054502) (cit. on pp. 1, 2).
- [3] World Health Organization (WHO). *World malaria report 2021*. 6th Dec. 2021. URL: <https://www.who.int/teams/global-malaria-programme/reports/world-malaria-report-2021> (visited on 01/02/2022) (cit. on p. 1).
- [4] Lucy Williams and Vari M. Drennan. 'Evaluating the efficacy of rapid diagnostic tests for imported malaria in high income countries: A systematic review'. In: *International Emergency Nursing* 60 (2022), p. 101110. doi: <https://doi.org/10.1016/j.ienj.2021.101110> (cit. on p. 1).
- [5] Nam K Tran et al. 'Evolving Applications of Artificial Intelligence and Machine Learning in Infectious Diseases Testing'. In: *Clinical Chemistry* 68.1 (Dec. 2021), pp. 125–133. doi: [10.1093/clinchem/hvab239](https://doi.org/10.1093/clinchem/hvab239) (cit. on p. 1).
- [6] Xataka.com. *La brecha entre la Colombia rural y urbana, explicada a través de 9 gráficos*. 9th Oct. 2016. URL: <https://magnet.xataka.com/en-diez-minutos/la-brecha-entre-la-colombia-rural-y-urbana-explicada-a-traves-de-9-graficos> (visited on 31/01/2022) (cit. on p. 2).
- [7] B. Herazo. 'Some Problems of Health in Colombia'. In: *Dossier Salud Pública Y Epidemiología en Odontología* 29.63 (Apr. 2010), pp. 37–39 (cit. on p. 2).
- [8] Zelalem Dejazmach et al. 'Assessing the Performance of CareStart™ Malaria Rapid Diagnostic Tests in Northwest Ethiopia: A Cross-Sectional Study'. In: *Journal of Parasitology Research* 2021 (Oct. 2021). doi: [10.1155/2021/7919984](https://doi.org/10.1155/2021/7919984) (cit. on p. 2).
- [9] Gloria Díaz, Fabio A. González and Eduardo Romero. 'A semi-automatic method for quantification and classification of erythrocytes infected with malaria parasites in microscopic images'. In: *Journal of Biomedical Informatics* 42.2 (2009), pp. 296–307. doi: <https://doi.org/10.1016/j.jbi.2008.11.005> (cit. on p. 2).
- [10] Yair Rivenson et al. 'Phase recovery and holographic image reconstruction using deep learning in neural networks'. In: *Light: Science & Applications* 7.2 (Feb. 2018), pp. 17141–17141. doi: [10.1038/lsa.2017.141](https://doi.org/10.1038/lsa.2017.141) (cit. on p. 2).
- [11] Massachusetts Institute of Technology (MIT). *Innovators Under 30 – Aydogan Ozcan*, 30. 2009. URL: <http://www2.technologyreview.com/tr35/profile.aspx?TRID=808> (visited on 03/02/2022) (cit. on p. 2).
- [12] Maria J. Lopera. 'Microscopio polarimétrico sin lentes portable'. Undergraduate Thesis. Universidad EAFIT, 2020 (cit. on pp. 2, 3).
- [13] Statista. *Global smartphone penetration rate as share of population from 2016 to 2020*. URL: <https://www.statista.com/statistics/203734/global-smartphone-penetration-per-capita-since-2005> (visited on 03/02/2022) (cit. on p. 2).
- [14] Joseph Goodman. *Introduction to Fourier Optics*. 2nd ed. McGraw-Hill, 1996 (cit. on p. 3).

- [15] Etienne Cuche, Pierre Marquet and Christian Depeursinge. ‘Simultaneous amplitude-contrast and quantitative phase-contrast microscopy by numerical reconstruction of Fresnel off-axis holograms’. In: *Appl. Opt.* 38.34 (Dec. 1999), pp. 6994–7001. doi: [10.1364/AO.38.006994](https://doi.org/10.1364/AO.38.006994) (cit. on p. 3).
- [16] Ulf Schnars et al. *Digital Holography and Wavefront Sensing*. 2nd ed. Springer, 2015 (cit. on p. 3).
- [17] Myung K. Kim. ‘Principles and techniques of digital holographic microscopy’. In: *SPIE Reviews* 1.1 (May 2010), p. 018005. doi: [10.1117/6.0000006](https://doi.org/10.1117/6.0000006) (cit. on p. 3).
- [18] Kommandotech. *The One OS to Rule Them All - 33 Android vs iOS Market Share Stats*. 16th May 2022. URL: <https://kommandotech.com/statistics/android-vs-ios-market-share/> (visited on 01/06/2022) (cit. on p. 5).
- [19] Dignited. *Why are most Android phones cheaper than iPhones*. 17th Nov. 2018. URL: <https://www.dignited.com/36659/why-are-most-android-phones-cheaper-than-iphones/> (visited on 01/06/2022) (cit. on p. 5).
- [20] Apple Inc. *XCode Release Notes*. 2022. URL: <https://developer.apple.com/documentation/xcode-release-notes> (visited on 02/08/2022) (cit. on p. 5).
- [21] Google Developers. *Download Android Studio & App Tools*. 2022. URL: <https://developer.android.com/studio> (visited on 15/02/2022) (cit. on p. 5).
- [22] Meta Platforms, Inc. *React Native*. 2022. URL: <https://reactnative.dev/> (visited on 02/02/2022) (cit. on pp. 5, 19).
- [23] The Pallets Projects. *Flask*. 2022. URL: <https://palletsprojects.com/p/flask/> (visited on 02/02/2022) (cit. on pp. 5, 19).
- [24] Hazar A. İlhan, Mert Doğar and Meric Özcan. ‘Autofocusing in digital holography’. In: *Practical Holography XXVII: Materials and Applications*. Ed. by Hans I. Bjelkhagen and V. Michael Bove Jr. Vol. 8644. International Society for Optics and Photonics. SPIE, 2013, p. 86440C. doi: [10.1117/12.2002038](https://doi.org/10.1117/12.2002038) (cit. on p. 5).
- [25] Meng Lyu et al. ‘Fast autofocusing in digital holography using the magnitude differential’. In: *Appl. Opt.* 56.13 (May 2017), F152–F157. doi: [10.1364/AO.56.00F152](https://doi.org/10.1364/AO.56.00F152) (cit. on p. 6).
- [26] StackOverflow. *What is compile-SdkVersion?* 4th Dec. 2014. URL: <https://stackoverflow.com/questions/27301867/what-is-compilesdkversion> (visited on 14/07/2022) (cit. on p. 7).
- [27] Maria J. Lopera. ‘Learning-Based Autofocusing Regression Model for Digital Lensless Holographic Microscopy’. In: 2nd Aug. 2022 (cit. on p. 9).
- [28] IBM. *What Are Neural Networks?* 17th Aug. 2020. URL: <https://www.ibm.com/cloud/learn/neural-networks> (visited on 23/07/2022) (cit. on p. 19).
- [29] WSGI.org. *WSGI*. 2022. URL: <https://wsgi.readthedocs.io/en/latest/what.html> (visited on 02/02/2022) (cit. on p. 19).